DISSERTATION

VORTEX PHASES IN TYPE-I SUPERCONDUCTORS

Submitted by

Mark Sweeney

Department of Physics

In partial fulfillment of the requirements for the degree of

Doctor of Philosophy

Colorado State University

Fort Collins, Colorado

Fall 2010

Doctoral Committee:

Department Chair: John Harton

Advisor: Martin P Gelfand

Jennifer L Mueller
Richard M Bradley
Stuart B Field

ABSTRACT OF DISSERTATION

VORTEX PHASES IN TYPE-I SUPERCONDUCTORS

Sufficiently thin films of type-I superconductor in a perpendicular magnetic field exhibit a triangular vortex lattice, while thick films develop an intermediate state. To elucidate what happens between these two regimes, precise numerical calculations have been made within Ginzburg-Landau theory at $\kappa = 0.5$ and 0.25 for a variety of vortex lattice structures with one flux quantum per unit cell. The phase diagram in the space of mean induction and film thickness includes a narrow wedge in which a square lattice is stable, surrounded by the domain of stability of the triangular lattice at thinner films/lower fields and, on the other side, rectangular lattices with continuously varying aspect ratio. The vortex lattice has an anomalously small shear modulus within and close to the square lattice phase.

Solutions of the Ginzburg-Landau equations have also been obtained for bulk systems and thin films for vortex lattices with one vortex but two flux quanta per square or triangular unit cell. These lattices of double fluxoid vortices are thermodynamically unstable in bulk in both type-I and type-II superconductors, as expected. In type-I films the situation is less clear, because the corresponding calculations for more complicated vortex lattice structures are not yet possible.

Mark Sweeney
Department of Physics
Colorado State University
Fort Collins, CO 80523
Fall 2010

TABLE OF CONTENTS

List of Tables

List of Figures

1 Introduction

Nearly a century ago Gilles Holst, a researcher in the laboratory of Kammerling Onnes, discovered a new thermodynamic phase of matter [1]. On cooling a metal below a critical temperature, T_c, Holst found its resistivity would suddenly drop, apparently to zero. The initial phenomenon he observed gave the new phase its name, superconductivity. The more complete phenomenology emerged over time: perfect diamagnetism (Meissner-Ochsenfeld effect), a discontinuity in the specific heat at the transition temperature, magnetic flux quantization, and the magnetic response that categorizes a superconductor as either type-I or type-II. In this last phenomenon a type-I superconductor in an external magnetic field will undergo a first-order phase transition with a discontinuity in the entropy at the phase change and a corresponding latent heat. On the other hand, a type-II superconductor in an external magnetic field undergoes a second-order phase transition with a continuous change in the entropy and no latent heat associated with the phase change. Bulk samples of type-II superconductors and, of particular interest to the present work, thin films of type-I superconductors can exist in a state, called the mixed state, which is only partially diamagnetic. Magnetic flux penetrates the sample in microscopic filaments, at the core of which the superconductivity goes to zero. As will be discussed in the following sections these flux lines are also referred to as vortices and the term *vortex state* is synonymous with the mixed state. Bulk type-I samples do not show this behavior, but depending on sample geometry and strength of the external magnetic field, will in a single physical sample, separate into macroscopic normal regions and fully superconducting (i.e., perfectly diamagnetic) regions. This is referred to as the intermediate state. In both cases, the mixed state and intermediate state, there is a threshold value

for magnetic field magnitude above which superconductivity is completely destroyed. This critical field value is sample and temperature dependent.

It is now known that the superconducting phase is due to an attractive potential between electrons becoming strong enough at low temperatures that the electrons form bound pairs, known as Cooper pairs. At the superconducting transition free electrons will form Cooper pairs and the superconducting state can then be described by a macroscopic wave function constructed from these Cooper pair states. It is in this sense that we talk about superconducting electrons condensing from the normal conduction electrons. Much like superfluid helium and Bose-Einstein condensates, superconductors are an example of a macroscopic phenomenon due to quantum mechanics—in particular they are all examples of macroscopic coherent states. These new phases of matter can be grouped together in a category referred to as quantum liquids [2], and in each case the constituents that make up the quantum liquid condense out of a normal fluid (conduction electrons in the case of superconductors) and the new state exists as a mixture of normal and quantum fluid. More generally, this description of a superconductor with coexistent normally conducting and superconducting electrons is referred to as the two-fluid model. The roots of this model can be found in the work of Gorter and Casimir [3] as well as F. and H. London [4] from the 1930s.

The actual microscopic mechanism in classical superconductors was explained in 1957 by Bardeen, Cooper and Schrieffer [5] in their groundbreaking paper titled simply "Theory of Superconductivity". However, the work of this manuscript does not make use of BCS theory; our work is based on the phenomenological theory of Ginzburg and Landau [6]. Their work predates BCS by seven years and is still widely applied in work on classic as well as high T_c superconductors, and is even used in areas outside of condensed matter physics. At its core Ginzburg-Landau (GL) theory postulates a complex order parameter—a macroscopic pseudo-wave-function—whose

modulus squared is proportional to the superconducting electron concentration. In 1959 Gor'kov [7] showed that for temperatures close to T_c the Ginzburg-Landau equations (described in Sec. 2.6) can be derived from the BCS microscopic theory and that the GL order parameter is equivalent to the BCS groundstate wave function. One of the advantages of using GL theory rather than the BCS is that it is much easier to work with for cases where the order parameter varies in space. Tinkham [8], in 1963, addressed such a problem and applied Ginzburg-Landau theory to very thin films of type-I superconductors and showed that, contrary to the bulk case, films of these materials can exist in the mixed state.

This is the primary focus of the current work: the mixed state in films of type-I superconductors. Towards that end we revisit the problem of vortex lattices that carry more than one flux quanta per vortex in bulk samples; the method we employ for films requires having a bulk "solution" as a starting point. For these two problems, multiply quantized vortices in bulk and equilibrium vortex lattices in type-I films, we defer the respective introductory material until those sections where we present our results. We first review in Sec. 2 the macroscopic phenomenology relevant to the discussion of the mixed state in bulk samples and in films. The material in this section follows the presentations in the classic texts by De Gennes [9] and Tinkham [10]. In Sec. 3 we discuss the vortex structure and the functional form for the fields (order parameter and local magnetic induction) that constitute superconducting vortices. Following this, in Sec. 4, we give results specific for type-I and type-II bulk samples. While the former are non-equilibrium states they are, as mentioned above, a precursor to our work on films and show some interesting behavior we wish to report. We conclude with a discussion of our work and results for films of type-I superconductors in Sec. 5. Much of the technical detail, along with background material, has been placed in Appendices A-K.

2 Phenomenology

In this section we discuss some of the observed properties and behaviors of superconductors and two theories that explain them. In this section, unless otherwise stated, we will use as our canonical geometry a long cylinder aligned with the z-axis placed in a homogeneous longitudinal magnetic field $\mathbf{H}_a = H_a\hat{z}$. The sample has a demagnetization factor equal to zero, explained in Sec. 2.3.

First, a distinction must be made between a superconductor and a normal metal with zero resistivity, i.e., a perfect conductor. Assume we have defect-free samples of a superconductor and of a perfect conductor. Also, assume the perfect conductor has a finite resistivity above the superconductor's transition temperature T_c. If both materials are in a zero magnetic field with a temperature below the critical value and then a small magnetic field is applied, neither material will allow flux penetration in the interior. For the perfect conductor this is due to Faraday's law; the changing magnetic field induces screening currents to circulate. In the second case both materials are above the critical temperature but with the same small applied magnetic field. Magnetic flux freely penetrates both samples. On decreasing the temperature below T_c, the perfect conductor will show no change. The superconductor on the other hand will expel all magnetic flux from the interior (i.e., act as a perfect diamagnet). The superconducting state is a function of temperature and magnetic field and does not depend on the magnetic history of the sample. It is this behavior that justifies categorizing the superconducting state as a thermodynamic state. It must be said that we assumed there are no impurities or defects in the sample and we will use this assumption for the rest of this work.

Finally, a note regarding terminology: in Sec. 2.6 we introduce the complex Ginzburg-Landau order parameter, ψ. As mentioned in the introduction this is equivalent to the BCS wave function and $|\psi|^2$ is proportional to the superconducting electron density. We will also use the term "order parameter" interchangeably with "condensate wave function".

2.1 Characteristic Length Scales

A superconductor is characterized in part by two length scales: the penetration depth, λ, and the coherence length, ξ. The penetration depth describes the distance over which the local magnetic induction decays at a normal/superconducting boundary. The coherence length is the minimum distance over which the order parameter can vary. A similar description due to Pippard [11] is that ξ is the distance over which the condensate responds to a perturbation. In addition, it turns out that the mean Cooper pair radius is approximately equal to ξ. Both λ and ξ are minimums at $T = 0$ with $\lambda(T) \cong \lambda(0)\left[1 - {}^{T}/_{T_c}\right]^{-1/2}$ and $\xi(T) \cong \xi(0)\left[1 - {}^{T}/_{T_c}\right]^{-1/2}$. However, the ratio of these two lengths is approximately constant and defines the dimensionless Ginzburg-Landau parameter, $\kappa \equiv \lambda/\xi$. As will be discussed in the following subsection for $\kappa < 1/\sqrt{2}$ a material will be a type-I superconductor, for $\kappa > 1/\sqrt{2}$ a material will be type-II.

2.2 Critical Temperature, Critical Fields

As the temperature is decreased below a critical value, T_c, a superconductor will undergo a phase transition from the normal state to the superconducting state. In the presence of an external applied magnetic field, H_a, a type-I superconductor will change back to the normal state once $H_a \geq H_c$. As mentioned in the introduction this is a first-order phase transition. H_c is called the thermodynamic critical field. It is a

function of temperature with a maximum at $T = 0$ and H_c decreases monotonically to zero at $T = T_c$.

Type-II superconductors, on the other hand, undergo a second-order phase transition and exhibit a different diamagnetic response. Starting from the superconducting state with no applied field we then increase H_a. Once it reaches a value equal to H_{c1}, called the lower critical field, flux will begin to penetrate the sample in filaments or flux lines. As the external field is further increased, the density of flux lines increases, which in turn raises the mean induction for the sample, until the external field reaches H_{c2}. Above this value the entire sample will go to the normal state with mean induction $\bar{B} = \mu_0 H_a$. For $H_a < H_{c1}$ the material is in the Meissner state, $\bar{B} = 0$ and magnetic susceptibility $\chi = -1$ (units and magnetic conventions are discussed in Appendices A and B). For the external field in the range $H_{c1} \leq H_a \leq H_{c2}$ the material is in the mixed state, $\bar{B} < \mu_0 H_a$ and $\chi > 0$. For $H_a > H_{c2}$ the material is in the normal state, $\bar{B} = \mu_0 H_a$ and $\chi = 0$. Both H_{c1} and H_{c2} exhibit a similar temperature dependence to H_c: maximum at $T = 0$ and decreasing as temperature is increased. In Fig. 1 we show phase diagrams for type-I and type-II superconductors as a function of temperature and applied field.

A type-I superconductor with volume V in the Meissner state will be lower in free energy than the normal state by $\frac{1}{2}\mu_0 H_c^2 V$—this is the magnetic field energy that has been expelled from the sample. The energy density $\frac{1}{2}\mu_0 H_c^2$ is referred to as the condensation energy. For type-II superconductors we use the energy difference between the normal state and the Meissner state as a definition for the thermodynamic critical field in type-II materials. We set this energy difference equal to $\frac{1}{2}\mu_0 H_c^2 V$. In type-II superconductors H_c lies between the lower and upper critical fields, $H_{c1} \leq H_c \leq H_{c2}$; however nothing unique happens at $H_a = H_c$.

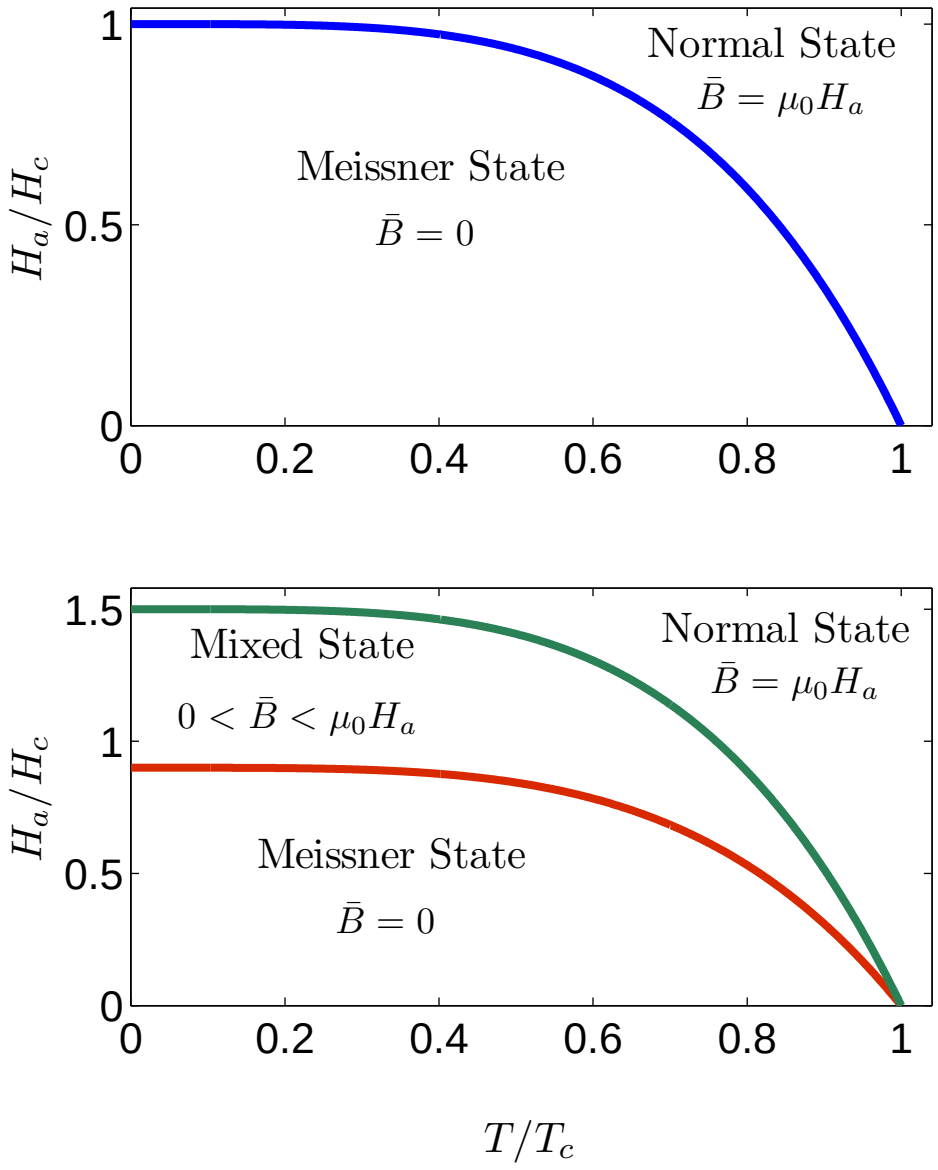

Figure 1: H_a-T Phase Diagrams

H_a-T phase diagrams for Type-I (upper) and Type-II (lower) superconductors.

2.3 Intermediate State, Mixed State

The initial division between type-I and type-II materials was based on the observation that some superconductors in an external magnetic field exhibit only a partial flux expulsion, regardless of sample shape. These type-II superconductors can exist somewhere between the normal state and the fully superconducting Meissner state. Type-I superconductors in cylindrical geometries aligned with the magnetic field will only exist in the normal state and the Meissner state. However in other geometries, for example a slab, a type-I superconductor will break up into macroscopic fully superconducting and normal regions. Here we examine some of the magnetic structures that form when a superconducting sample as a whole has $0 < \bar{B} < \mu_0 H_a$.

At an interface between normal and superconducting regions there is an energy associated with the surface area between the two regions. The energy per unit area, or surface tension, can be positive or negative and the value of the GL parameter, κ, determines the sign and relative strength of this surface tension. For type-I materials the surface tension is positive and the overall energy can be reduced by decreasing the interface surface area. For type-II materials the surface tension is negative and maximizing the surface area is favored. At the critical value $\kappa = 1/\sqrt{2}$ the surface tension is zero and there is no surface energy associated with the boundary between normal and superconducting regions.

As an example of geometry effects on the magnetic structures, consider a disk with a radius much larger than its thickness placed in an external magnetic field directed normal to its two faces. There is a demagnetization factor n associated with different geometries (see §29 in reference [12]), ranging in value from zero for a very long, thin cylinder (magnetic field directed along its axis) to $n \approx 1$ for the case considered here. A bulk superconductor in a weak external field acts as a perfect diamagnet and all magnetic flux is expelled. For the wide, thin disk this flux expulsion would lead to high magnetic field values around the edges, exceeding the critical field value. In

addition the magnetic field energy density will be very large in these regions. So it is energetically favorable for flux to penetrate the sample first by reducing the magnetic field energy density exterior to the sample and second by not maintaining the superconducting state (i.e., superheating) in regions bordering areas where the critical field value is exceeded. In type-I materials, with positive surface energy, it is favorable to form large macroscopic regions of flux penetration and complimentary large regions where $B = 0$. The sample breaks up into macroscopic normal regions and macroscopic superconducting regions—it enters the intermediate state. On the other hand, type-II materials, with negative surface energy, favor increasing the surface area to volume ratio of flux penetrating regions. The magnetic flux will penetrate the sample in thin filaments, or flux lines, rather than macroscopic regions. This is the mixed state, also referred to as the vortex state or Schubnikov phase.

The disk was used as an example to illustrate the differences between the intermediate state and the mixed state, and the effects of sample shape. However type-II superconductors of any shape (demagnetization factor $0 \leq n \leq 1$) will exist in the mixed state and never the intermediate state. Further, thin films of type-I superconductors can exist in the mixed state.

2.4 London Theory

In 1935 Fritz and Heinz London [4] proposed a model for superconductivity based on the Drude model for normal conductors. In their theory the supercurrent is determined by the local vector potential

$$\mathbf{j}_S(\mathbf{r}) = -\frac{1}{\mu_0}\frac{1}{\lambda_L^2}\mathbf{A}(\mathbf{r}) \tag{1}$$

with $\mathbf{B} = \nabla \times \mathbf{A}$ and where λ_L is a phenomenological parameter called the London penetration depth. Taking the curl of both sides and applying Ampere's law leads to

the London equation

$$\nabla^2 \mathbf{B}(\mathbf{r}) = \frac{1}{\lambda_L^2} \mathbf{B}(\mathbf{r}) \ . \tag{2}$$

In this form the meaning of penetration depth is more clear, at the interface between a superconductor and free space where $\mathbf{B}_{\text{ext}} \neq 0$, λ_L is the length scale over the field decays inside the superconductor. For charge carriers with concentration n, mass m and charge q, $\lambda_L = \sqrt{m/\mu_0 n q^2}$. More importantly the London equation shows that, except close to a boundary, the induction inside a superconductor must be zero, i.e., it explains the Meissner effect. However, London theory does not allow for spatial variation of the condensate and is best suited to describe the behavior of strongly type-II superconductors.

2.5 Flux Quantization

A charged particle moving in a magnetic field has a velocity operator

$$\mathbf{v} = \frac{1}{m} \left(-i\hbar\nabla - q\mathbf{A} \right) \ .$$

Anticipating the material in Section 2.6, ψ is the wave function (or order parameter) that describes the superconducting state and $|\psi|^2 = n_s$, the concentration of superconducting charge carriers. Then $\psi = \sqrt{n_s} e^{i\varphi}$ and the current density is

$$\mathbf{j} = q\psi^* \mathbf{v} \psi = \frac{q n_s}{m} \left(\hbar\nabla\varphi - q\mathbf{A} \right) \ .$$

Rearranging we get an expression for the vector potential:

$$\mathbf{A} = \frac{\hbar}{q}\nabla\varphi - \frac{m}{q^2 n_s}\mathbf{j} \, .$$

Now consider a superconductor in the shape of a ring with a large cross-section placed in an applied field such that there is a non-zero magnetic flux, $\Phi = \int_S \mathbf{B} \cdot \hat{n}\, da$, through the center of the ring. Assume the ring is in the Meissner state. Then $\mathbf{B}$ and $\mathbf{j}$ are zero at interior locations away from the ring surface. Applying Stokes's theorem and taking a closed contour C through this Meissner state region we obtain: $\Phi = \oint_C \nabla \times \mathbf{B} \cdot d\mathbf{l} = \oint_C \frac{\hbar}{q} \nabla\varphi \cdot d\mathbf{l}$. The phase must be single valued modulo 2π so $\oint_C \nabla\varphi \cdot d\mathbf{l} = p2\pi$ where p is an integer. This gives $\Phi = p\frac{2\pi\hbar}{q}$ and in 1948 when Fritz London [13] examined this problem he predicted that the flux through the ring would be quantized in units of $\frac{2\pi\hbar}{e}$. London assumed the charge carriers were individual electrons (not Cooper pairs) and his predicted flux quantum was two times too large. In 1961 experiments [14, 15] showed the quantum of flux for the ring configuration is

$$\Phi_0 = \frac{2\pi\hbar}{2e} = 2.07 \times 10^{-15}\,\mathrm{T\,m^2}\,. \tag{3}$$

London defined the fluxoid for a region as the sum of the flux and of the contour integral of the gauge-invariant supervelocity:

$$\Phi' \equiv \Phi + \frac{m}{q} \oint_C \mathbf{Q} \cdot d\mathbf{l}\,. \tag{4}$$

The supervelocity is defined to be

$$\mathbf{Q} \equiv \frac{1}{m} \left(\hbar\nabla\varphi - q\mathbf{A}\right)\,. \tag{5}$$

With the correct assignment $q = 2e$ it is the fluxoid that is quantized in superconductors. In cases where the contour C in Eq. (4) has $\oint_C \mathbf{Q} \cdot d\mathbf{l} = 0$ the associated flux will also be quantized. London defined the fluxoid before the full details of the mixed

state were known but we will revisit the fluxoid in Sec. 3 and apply the concept to vortices.

2.6 Ginzburg-Landau Theory

In 1950 Ginzburg and Landau [6] proposed their theory of superconductivity in which they postulated the existence of a complex order parameter $\psi(\mathbf{r})$—a macroscopic pseudo wave function—with $|\psi(\mathbf{r})|^2$ proportional to n_s, the superconducting electron concentration. Further, they assumed a free energy density, F, as an expansion in powers of $\psi(\mathbf{r})$. This was based on Landau's general theory of second-order phase transitions (see reference [16], chapter XIV) where there is a continuous change from a more symmetric (less ordered) state to a less symmetric (more ordered) state. However, the Ginzburg-Landau theory allows for both first and second-order phase transitions. In both cases ψ gives a measure of the order in the superconducting state, with $|\psi|$ increasing as the temperature drops below T_c. Within GL theory, if the spatial average over the sample $\left\langle |\psi(\mathbf{r})|^2 \right\rangle$ has a discontinuous jump from zero to some finite value at the transition then it is a first-order phase transition. On the other hand, if this average of the order parameter varies continuously from zero at the transition then the phase transition is of second order. Since the GL free energy functional F is expressed as a finite expansion then GL theory should only apply when $|\psi|$ is small, and in practice this means that the temperature must be close to T_c. However, the advantages of GL theory are that it applies to both types of superconductors, allows for a spatially varying condensate and is much easier to work with than BCS theory. In the rest of section we present GL theory in the context of the problems we will explore; for more general treatments see De Gennes or Tinkham [10, 9].

In Ginzburg-Landau theory the free energy density is expanded in even powers of $|\psi|$ (F must be real and $|\psi|$ is not analytic at $\psi(0)$) and additional terms are included

for kinetic energy and magnetic field energy. In this manuscript we consider periodic structures of infinite extent. For this reason we work with the free energy per unit cell or mean free energy density. The GL mean free energy density is

$$\bar{F} = \frac{1}{V}\int_V d^3r \left\{ \alpha \left|\psi\left(\mathbf{r}\right)\right|^2 + \frac{\beta}{2}\left|\psi\left(\mathbf{r}\right)\right|^4 + \frac{1}{2m}\left|\left(-i\hbar\nabla - q\mathbf{A}\right)\psi\left(\mathbf{r}\right)\right|^2 + \frac{1}{2\mu_0}\left|\mathbf{B}\right|^2 \right\} \quad (6)$$

α and β are phenomenological parameters, where $\alpha\left(T\right) = \alpha_0\left({}^{T}/_{T_c} - 1\right)$ with $\alpha_0 > 0$, and β is temperature independent. The modulus squared order parameter, $\left|\psi\right|^2$, has units of number density. If the temperature is above T_c then in equilibrium the material will be in the (more symmetric, disordered) normal state and $\psi = 0$. In the Meissner state ψ is uniform throughout the interior of a bulk superconductor and $\mathbf{B} = \mathbf{A} = 0$. In this case the free energy is minimized if $\left|\psi\right|^2 = \frac{-\alpha}{\beta}$ and $\bar{F}_{Meissner} = \frac{-\alpha^2}{2\beta}$. Since the phase is constant we can take the Meissner state order parameter to be real valued and define

$$\psi_\infty \equiv \sqrt{\frac{-\alpha}{\beta}}\,. \quad (7)$$

The subscript on ψ_∞ is to indicate that this is the value for the bulk interior. As mentioned previously, we work primarily with the free energy per unit cell but it is the integrand in Eq. (6) that is the actual free energy density.

Writing $\psi = \left|\psi\right| e^{i\varphi}$ and looking at the kinetic energy, $\frac{1}{2m}\left|\left(-i\hbar\nabla - q\mathbf{A}\right)\psi\right|^2 = \frac{1}{2m}\left[\hbar\left(\nabla\left|\psi\right|\right)^2 + \left(\hbar\nabla\varphi - q\mathbf{A}\right)^2\left|\psi\right|^2\right]$. The first term gives the additional energy due to variations in the magnitude of the order parameter. The second term gives the gauge invariant form of the kinetic energy of the supercurrents. From Eq. (5) the gauge invariant supervelocity is $\mathbf{Q} = \frac{1}{m}\left(\hbar\nabla\varphi - q\mathbf{A}\right)$, so that the supercurrent energy can be written $\frac{1}{2}m\mathbf{Q}^2\left|\psi\right|^2$, and $\frac{q}{m}\left(\hbar\nabla\varphi - q\mathbf{A}\right)\left|\psi\right|^2 = q\mathbf{Q}\left|\psi\right|^2$ gives the supercurrent, $\mathbf{j}$.

The free energy can be written in reduced units (see appendix A)

$$\bar{F} = \frac{1}{V}\int_V d^3r \left\{ \frac{1}{2} - |\psi|^2 + \frac{1}{2}|\psi|^4 + \left| \left(-\frac{i}{\kappa}\nabla - \mathbf{A} \right) \psi \right|^2 + |\mathbf{B}|^2 \right\} \tag{8}$$

where a constant term is included so the Meissner state has $\bar{F} = 0$ (in reduced energy density units $\frac{1}{2} = \frac{1}{2}\mu_0 H_c^2$). We assume the material is otherwise non-magnetic so the normal state free energy is constant. Eq. (8) applies to the bulk case and we will modify this free energy functional for the film case in Sec. 5. Calculating the variation δF with respect to $\delta\psi$ and $\delta\mathbf{A}$ and setting equal to zero gives the Ginzburg-Landau equations

$$\left(-\frac{i}{\kappa}\nabla - \mathbf{A} \right)^2 \psi = \psi\left(1 - |\psi|^2\right) \tag{9}$$

$$\nabla \times (\nabla \times \mathbf{A}) = -\frac{i}{2\kappa}\left(\psi\nabla\psi^\star - \psi^\star\nabla\psi\right) - |\psi|^2 \mathbf{A}\,. \tag{10}$$

In working with Ginzburg-Landau theory solving the coupled nonlinear GL equations for ψ and $\mathbf{A}$ (or $\mathbf{Q}$) is the crux of the problem. Note that the right hand of (10) side is the definition of the supercurrent so this is a statement of Ampere's law. Also, if the order parameter is uniform then Eq. (10) reduces to $\mathbf{j} = -|\psi|^2 \mathbf{A}$, and we recover the London equation Eq. (1).

We employ two gauge invariant versions of the GL energy and GL equations when calculating energies for superconductors in the mixed state. Both versions use a real valued order parameter, either $f = |\psi|$ or $\omega = |\psi|^2$. In the low induction regime, where vortices are spaced far apart, we assume radial symmetry for all fields. Then we use the order parameter magnitude f and we have

$$\bar{F} = \frac{1}{V}\int_V d^3r \left\{ \frac{1}{2} - f^2 + \frac{1}{2}f^4 + \frac{1}{\kappa^2}|\nabla f|^2 + f^2|\mathbf{Q}|^2 + |\mathbf{B}|^2 \right\} \tag{11}$$

$$\frac{1}{\kappa^2}\nabla^2 f = f|\mathbf{Q}|^2 - f + f^3 \tag{12}$$

$$\nabla \times \mathbf{B} = -f^2 \mathbf{Q} \,. \tag{13}$$

As the induction rises the vortex density increases and the vortices begin to overlap. Repulsive forces then become significant and the free energy can be minimized by particular arrangements of vortices. We can no longer assume radial symmetry and the vortices form a flux line lattice. In this regime we use the modulus squared order parameter $\omega = |\psi|^2$ and our working equations are

$$\bar{F} = \frac{1}{V} \int_V d^3 r \left\{ \frac{1}{2} - \omega + \frac{1}{2}\omega^2 + \frac{1}{4\kappa^2} \frac{|\nabla \omega|^2}{\omega} + \omega \left|\mathbf{Q}\right|^2 + \left|\mathbf{B}\right|^2 \right\} \tag{14}$$

$$\frac{1}{2\kappa^2} \nabla^2 \omega = -\omega + \omega^2 + \omega \left|\mathbf{Q}\right|^2 + \frac{1}{4\kappa^2} \frac{|\nabla \omega|^2}{\omega} \tag{15}$$

$$\nabla \times \mathbf{B} = -\omega \mathbf{Q} \tag{16}$$

3 Vortex Structure

Superconductors are unique among superfluids in that the condensate carries a net charge. While in motion the superconducting condensate generates a magnetic field and in turn is subject to magnetic forces. At equilibrium vortices in superconductors exist only if there is a non-zero applied magnetic field. The vortices are line singularities where the order parameter magnitude, $|\psi|$, is zero and its phase, φ, is undefined. Moving out from the core $|\psi|$ will rise to a maximum on a length scale according to the coherence length, ξ. In addition, on making a complete circuit around the core, the phase of the order parameter can only change by $2\pi p$. The integer p determines the number of flux quanta associated with the vortex. The local magnetic induction, $\mathbf{B}(\mathbf{r})$, will have a maximum at the vortex core and then decrease over a length scale described by the penetration depth λ. In Fig. 2 we show the different vortex profiles for different values of $\kappa = \lambda/\xi$. The condensate circulates around the vortex core generating a superconducting current or supercurrent, $\mathbf{j}(\mathbf{r})$ and Ampère's law tells us that $j \sim -\frac{\partial B}{\partial r}$. The supercurrent magnitude will rise from a zero value at the core then moving outward will rise to a local maximum (approximately at $r = \xi$) and then drop off to zero, see Fig. 3. The order parameter and local magnetic induction are roughly complements of each other. It is this coupled behavior that makes the terms "vortex" and "flux-line" interchangeable for superconductors. In general no magnetic field line has an endpoint (in the absence of magnetic monopoles) and superconducting vortices must begin and end on the sample surface (or form closed loops within the sample).

This section is intended as a bridge between the background material and the presentation of our methods and results. The structure of a vortex, especially at

positions close to the core, is important to our development of an Ansatz for multiply quantized vortices. The configurations we examine in this work are for superconducting films of thickness d parallel to the xy-plane and centered at $z = 0$. The applied magnetic field is normal to the film surface, $\mathbf{H}_a = H_a\hat{z}$, and the sample will have mean induction $\bar{\mathbf{B}} = \bar{B}\hat{z}$. Depending on context we may work with Cartesian, (x, y, z), or cylindrical, (r, θ, z), coordinates. In general we will use $(\mathbf{r}_\perp, z)$, with $\mathbf{r}_\perp = x\hat{x} + y\hat{y}$, and express vector quantities like the local induction as $\mathbf{B}(\mathbf{r}_\perp, z) = \mathbf{B}_\perp(\mathbf{r}_\perp, z) + B_z(\mathbf{r}_\perp, z)\hat{z}$. In cases with radial symmetry vector quantities will be decomposed as $\mathbf{V}(\mathbf{r}) = V_r(r_\perp, z)\hat{r} + V_\theta(r_\perp, z)\hat{\theta} + V_z(r_\perp, z)\hat{z}$. Finally, we note that the behavior near the core is a crucial boundary condition and we have summarized this behavior for $|\psi|$, B, etc. in Table 1.

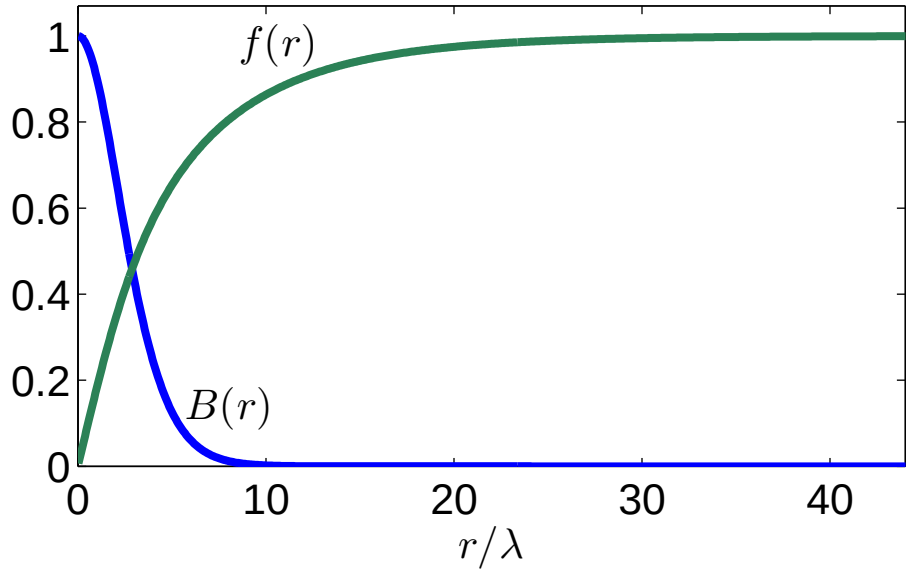

(a) $\kappa = 0.1$

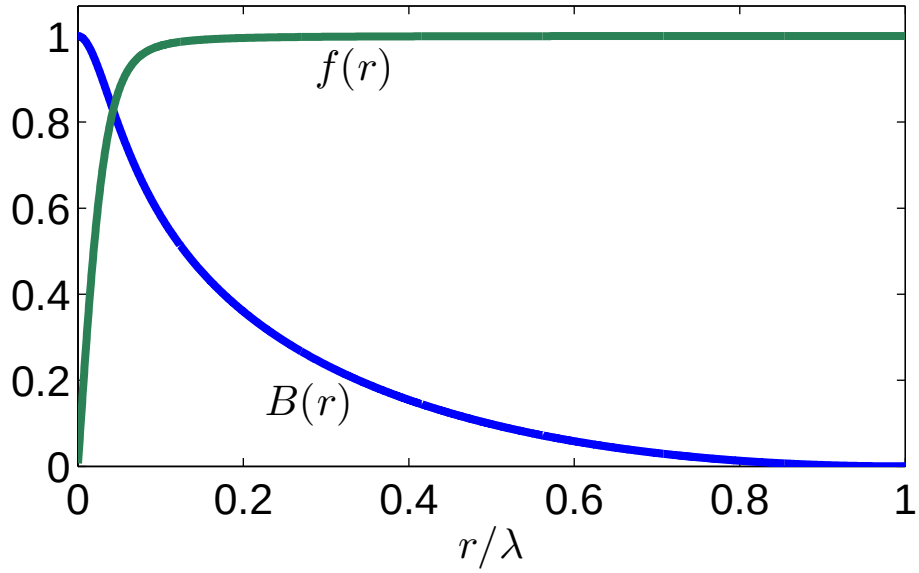

(b) $\kappa = 50$

Figure 2: Vortices with $\kappa = 0.1$ and $\kappa = 50$

Two plots illustrating the relative difference in the radial dependence of the order parameter ($f(r) = |\psi(r)|$) and local induction for isolated $p = 1$ vortices with different κ values. The data comes from our circular cell computational method, details for which are in Sec. 4.6.1. For the upper plot $\bar{B} = 0.01\mu_0 H_{c2}$, in the lower plot $\bar{B} = 0.005\mu_0 H_{c2}$.

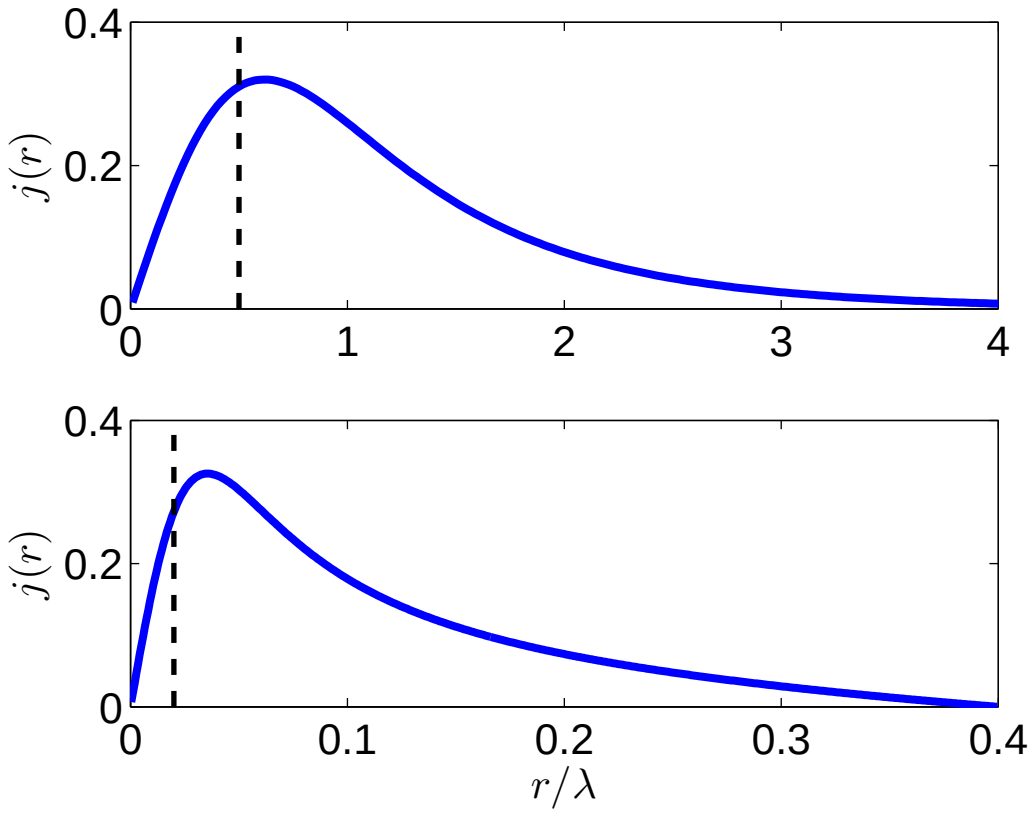

Figure 3: $j\,(r)$, for $\kappa = 2$ and $\kappa = 50$

Supercurrent for isolated $p = 1$ vortices with $\kappa = 2$ (upper plot) and $\kappa = 50$ (lower plot). The dashed line indicates the position $r = \xi$, the current maximum lies just beyond this location. In both plots $\bar{B} = 0.005\mu_0 H_{c2}$.

	$r_\perp \to 0$
$\psi(r_\perp, \theta)$	$r_\perp^p e^{ip\theta}$
$\mathbf{A}(r_\perp)$	$\left(\frac{1}{2}B_z(0)\, r_\perp - C_1 r_\perp^{2p+1}\right)\hat{\theta}$
$B_z(r_\perp)$	$B_z(0) - C_2 r_\perp^{2p}$
$\mathbf{Q}(r_\perp)$	$\left(\frac{1}{2}B_z(0)\, r_\perp - \frac{p}{\kappa r_\perp}\right)\hat{\theta}$
$\mathbf{j}(r_\perp)$	$r_\perp^{2p-1}\hat{\theta}$

Table 1: Summary of near-core behavior for bulk samples.

The near-core behavior of the p-quanta vortex gives crucial conditions on the mathematical fields we use in describing the vortex state. From Appendix E we have the result for small $r_\perp$ that $\psi(r_\perp, \theta) = c r_\perp^p e^{ip\theta}$, and from Appendix F that $B(r_\perp) = B(0) - \frac{1}{2\kappa}|\psi(r_\perp)|^2$. With $\nabla \times \mathbf{A} = \mathbf{B}$, the reduced unit definition of $\mathbf{Q}$ (Eq. (18)), and applying Ampère's law, we summarize the small $r_\perp$ behavior for the physical fields of interest. The values of the constants C_1 and C_2 in $\mathbf{A}$ and B_z are not important but both are positive and $C_2/C_1 = 2p + 2$.

3.1 The Fluxoid

In Sec. 2.5 we introduced flux quantization for holes in superconductors. Fritz London [13] first defined the fluxoid, Φ', associated with an island of normal region in the superconducting state as the sum of the flux through this hole and the contour integral of the supervelocity in a region surrounding the hole. The London fluxoid as defined in Eq. (4) actually simplifies to

$$\Phi' \equiv \frac{\hbar}{2e} \oint \nabla\varphi \cdot d\mathbf{s} \tag{17}$$

—a contour integral over the phase of the order parameter. Since the order parameter must be single valued the order parameter phase change for a complete circuit is $\oint \nabla\varphi \cdot d\mathbf{s} = 2\pi p$ with p an integer (in topology p is the winding number of the line defect). This gives the quantization condition on fluxoids: $\Phi' = p\Phi_0$. We can define the fluxoid as a vector quantity, $\mathbf{\Phi}'$, if we assign it a direction along the vortex core. In this work we will only consider cases for $\mathbf{\Phi}' = \Phi'\hat{z}$. If we take the contour integral in Eq. (17) around the singularity (i.e., the vortex core) we then get the fluxoid that is associated with the vortex. In this work when discussing p-quanta vortices we mean vortices that have an associated fluxoid with $\Phi' = p\Phi_0$.

3.2 Periodicity

With both film and bulk samples we consider the sample is large enough in the $\mathbf{r}_\perp$-plane that we can ignore the lateral boundaries and treat the sample as infinite in extent. In the mixed state we consider a uniform distribution of identical p-quanta vortices parallel to the z-axis. In other words we have a periodic arrangement of vortices giving a 2D lattice. In this lattice we restrict ourselves to one vortex per primitive unit cell. With each vortex there is $p\Phi_0$ of magnetic flux hence the primitive cell area is $S = p\Phi_0/\bar{B}$. In addition, we treat all fields (induction, order parameter,

supercurrents, etc.) as periodic. Our calculations begin with choices for the GL parameter κ, vortex multiplicity p, lattice type (square, triangular, etc.) and mean induction $\bar{B}$. In general we use a flux line lattice (FLL) in the xy-plane with primitive lattice vectors $\mathbf{R}_{10} = x_1\hat{x}$ and $\mathbf{R}_{01} = x_2\hat{x} + y_2\hat{y}$ where $|\mathbf{R}_{10} \times \mathbf{R}_{01}| = x_1 y_2 = S$. We determined the periodicity starting from the film interior but it holds for the free space region outside the sample and it is worth noting that for any z-position $\frac{1}{S}\int_S \mathbf{B}(\mathbf{r}_\perp, z) \cdot \hat{z}\, da = \bar{B}$. Finally, when we work with the FLL model we use the order parameter modulus squared $\omega = |\psi|^2$. We have included mesh plots of the local induction and order parameter for different configurations in Figs. 29–32.

In Abrikosov's [17] ground breaking work on type-II superconductors he found that a bulk sample near H_{c2} will have a minimum free energy if the unit cell is a square. In that case the primitive lattice vectors are $\mathbf{R}_{10} = \sqrt{S}\hat{x}$ and $\mathbf{R}_{01} = \sqrt{S}\hat{y}$. Later Kleiner *et al.* [18] found that the close packed triangular lattice, with $x_2 = \frac{1}{2}x_1$ and $y_2 = \frac{\sqrt{3}}{2}x_1$, is slightly lower in energy and gives the true minimum.

In the low induction regime the inter-vortex spacing, $\sim \sqrt{S}$, is large and the fields will be nearly radially symmetric. We can replace the unit cell with an equal area circular cell (CC) that has a radius, R, defined by $\pi R^2 = S$. In this regime we assume the physical quantities will be fully radially symmetric, e.g., $\mathbf{B} = \mathbf{B}(r_\perp, z)$ and $\mathbf{j}_\perp = j_\theta(r_\perp, z)\,\hat{\theta}$, and we use the order parameter $f = |\psi|$.

3.3 Supervelocity

The supercurrents that circulate around a vortex are given by $\mathbf{j} = -|\psi|^2\,\mathbf{Q}$. The supervelocity of the condensate, introduced in Sec. 2.6, is an important quantity in our work and we repeat its definition (this time in reduced units)

$$\mathbf{Q}(\mathbf{r}_\perp, z) \equiv \mathbf{A}(\mathbf{r}_\perp, z) - \frac{1}{\kappa}\nabla\varphi(\mathbf{r}_\perp, z)\ . \tag{18}$$

While $\mathbf{Q}$ can have a z-dependence, we only consider equilibrium cases where $\mathbf{Q}(\mathbf{r}_\perp, z) = \mathbf{Q}_\perp(\mathbf{r}_\perp, z)$, i.e., $Q_z = 0$ which in turn means $j_z = 0$ and $\frac{\partial \varphi}{\partial z} = \kappa A_z$. Close to a vortex core all fields will be radially symmetric and the order parameter phase will be $\varphi = p\theta$. Then $\nabla\varphi = \frac{p}{r_\perp}\hat{\theta}$ and the supervelocity will be dominated by the phase gradient: $\mathbf{Q} \approx -\frac{p}{\kappa r_\perp}\hat{\theta}$. From this it is obvious that $\mathbf{Q}$ is singular at $r = 0$. However, the two physical quantities involving the supervelocity, the current $-|\psi|^2 \mathbf{Q}$ and (reduced unit) kinetic energy density term $|\psi|^2 |\mathbf{Q}|^2$, are dominated by the small-$r_\perp$ behavior of the order parameter, and both go to zero as $r_\perp \to 0$. Also, from Eq. (18), if we exclude the singularities, $\nabla \times \mathbf{Q} = \mathbf{B}$. Examining the curl at a vortex core and applying Stokes's theorem we find $\nabla \times \left(-\frac{p}{\kappa r_\perp}\hat{\theta}\right) = -\frac{p2\pi}{\kappa}\delta_2(r_\perp)\hat{z}$. In reduced units (see Sec. A.2) we have $\Phi_0 = \frac{2\pi}{\kappa}$. For a lattice of p-quanta vortices, the complete expression for the curl of the supervelocity is

$$\nabla \times \mathbf{Q} = \mathbf{B} - p\Phi_0 \sum_{m,n} \delta_2(\mathbf{r}_\perp - \mathbf{R}_{mn})\hat{z}\,. \tag{19}$$

In the vortex lattice the magnetic flux through the 2D primitive unit cell is given by $\int_S \mathbf{B}\cdot\hat{z}da = \bar{B}S = p\Phi_0$, where S is the area of the unit cell. Then from Eq. 19 we find $\int_S (\nabla \times \mathbf{Q})\cdot\hat{z}da = \bar{B}S - p\Phi_0 = 0$. Again applying Stokes's theorem we find $\oint_C \mathbf{Q}\cdot d\mathbf{l} = 0$ for any contour that encloses an area nS and includes n vortices. In the language of fluid dynamics $\mathbf{Q}$ is the velocity field of the fluid (the condensate), $\oint_C \mathbf{Q}\cdot d\mathbf{l}$ is the circulation and $\nabla \times \mathbf{Q}$ is called the vorticity of the fluid. In general the circulation is non-zero but it vanishes for a contour enclosing a unit cell.

The supervelocity can be split into two parts:

$$\mathbf{Q}(\mathbf{r}_\perp, z) = \mathbf{Q}_A(\mathbf{r}_\perp) + \mathbf{q}(\mathbf{r}_\perp, z) \tag{20}$$

where

$$\mathbf{Q}_A(\mathbf{r}_\perp) \equiv \frac{\bar{B}}{2}\hat{z} \times \mathbf{r}_\perp - \frac{1}{\kappa}\nabla\varphi(\mathbf{r}_\perp)\,. \tag{21}$$

$\mathbf{Q}_A$ is called the Abrikosov supervelocity and is part of the solution to the linearized GL equation (see Appendix F). Eq. (20) defines $\mathbf{q}$ and it can be described as the variation of the supervelocity from $\mathbf{Q}_A$. We then have

$$\nabla \times \mathbf{Q}_A = \bar{B}\hat{z} - p\Phi_0 \sum_{m,n} \delta_2 \left(\mathbf{r}_\perp - \mathbf{R}_{mn}\right) \hat{z} \tag{22}$$

and

$$\nabla \times \mathbf{q} = \mathbf{B}\left(\mathbf{r}_\perp, z\right) - \bar{B}\hat{z}\,. \tag{23}$$

Finally, the average vorticities of these velocity fields over the unit cell vanish: $\int_S \nabla \times \mathbf{Q}_A \cdot \hat{z} da = 0$ and $\int_S \nabla \times \mathbf{q} \cdot \hat{z} da = 0$.

4 Bulk Samples

The iterative methods we employ to solve the GL equations for the mixed state in type-I films, which are discussed in Sec. 5, require having a convergent result for bulk samples. The bulk result may not be an equilibrium solution but it satisfies the GL equations for our choices of κ, $\bar{B}$, vortex lattice type, etc. In a certain sense one could say we start with $d \to \infty$ and then relax the result to the appropriate finite thickness. In this section on bulk samples we present our methods to acquire these convergent (if not equilibrium) results. In addition, we present some interesting results for the bulk case and fill in missing information on lattices of doubly quantized vortices in bulk type-II superconductors.

In bulk type-II superconductors, mixed states in which the vortices carry more than one flux quantum are unstable with respect to the usual vortices that carry a single flux quantum. Near the upper critical field this result was established by Abrikosov [17], while near the lower critical field it is implied by Matricon's [19] calculations for isolated vortices. As far as we are aware, there have been no explicit calculations within Ginzburg-Landau theory for lattices of multiply quantized vortices at magnetic field values between these two limits, but since there is no reason to believe that such lattices should be stable at intermediate fields, there has been no reason to carry out the calculations.

The formal developments we present are an extension of Brandt's work in Ref. [20]. In Sections 4.2 and 4.3 we describe how Brandt's Ansatz and iteration scheme for singles are modified for doubles. In Sections 4.4 and 4.5 we discuss algorithm issues and programming details. We present alternative methods to finding the solutions to the GL equations in Sections 4.6 and 4.7. In Sec. 4.8 we offer illustrative results

for order parameter and magnetic induction profiles, as well as the Gibbs free energy, for doubles and singles in a type-II superconductor. In Appendix H we discuss the solutions of the linearized GL equations, which serve as initial values for the iterative calculations.

In Sec. 3 we introduced our notation on vector quantities. In bulk samples all fields are uniform in the z-direction, and in this section we simplify the notation by dropping the subscript on the position vector in the xy-plane: $\mathbf{r} = \mathbf{r}_\perp$. In addition any vector quantity in bold is assumed to be in the xy-plane, e.g., $\mathbf{Q} = \mathbf{Q}_\perp$. The one exception is for the induction, which in a few instances has been written in bold. However, in bulk it is always true, for the sample setup we consider, that $\mathbf{B}(\mathbf{r}) = B(\mathbf{r})\,\hat{z}$.

4.1 Overview

Our goal is to find the solution to the two GL equations. They are coupled, second order, non-linear partial differential equations. In gauge invariant form and in terms of the real valued fields $f(\mathbf{r}) = |\psi(\mathbf{r})|$ and $\mathbf{Q}(\mathbf{r})$ we have

$$\frac{1}{\kappa^2}\nabla^2 f = f\,|\mathbf{Q}|^2 - f + f^3 \tag{24}$$

$$\nabla \times (\nabla \times \mathbf{Q}) = -f^2\mathbf{Q}\,. \tag{25}$$

These are local equations but their solution gives a stationary point for the overall free energy of the sample. We start with a choice of GL parameter κ, mean sample induction $\bar{B}$ and vortex lattice type. We express f (or $\omega = f^2$) and $\mathbf{Q}$ as expansions of orthogonal basis functions. We iteratively solve for the coefficients corresponding to these basis functions such that they satisfy Eq. (24) and Eq. (25). In order that we find the minimum of the free energy we need a good initial guess; that initial guess is the solution to the linearized GL equation.

4.2 Form of the Solutions to the GL Equation

Consider a vortex in which the phase of the order parameter changes by $2\pi p$ on circling the vortex core. If that core is at the origin, then the order parameter behaves as $\psi \sim r^p e^{ip\theta}$ as $r \to 0$ (see Appendix E) and the modulus squared order parameter as $\omega \equiv |\psi|^2 \sim r^{2p}$. Brandt [20] thoroughly worked out the singles case and we include part of his Ansatz for reference.

$$\omega(\mathbf{r}) = \sum_{\mathbf{K}} a_{\mathbf{K}} \left[1 - \cos(\mathbf{K} \cdot \mathbf{r})\right] \tag{26}$$

$$B(\mathbf{r}) = \bar{B} + \sum_{\mathbf{K}} b_{\mathbf{K}} \cos(\mathbf{K} \cdot \mathbf{r}) \ . \tag{27}$$

In this work we focus on the $p = 2$ case. Brandt's work suggests that for a flux line lattice with one vortex per primitive cell we adopt the Ansatz

$$\omega(\mathbf{r}) = \sum_{\mathbf{K}} a_{\mathbf{K}} \left[1 - \cos(\mathbf{K} \cdot \mathbf{r})\right]^2 \tag{28}$$

in which $\mathbf{r}$ is a two-dimensional vector and where $\mathbf{K}$ runs over reciprocal lattice vectors excluding the origin (as will be the case for all sums over $\mathbf{K}$ henceforth). This form satisfies the requirements of periodicity and fourth-power behavior near vortex cores. It turns out to be useful to express this with only first powers of cosines,

$$\omega(\mathbf{r}) = \sum_{\mathbf{K}} a_{\mathbf{K}} \left[\frac{3}{2} - 2\cos(\mathbf{K} \cdot \mathbf{r}) + \frac{1}{2}\cos(2\mathbf{K} \cdot \mathbf{r})\right] \ . \tag{29}$$

In Appendix F we show for small r the induction satisfies $B(\mathbf{r}) \approx B(0) - \frac{1}{2\kappa}\omega(\mathbf{r})$, so $B(0) - B(r) \sim r^4$. This small-r behavior suggests the form for the deviation from mean induction, $b(\mathbf{r}) = B(\mathbf{r}) - \bar{B}$,

$$b(\mathbf{r}) = \sum_{\mathbf{K}} b_{\mathbf{K}} \left[2\cos(\mathbf{K}\cdot\mathbf{r}) - \frac{1}{2}\cos(2\mathbf{K}\cdot\mathbf{r}) \right] \tag{30}$$

again, with only first powers of cosines). Note that $B(0) = \bar{B} + \frac{3}{2}\sum_{\mathbf{K}} b_{\mathbf{K}}$.

As discussed in Sec. 3.3, the supervelocity can be decomposed as $\mathbf{Q}(\mathbf{r}) = \mathbf{Q}_A(\mathbf{r}) + \mathbf{q}(\mathbf{r})$, see Eqs. (20)–(23), and the deviation from the Abrikosov form has the property that $\nabla \times \mathbf{q}(\mathbf{r}) = b(\mathbf{r})$. This last relation implies

$$\mathbf{q}(\mathbf{r}) = \sum_{\mathbf{K}} b_{\mathbf{K}} \frac{\hat{\mathbf{z}}\times\mathbf{K}}{|\mathbf{K}^2|} \left[2\sin(\mathbf{K}\cdot\mathbf{r}) - \frac{1}{4}\sin(2\mathbf{K}\cdot\mathbf{r}) \right] . \tag{31}$$

The mean induction $\bar{B}$ fixes the area of the lattice unit cell, through $S = 2\Phi_0/\bar{B}$. The unit cell has primitive lattice vectors $\mathbf{R}_{10} = x_1\hat{x}$, $\mathbf{R}_{01} = x_2\hat{x} + y_2\hat{y}$ and in those terms $S = (\mathbf{R}_{10}\times\mathbf{R}_{01})\cdot\hat{z} = x_1 y_2$. The general reciprocal lattice vector is $\mathbf{K}_{mn} = 2\pi\left[m y_2\hat{x} + (m x_2 + n x_1)\hat{y}\right]/S$.

As will be detailed in the following sections, there are additional challenges when solving for the doubly quantized vortices compared to the singles case. These challenges only increase when looking at higher quanta vortices and we do not go beyond $p = 2$. However, knowing the behavior at the vortex core we can write the Ansatz for triply quantized vortices:

$$\omega(\mathbf{r}) = \sum_{\mathbf{K}} a_{\mathbf{K}} \left[\frac{5}{2} - \frac{15}{4}\cos(\mathbf{K}\cdot\mathbf{r}) + \frac{3}{2}\cos(2\mathbf{K}\cdot\mathbf{r}) - \frac{1}{4}\cos(3\mathbf{K}\cdot\mathbf{r}) \right] \tag{32}$$

$$b(\mathbf{r}) = \sum_{\mathbf{K}} b_{\mathbf{K}} \left[\frac{15}{4}\cos(\mathbf{K}\cdot\mathbf{r}) - \frac{3}{2}\cos(2\mathbf{K}\cdot\mathbf{r}) + \frac{1}{4}\cos(3\mathbf{K}\cdot\mathbf{r}) \right] \tag{33}$$

$$\mathbf{q}(\mathbf{r}) = \sum_{\mathbf{K}} b_{\mathbf{K}} \frac{\hat{\mathbf{z}}\times\mathbf{K}}{|\mathbf{K}^2|} \left[\frac{15}{4}\cos(\mathbf{K}\cdot\mathbf{r}) - \frac{3}{2}\cos(2\mathbf{K}\cdot\mathbf{r}) + \frac{1}{4}\cos(3\mathbf{K}\cdot\mathbf{r}) \right] \tag{34}$$

Then in this case we have $S = 3\Phi_0/\bar{B} = x_1 y_2$. In a similar fashion the higher order Ansätze can be constructed.

4.3 GL Equations and Iterative Solution Scheme

The Ginzburg-Landau mean free energy density $\bar{F}$, referenced from the Meissner state, may be expressed in gauge-invariant form as

$$\bar{F}\left(T,\bar{\mathbf{B}}\right)=\left\langle \frac{1}{2}-\omega+\frac{1}{2}\omega^{2}+\frac{\left|\nabla\omega\right|^{2}}{4\kappa^{2}\omega}+\omega\left|\mathbf{Q}\right|^{2}+\left|\mathbf{B}\right|^{2}\right\rangle \tag{35}$$

where the angular brackets denote integration over a two-dimensional unit cell, $\langle\cdots\rangle=\frac{1}{S}\int_{S}\cdots dx\,dy$. Extremalization of $\bar{F}$ leads to the Ginzburg-Landau equations, Eqs. (15) and (16), and following Brandt we add stabilizing terms ($2\kappa^{2}\omega$ and $\overline{\omega}B$, respectively) to both sides of these equations yielding:

$$\left(-\nabla^{2}+2\kappa^{2}\right)\omega=2\kappa^{2}\left[2\omega-\omega^{2}-\omega\left|\mathbf{Q}\right|^{2}-\frac{\left|\nabla\omega\right|^{2}}{4\kappa^{2}\omega}\right] \tag{36}$$

$$\left(\nabla^{2}-\overline{\omega}\right)B=\left(\omega-\overline{\omega}\right)B+\left(\nabla\omega\times\mathbf{Q}\right)\cdot\hat{z}\,. \tag{37}$$

where $\overline{\omega}$ is the mean value of the order parameter. Getting Eq. (37) from Eq. (16) is not obvious and we derive the result in Appendix I. Brandt describes these versions of the GL equations as inhomogeneous London-like equations.

The first GL equation leads to an iterative equation for $a_{\mathbf{K}}$. We multiply Eq. (36) by $\cos\left(\mathbf{K}\cdot\mathbf{r}\right)$ and integrated over the unit cell. The orthogonality relation

$$\left\langle \cos\left(\mathbf{K}\cdot\mathbf{r}\right)\cos\left(\mathbf{K}'\cdot\mathbf{r}\right)\right\rangle =\frac{1}{2}\delta_{\mathbf{K},\mathbf{K}'}$$

enables us to do the integral on the left analytically. Rearranging leads to an identity which we treat as a step in an iterative solution for $a_{\mathbf{K}}$,

$$a_{\mathbf{K}}:=\frac{2\kappa^{2}}{\left|\mathbf{K}\right|^{2}+2\kappa^{2}}\left\langle \left(-2\omega+\omega^{2}+\omega Q^{2}+\frac{\left(\nabla\omega\right)^{2}}{4\kappa^{2}\omega}\right)\cdot\cos\left(\mathbf{K}\cdot\mathbf{r}\right)\right\rangle +\frac{1}{4}a_{\mathbf{K}/2}\,. \tag{38}$$

If $\mathbf{K}/2$ is not a reciprocal lattice vector then $a_{\mathbf{K}/2}\equiv 0$. Eq. (38) should be compared

with the corresponding relation for singly quantized vortices, Eq. (11) in Ref. [20], the only difference is the last term and a factor of two on the integrand.

The next step in the iterative scheme is to rescale all of the $a_{\mathbf{K}}$ by the same factor, so as to minimize F. This goes through without modification from Brandt's version

$$a_{\mathbf{K}} := a_{\mathbf{K}} \left\langle \omega - \omega Q^2 - g \right\rangle / \left\langle \omega^2 \right\rangle \,. \tag{39}$$

Similarly, we multiply Eq. (37) by $\cos(\mathbf{K}\cdot\mathbf{r})$ and integrate over the unit cell leading to the iterative solution for $b_{\mathbf{K}}$

$$b_{\mathbf{K}} := -\frac{\left\langle [(\omega-\overline{\omega})\, B(\mathbf{r}) + (\nabla\omega \times \mathbf{Q})\cdot\hat{z}] \cos(\mathbf{K}\cdot\mathbf{r}) \right\rangle}{\left(|\mathbf{K}|^2 + \overline{\omega}\right)} + \frac{1}{4} b_{\mathbf{K}/2} \,. \tag{40}$$

Again, if $\mathbf{K}/2$ is not a reciprocal lattice vector then the coefficient $b_{\mathbf{K}/2} \equiv 0$.

The GL equations are solved, in principle, by cycling through Eqs. (38), (39), and (40) until the coefficients converge to the desired level of precision. In practice we find that the equations as written do not usually converge to a physical solution; however, by "mixing" the $a_{\mathbf{K}}$ that comes out of (38) with the value from the prior iteration (and likewise for the $b_{\mathbf{K}}$ produced by (40)) the convergence of the algorithm is much improved, though at the cost of more iterations. We have not attempted to determine optimal mixing parameters. Taking 90% of the prior iteration plus 10% of the current iteration is sufficient for every calculation we have carried out so far. We validated our implementation by comparing results to other minimization methods (described in Sec. 4.7).

Even with mixing, it is crucial to have a good initial guess for the $a_{\mathbf{K}}$ and $b_{\mathbf{K}}$. Brandt has demonstrated [20] that the solution of the linearized GL equations for the $a_{\mathbf{K}}$, together with $b_{\mathbf{K}} = 0$ for all $\mathbf{K}$, serves well for the initial values for single, and we find the same to be true for doubles. Constructing solutions to the linearized GL equations for doubles in terms of the $a_{\mathbf{K}}$ is not trivial, and we detail our method

in Appendix H. The solution to the linearized GL equations is used to begin the iteration cycle in Eq. (39).

4.4 Implementation Issues

In order to have a finite computational problem the expansions for ω, b, and $\mathbf{q}$ must be truncated; and the iterations involve integrals over the unit cell which must be numerically evaluated. These two issues are related. For singles, it is sufficient to carry out the quadrature by summation of values on a grid aligned with the primitive lattice vectors, and to include in the expansions only $|\mathbf{K}| \leq K_{\max}$ with $K_{\max}$ chosen so that the number of reciprocal lattice vectors is slightly less than the number of points in the integration grid (this comes from the Nyquist criterion, see Brandt [20]). For doubles the situation is more complicated.

Observe that the expansion (29) for ω can be rearranged so that it has nearly the same form as for singles,

$$\omega(\mathbf{r}) = \sum_{\mathbf{K}} \left[2a_{\mathbf{K}} - \frac{1}{2} a_{\mathbf{K}/2} \right] \left[1 - \cos(\mathbf{K} \cdot \mathbf{r}) \right] . \tag{41}$$

When $\mathbf{K}$ is a fundamental, as defined following Eq. (38), $a_{\mathbf{K}/2} \equiv 0$. Eqs. (28), (29) and (41) are identical for infinite sums, but they are different when truncated. As discussed in Appendix H, the $a_{\mathbf{K}}$ that solve the linearized GL equations for doubles do not fall off in a Gaussian manner like they do for singles; however, the $2a_{\mathbf{K}} - \frac{1}{2}a_{\mathbf{K}/2}$ are approximately Gaussian (see Fig. 27). This motivates the following truncation scheme for constructing ω when evaluating the integrals over the unit cell: use Eq. (41), including in the sum reciprocal lattice vectors with $|\mathbf{K}| \leq K_{\max}$ except for fundamentals with $K_{\max}/2 < |\mathbf{K}| \leq K_{\max}$. Expressions analogous to Eq. (41) exist for b and $\mathbf{q}$, namely

$$b(\mathbf{r}) = \sum_{\mathbf{K}} \left[2b_{\mathbf{K}} - \frac{1}{2} b_{\mathbf{K}/2} \right] \cos(\mathbf{K} \cdot \mathbf{r}) \tag{42}$$

$$\mathbf{q}(\mathbf{r}) = \sum_{\mathbf{K}} \left[2b_{\mathbf{K}} - \frac{1}{2} b_{\mathbf{K}/2} \right] \sin(\mathbf{K} \cdot \mathbf{r}) \frac{\hat{\mathbf{z}} \times \mathbf{K}}{|\mathbf{K}^2|}, \tag{43}$$

and we apply the same truncation scheme.

We conclude this section with a warning. It is tempting to define $c_{\mathbf{K}} \equiv 2a_{\mathbf{K}} - \frac{1}{2}a_{\mathbf{K}/2}$, $d_{\mathbf{K}} \equiv 2b_{\mathbf{K}} - \frac{1}{2}b_{\mathbf{K}/2}$, and carry out iterative calculations for those quantities, by moving the $\frac{1}{4}a_{\mathbf{K}/2}$ from the right side of Eq. (38) to the left (and likewise for Eq. (40)): the resulting equations have exactly the form of Eqs. 11 and 13 from Ref. [20] for the iterations of the coefficients for singles. Doing this invariably leads to a "singles-like" solution ($\omega \sim r^2$ and $B(0) - B(r) \sim r^2$ for small r) which is inconsistent with the assumed forms of $\bar{B}$, $\mathbf{Q}_A$ and S; in addition this unphysical solution is a free energy saddle point rather than a minimum.

4.5 Programming Details

The method outlined in Sec. 4.3 involves calculations of quantities like $\omega(\mathbf{r})$, $B(\mathbf{r})$, $\mathbf{Q}(\mathbf{r})$, etc. on a finite grid and numerical integrations (in cases where analytic integrals do not exist, e.g., $\langle \omega |\mathbf{Q}|^2 \rangle$). We implemented these calculations and the entire iterative algorithm using Matlab ®. Our code is written in Matlab m-files, meaning they are executed as scripts. We did compare a simple loop implementation in Matlab to a vectorized implementation in GNU Octave and found only a slight improvement in execution speed. Our working version is in Matlab as a mix of vectorized and for-loop calculations, all contained in 10 m-files and a total of 1008 lines of code.

4.6 Low Induction Regime and the Circular Cell

For bulk type-II superconductors the triangular lattice is the lowest energy lattice. However, as one goes to a lower mean induction the vortices get further and further apart. The area of a unit cell for a lattice of p-quanta vortices (one vortex per unit cell) is given by $S = p\Phi_0/\bar{B}$ and the inter-vortex spacing has $x_1 \propto 1/\sqrt{\bar{B}}$. Once x_1 is

much larger than λ and ξ, most of the unit cell, aside from the near core region, has $B(\mathbf{r}) \to 0$ and $|\psi(\mathbf{r})| \to \psi_\infty$ (see Eq. (7)). In this limit the vortex-vortex interaction goes to zero and the relative positions of vortices is less important, i.e., $B(\mathbf{r}) \approx B(r)$ and $|\psi(\mathbf{r})| \approx |\psi(r)|$ for all locations. The area of the core region ($r < \max(\lambda, \xi)$) relative to the area, S, of the unit cell area gets quite small. Ideally we would have fine sampling at the core and coarse sampling between vortices where different $\mathbf{r}$ values give nearly identical contributions to the free energy. Alternatively, we can replace the unit cell in Cartesian coordinates with a radially symmetric unit cell in cylindrical coordinates. The radius of this circular cell (CC) is defined by $\pi R^2 = S$. In addition to the small r behavior summarized in Table 1 on page 20 we have conditions at the cell boundary, $r \to R$:

1. $\frac{df}{dr} \to 0$.
2. $j = \frac{dB}{dr} \to 0$. In cylindrical coordinates we have $\nabla \times (B\hat{z}) = -\frac{dB}{dr}\hat{\theta} = \mathbf{j}$.
3. $\oint \mathbf{A}(r) \cdot d\mathbf{l} = p\Phi_0$ for a circular contour of radius R, so $A(R) = \frac{\overline{B}}{2}R$.

4.6.1 Fourier Ansatz

For the flux line lattice (FLL) in Cartesian coordinates we use a Fourier Ansatz where orthogonality of the basis functions is fundamental to the implementation. For the circular cell we have $f(r) = |\psi(r)|$, $\mathbf{B}(r) = B(r)\hat{z}$, $\mathbf{A} = A(r)\hat{\theta}$ and $\mathbf{j} = j(r)\hat{\theta}$. Again, we follow Brandt [21] and below we reproduce his singles Ansatz. The order parameter is expanded in terms of the unknown coefficients f_G and the basis functions $f_m(r)$:

$$f(r) = \sum_{m=1}^{M} f_G f_m(r) \tag{44}$$

$$f_m(r) = \sin(G_m r), \; G_m = \frac{\pi(2m-1)}{2R}. \tag{45}$$

For the induction terms it will prove useful later if we define the induction basis functions $b_{r,n}(r)$ and $b_{z,n}(r)$,

$$b_{r,n}(r) = \sin(K_n r),\ K_n = \frac{\pi n}{R} \tag{46}$$

with $b_{z,n}(r) = \frac{1}{r}\frac{d}{dr}[r b_{r,n}(r)]$, or

$$b_{z,n}(r) = \frac{1}{r}\left[\sin(K_n r) + K_n r\cos(K_n r)\right]. \tag{47}$$

Then the magnetic related fields are expanded in terms of the unknown coefficients a_K

$$B(r) = \sum_{n=1}^{N} a_K b_{z,n}(r) + \overline{B} \tag{48}$$

$$A(r) = \sum_{n=1}^{N} a_K b_{r,n}(r) + \frac{\overline{B}}{2} r \tag{49}$$

$$Q(r) = \sum_{n=1}^{N} a_K b_{r,n}(r) + \frac{\overline{B}}{2} r - \frac{p}{\kappa r}, \tag{50}$$

where p is the fluxoid multiplicity. Finally, the supercurrent (with a sign correction to Brandt's [21] Eq. (10)) is

$$j(r) = \sum_{n=1}^{N} a_K \frac{(1 + K_n^2 r^2)\sin(K_n r) - K_n r\cos(K_n r)}{r^2}. \tag{51}$$

While it is confusing to use $a_{\mathbf{K}}$ for the FLL order parameter and a_K for the CC induction terms, in both cases we maintain Brandt's original definitions. With this Fourier CC Ansatz the first GL equation, Eq. (12) can be written in polar coordinates as: $\frac{1}{\kappa^2}\left(\frac{d^2 f}{dr^2} + \frac{df}{dr}\right) = fQ^2 - f + f^3$. Similar to the flux line lattice a stabilizing term

is added to give:

$$\left(-\frac{d^2}{dr^2}+\kappa^2\right) f = \kappa^2\left(-fQ^2+2f-f^3\right)+\frac{df}{dr}\,. \tag{52}$$

The second GL equation becomes simply

$$j = -f^2 Q\,. \tag{53}$$

An integral over the unit cell involves $2\pi\int_0^R \cdots r\,dr$ and sines and cosines are not orthogonal. However, the GL equations apply locally and we can use an integral where the basis functions are orthogonal, $\int_0^R \cdots dr$, to isolate the f_G and a_K coefficients. Doing so gives

$$f_G := \frac{2}{G_m^2+\kappa^2}\int_0^R \left[\kappa^2\left(-fQ^2+2f-f^3\right)+\frac{df}{dr}\right]\sin\left(G_m r\right)\,dr\,. \tag{54}$$

The iteration expression for the a_K comes from isolating an $a_K K_n^2 \sin\left(Kr\right)$ term in Eq. (51). We define $j_2 = j - \sum_{n=1}^{N} a_K K_n^2 \sin\left(K_n r\right)$

$$j_2\left(r\right) = \sum_{n=1}^{N} a_K \frac{\sin\left(K_n r\right) - K_n r\cos\left(K_n r\right)}{r^2} \tag{55}$$

to get

$$a_K := \frac{1}{K_n^2+1}\left\{a_K - 2\int_0^R \left[f^2 Q + j_2\right]\sin\left(K_n r\right)\,dr\right\}\,. \tag{56}$$

To evaluate the numerical integrals in Eqs. (54) and (56) we grid with uniform spacing and $r_i = \left(i-1/2\right)\frac{R}{N_r}$ with $i = 1, 2, \ldots, N_r$.

Doubly quantized vortices will have small r behavior $f\left(r\right) \sim r^2$ and $B\left(0\right) - B\left(r\right) \sim r^4$ (see Table 1 on page 20). This behavior motivates our choice of an Ansatz for $f\left(r\right)$ and $B\left(r\right)$, which then determines (along with boundary conditions) $A(r)$ from $B = \frac{1}{r}\frac{d}{dr}\left(rA\right)$ and $j(r) = -\frac{dB}{dr}$. We still use Eqs. (44) and (48)–(50) but redefine the

basis functions to match the correct near core behavior. First for the order parameter

$$f_m(r) = 1 - \cos(G_m r),\ G_m = m\frac{\pi}{R}. \tag{57}$$

While for the induction we define the basis functions for doubles as

$$b_{r,n}(r) = \sin(K_n r) - \tfrac{1}{8}\sin(2K_n r) \tag{58}$$

and

$$b_{z,n}(r) = \frac{1}{r}\left[\sin(K_n r) - \tfrac{1}{8}\sin(2K_n r) + K_n r\cos(K_n r) - \tfrac{1}{4}K_n r\cos(2K_n r)\right] \tag{59}$$

where $K_n = \frac{\pi n}{R}$ as in the singles case. We write out the supercurrent expression explicitly as

$$\begin{aligned} j(r) &= \sum_{n=1}^{N} a_K \frac{1}{r^2}\left[\left(1 + K_n^2 r^2\right)\sin(K_n r) - K_n r\cos(K_n r)\right. \\ &\quad \left. - \left(\tfrac{1}{8} + \tfrac{1}{2}K_n^2 r^2\right)\sin(2K_n r) + \tfrac{1}{4}Kr\cos(2K_n r)\right]. \end{aligned} \tag{60}$$

The f_G iteration for doubles is

$$f_G := \frac{2}{G_m^2 + \kappa^2}\int_0^R \left[\kappa^2\left(-fQ^2 + 2f - f^3\right) + \frac{df}{dr}\right]\cos(G_m r)\ dr. \tag{61}$$

For the a_K iteration we again isolate an $a_K K^2 \sin(Kr)$ term but we redefine j_2 as

$$\begin{aligned} j_2(r) &= \sum_{n=1}^{N} a_K \tfrac{1}{r^2}\left[\sin(K_n r) - K_n r\cos(K_n r)\right. \\ &\quad \left. - \left(\tfrac{1}{8} + \tfrac{1}{2}K_n^2 r^2\right)\sin(2K_n r) + \tfrac{1}{4}K_n r\cos(2K_n r)\right]. \end{aligned} \tag{62}$$

Then the update step for the a_K coefficients is identical to Eq. (56). In practice for

inductions $\bar{B} \lesssim \mu_0 H_{c2}/10$ we use the Fourier circular cell rather than the FLL to calculate and compare free energies of singly and doubly quantized vortices.

4.6.2 Bessel Circular Cell Ansatz

For doubly quantized vortices the second GL equation iteration step for the a_K, Eq. (56) with Eq. (62), is unwieldy and we were interested in finding an alternative. As mentioned above, sines and cosines are not orthogonal over the circular unit cell. A more natural choice of basis functions are the Bessel functions of the first kind, J_n, with $\int_0^R J_n\left(\frac{\alpha_{nm}}{R}r\right)\, J_n\left(\frac{\alpha_{np}}{R}r\right)\, r\, dr = \delta_{mp}\frac{R^2}{2}J_{n+1}^2\left(\alpha_{nm}\right)$, where α_{nm} is the m^{th} zero of J_n. We first implemented this for the simpler, singly quantized case. Since the analytic integrals we evaluate involve no mixing of order parameter and magnetic terms we left the first GL equation iteration for the f_G unchanged (the order parameter Ansatz is not changed). So our Bessel circular cell Ansatz is:

$$B\left(r\right) = \sum_{m=1}^{M} d_m J_0\left(\frac{\alpha_{1m}}{R}r\right) + \bar{B} \tag{63}$$

$$A\left(r\right) = \sum_{m=1}^{M} d_m \frac{R}{\alpha_{1m}} J_1\left(\frac{\alpha_{1m}}{R}r\right) + \frac{\bar{B}}{2}r \tag{64}$$

$$Q\left(r\right) = \sum_{m=1}^{M} d_m \frac{R}{\alpha_{1m}} J_1\left(\frac{\alpha_{1m}}{R}r\right) + \frac{\bar{B}}{2}r - \frac{1}{\kappa r} \tag{65}$$

$$j\left(r\right) = \sum_{m=1}^{M} d_m \frac{\alpha_{1m}}{R} J_1\left(\frac{\alpha_{1m}}{R}r\right)\,. \tag{66}$$

The above equations satisfy all the boundary conditions for the vortex core, $r \to 0$ (see Table Table 1 on page 20), and at the cell edge, $r \to R$. We were also fortunate in that J_0 is orthogonal over the zeros of J_1: $\int_0^R\, J_0\left(\frac{\alpha_{1m}}{R}r\right) J_0\left(\frac{\alpha_{1n}}{R}r\right)\, r\, dr = \delta_{mn}\frac{R^2}{2}\left[J_0\left(\alpha_{1m}\right)\right]^2$. We mentioned that the Fourier Ansatz supercurrent, Eq. (56), is unwieldy and we

suggest comparison with the Bessel Ansatz, Eq. (66). Using the second GL equation Eq. (37) we arrived at the iterative equation to update the d_m coefficients:

$$d_m = \frac{-\int_0^R \left((2f\nabla f \times \mathbf{Q}) \cdot \hat{z} + \left(f^2 - \bar{f}^2 \right) B \right) J_0 \left(\frac{\alpha_{1m}}{R} r \right) r \, dr}{\left[J_0 \left(\alpha_{1m} \right) \right]^2 \left(\left(\frac{\alpha_{1m}}{R} \right)^2 + \bar{f}^2 \right)} \tag{67}$$

where the integral is evaluated numerically on a uniform grid. Even though $f(r)$ uses a different set of basis functions it is calculated on the same grid as the induction terms and we are able to use the results of the f_G iterations without additional calculations. For the singles we do achieve matching between the Fourier Ansatz and the Bessel Ansatz when comparing free energies.

Unfortunately, for doubly quantized vortices with a Bessel Ansatz we ran into obstacles that we could not surmount. For doubles we have $f(r) \sim r^2$ and $B(0) - B(r) \sim r^4$. In this coordinate system we have $B = \frac{1}{r}\frac{d}{dr}(rA)$ and $j = -\frac{dB}{dr}$, so $A(r) \sim r + Cr^5$ and $j(r) \sim r^3$. Note that J_0 is unique among the integral J_n in that at $r = 0$ it is a maximum with $J_0(0) = 1$ ($J_n(0) = 0$ for all other n). We again were fortunate with the singles Bessel Ansatz because the small r-behavior for $J_0(0) - J_0(r) \sim r^2$ exactly matches our induction $B(0) - B(r) \sim r^2$, and $B(0)$ is a maximum. Our efforts to use combinations of J_n and J_m that matched the small r conditions on B, A and j along with the requirements that $B = \frac{1}{r}\frac{d}{dr}(rA)$ and $j = -\frac{dB}{dr}$ proved unsuccessful and we abandoned this approach for doubly quantized vortices. Our primary goal with the Bessel Ansatz was to simplify the iteration step for the induction terms in the doubles case, Eq. (56) with Eq. (62). However, it is a novel approach and in the singles case matches the Fourier Ansatz results.

4.7 Other Minimization Methods

In general there are many methods that could be used to minimize the Ginzburg-Landau free energy functional. We chose Brandt's iterative method [20, 21] because

he has long worked in this field, his results are found to be in good agreement with experiment, and is relatively easy to implement and modify. However, we have explored other methods and while we did not end up replacing the Brandt iterative method these alternatives were used in part as a validation of our results.

The primary alternative we used was a conjugate gradient algorithm from Hager and Zhang [22], but we also used a Newton's method implementation. For a general background on optimization we refer to Nocedal and Wright [23]. The methods are both direct minimizations of the GL free energy functional, $\bar{F}$, with respect to the $a_{\mathbf{K}}$ and $b_{\mathbf{K}}$ coefficients from our Ansatz. We define a vector of these coefficients, $\mathbf{v} \equiv \{a_{\mathbf{K}}\} \cup \{b_{\mathbf{K}}\}$ and a corresponding gradient $\nabla_{\mathbf{v}} = \Sigma_i \hat{\imath}_i \frac{\partial}{\partial v_i}$. The scalar valued function $\bar{F} = \bar{F}(\mathbf{v})$ is a minimum at $\mathbf{v} = \mathbf{v}^*$ and

$$\nabla_{\mathbf{v}} \bar{F}|_{\mathbf{v}=\mathbf{v}^*} = 0 \tag{68}$$

Newton's method starts from an initial guess for a solution $\mathbf{v}_0$ and has an update step:

$$\mathbf{v} := \mathbf{v} - H^{-1} \nabla_{\mathbf{v}} \bar{F}$$

where H is the Hessian matrix, with $H_{ij} = \frac{\partial^2 \bar{F}}{\partial v_i \partial v_j}$ (note that it is symmetric). We don't explicitly calculate the inverse Hessian but find $\mathbf{u}$ such that $\nabla_{\mathbf{v}} \bar{F} = H\mathbf{u}$ (sometimes written as a backslash, or left division: $\mathbf{u} = H \setminus \nabla_{\mathbf{v}} \bar{F}$). This system of linear equations could be solved via Gaussian elimination for the unknown u_i but in practice we use a Cholesky factorization. Each iteration requires a calculation of $\nabla_{\mathbf{v}} \bar{F}$ and H. It is well known that Newton's method is best suited if the initial choice for $\mathbf{v}$ is close to the solution. As such we used it to test perturbed solutions from our Brandt based scheme. In addition the calculation step $\mathbf{u} = H \setminus \nabla_{\mathbf{v}} \bar{F}$ is costly.

Hager and Zhang have made their above cited CG_Descent algorithm freely available and we use their C-code implementation. In brief, with CG_Descent the user

(in this case, us) writes the code for the function to be minimized (called the cost function) and the code for its gradient. These are then passed in as pointers to function to the CG_Descent routine. The two user supplied functions have fixed argument lists. In our case we need to carry along data besides the vector of coefficients that vary in size and value for different minimization calls—for example the set of $\mathbf{K}$ vectors. Our solution to the fixed argument list was to save the CG_Descent file as a C++ file and change the pointer to function with a pointer to base class. The calls to the cost function and its gradient in our C++ base class have the same arguments as the C version but all the other required data is included as class data members. We then inherit from this base class depending whether we are doing singles or doubles and whether a flux line lattice or a circular cell. Some of the issues we ran into with the Brandt method were also issues for CG_Descent. For example, fine sample spacing means quadrature on a large grid and a large number of coefficients. While the CG_Descent is compiled code, Matlab's internal optimizations of our implementation of the Brandt scheme were able to match it in performance (execution time for CG_Descent was typically 1.5–2 times as long). In the end, we use the CG_Descent as a validation of our Matlab scripts when going to a new calculation regime or a change in Ansatz.

4.8 Results

To illustrate the effectiveness of the calculational scheme described in the previous sections, we will present results for $\kappa = 1$, 4 and 10 for triangular arrays of both doubly and singly quantized vortices. In comparing doubles with singles it is important to do the calculations on an equal footing; with this in mind, in order to have the same spacing between real-space grid points in both calculations we use about twice as many grid points for doubles than for singles. For $\bar{B}$ greater than about $\mu_0 H_{c2}/5$ we typically use 32 points along each primitive lattice vector for singles and 46 for doubles. Singles

and doubles then have the same $K_{\max}$ but the doubles calculation includes twice as many reciprocal lattice vectors as the singles calculation. A typical singles calculation converges in about 50 iterations while the doubles require about four times as many. At lower inductions the area of the vortex core becomes considerably less than the area of the unit cell, and in order to represent the solutions well the real-space sampling needs to be refined by increasing the number of grid points per unit cell edge to 64 or 96 for singles and with proportionally increased numbers for doubles. The growth in the number of grid points and reciprocal lattice vectors puts a practical lower limit on the mean induction of about $\mu_0 H_{c2}/10$. Below this value we use the circular cell to calculate free energies.

In Fig. 4 we show the order parameter and induction along a line connecting two adjacent vortices at $\bar{B} = \mu_0 H_{c2}/2$ for both doubles and singles with $\kappa = 1$. As one would expect, the vortex cores for doubles are wider than for singles. In Figs. 5, 6 and 7 we present the Gibbs free energy density $\tilde{G}$ in the full range of applied fields $H_{c1} \leq H_a \leq H_{c2}$ for triangular singles and doubles (see Appendix C, Eq. (113) for a definition of $\tilde{G}$). The applied field H_a is calculated in the same manner as in Refs. [24, 20], based on the virial theorem of Doria, Gubernatis, and Rainer [25]. These results confirm that doubles are thermodynamically unstable in bulk type-II superconductors.

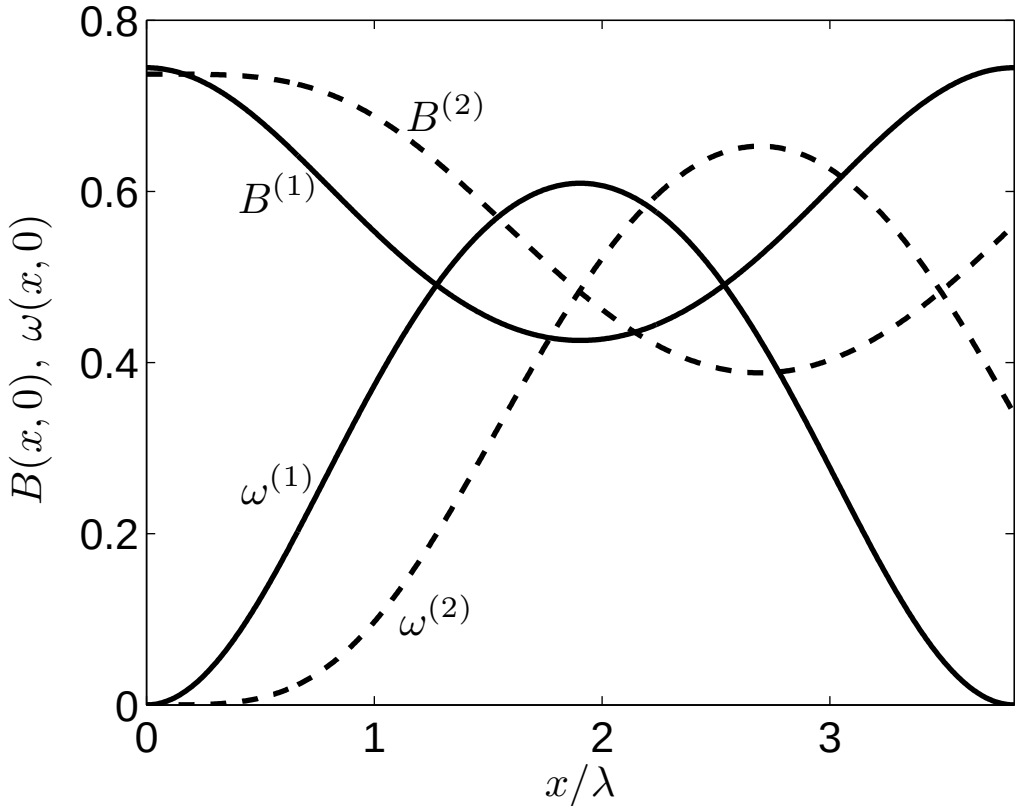

Figure 4: Cross-section $\kappa = 1$

Cross-section for $\kappa = 1$ and $\bar{B} = 0.5H_{c2}$ along the $\mathbf{R}_{10}$ direction (i.e., $y = 0$). The solid lines are for singly quantized vortices and dashed lines for doubly quantized vortices.

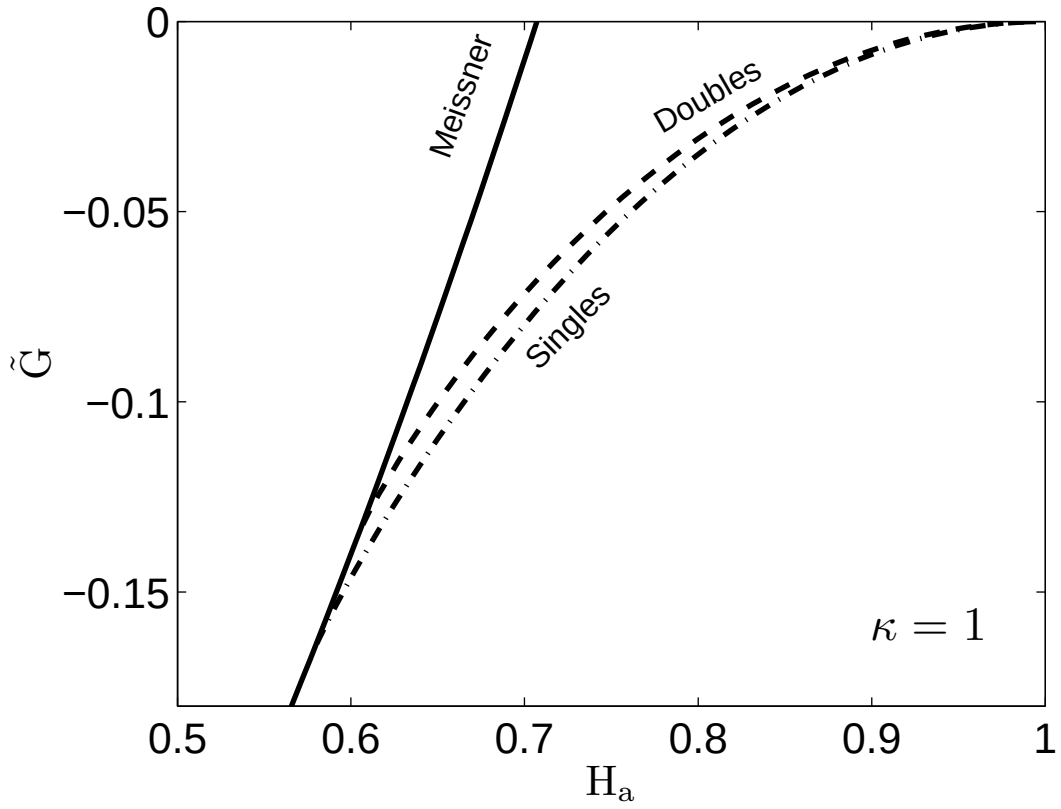

Figure 5: Gibbs Energy, $\kappa = 1$

Gibbs energy density, $\tilde{G}$, for $\kappa = 1$ and referenced from the normal state, i.e., $\tilde{G}_N = 0$ for all $\mathrm{H_a}$. The solid line is the Meissner state energy. The dot-dash line is for singles with $H_{c1} = 0.58$, the dashed line is for doubles with $H_{c1} = 0.60$ ($H_{c2} = \kappa$ in reduced units). In this and the following Gibbs energy figures notice that the Meissner↔Mixed↔Normal transitions occur such that $d\tilde{G}/dH_a$ is constant, which is a characteristic of a second-order phase transition (no latent heat). But the Meissner↔Normal transitions ($H_c = 1/\sqrt{2}$ in reduced units) have a discontinuous $d\tilde{G}/dH_a$, indicative of a first-order phase transition, in this case with $\frac{1}{V}L_f = \frac{1}{2}\mu_0 H_c^2$. Also, in this plot, and subsequent plots with different κ, the Meissner and normal states will differ in Gibbs energy density by $\tilde{G}_M - \tilde{G}_N = H_a^2 - \frac{1}{2}$.

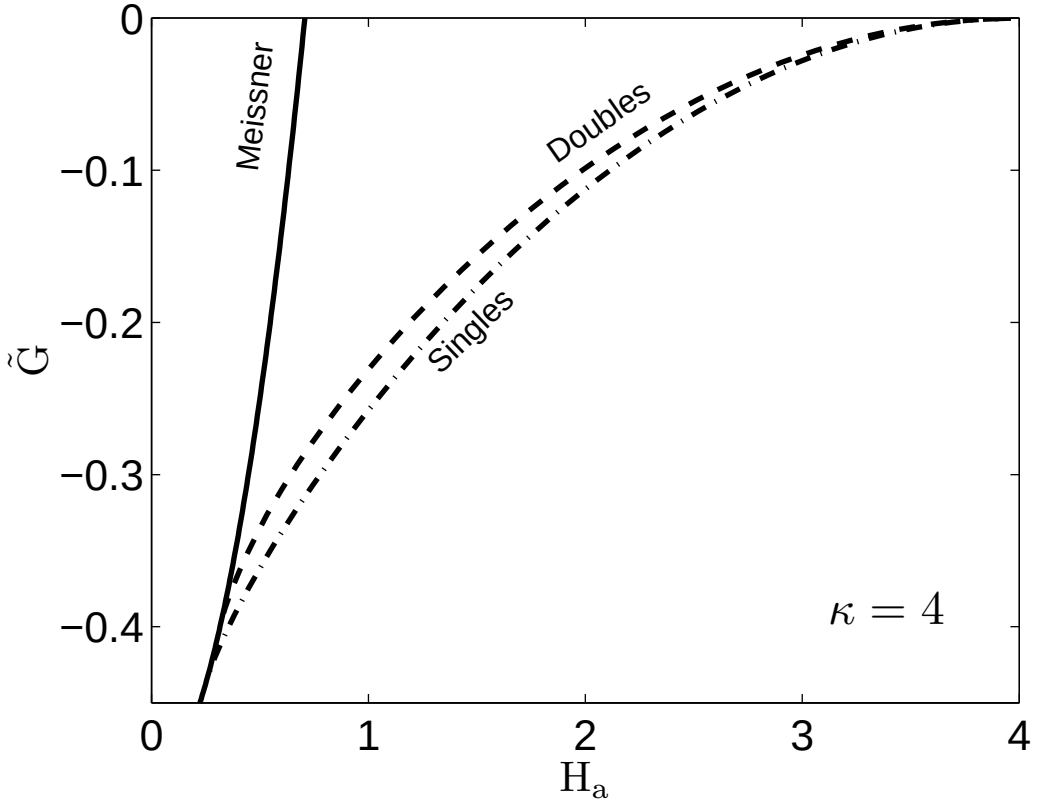

Figure 6: Gibbs Energy , $\kappa = 4$

Same as Fig. 5 but with $\kappa = 4$. The lower critical fields are $H_{c1} = 0.26$ for singles, and $H_{c1} = 0.32$ for doubles.

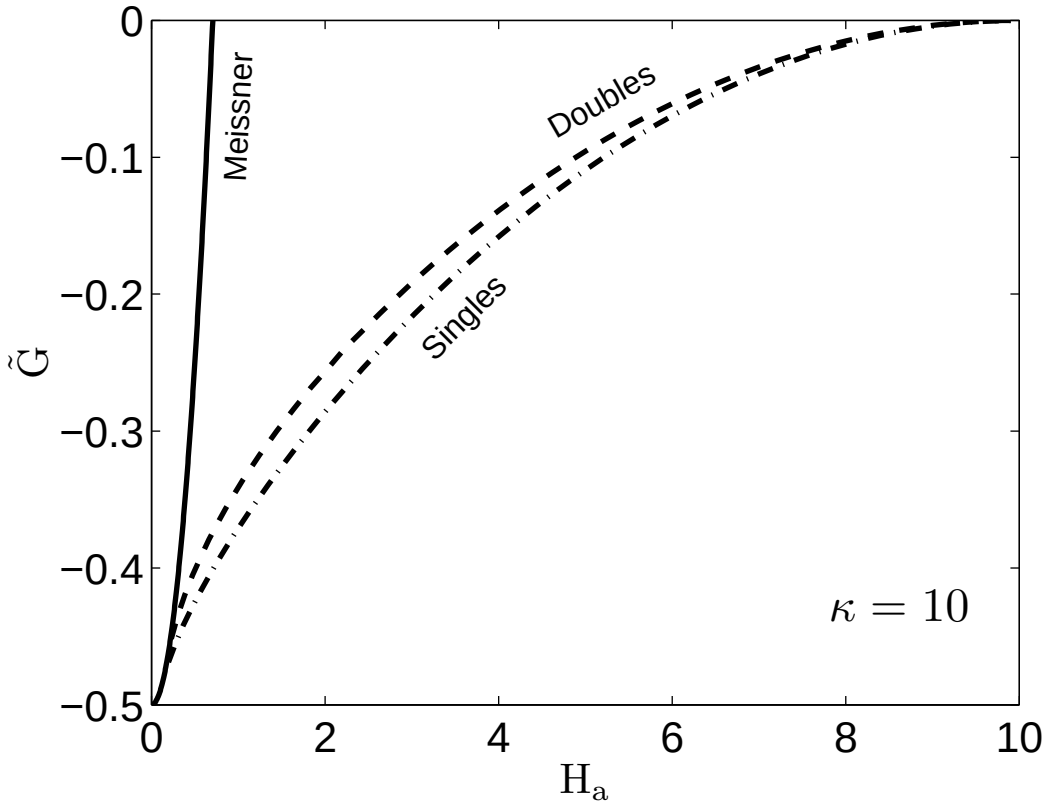

Figure 7: Gibbs Energy, $\kappa = 10$

Same as Fig. 5 but with $\kappa = 10$. The lower critical fields are $H_{c1} = 0.16$ for singles, and $H_{c1} = 0.20$ for doubles.

In Figs. 8, 9 and 10 we plot the magnetization as a function of applied field, and for both singles and doubles we find $\int M\,dH = -\frac{1}{2}\mu_0 H_c^2$ (SI units). The magnetic susceptibility is defined as $\chi = \frac{\partial M}{\partial H_a}$, and in the region $H_{c1} \leq H_a \leq H_{c2}$ the susceptibility is positive (we plot $-M$) and, except just above H_{c1}, the susceptibility is lower for doubles. For $H_a < H_{c1}$ the sample is in the Meissner state and $\chi = -1$ while just above H_{c1} we have $\chi \to +\infty$. This theoretical infinite susceptibility is derived in many works (e.g., De Gennes [9] Sec. 3-2) and we will briefly summarize De Gennes's analysis. Just above H_{c1} few flux lines have penetrated the sample and the vortex spacing is very large (i.e., $\sqrt{S} \gg \lambda, \xi$). There is virtually no interaction between vortices and minimal cost to adding more flux lines. A small change in the applied field can make a large change in the induction. However, as the applied field and vortex density increases repulsive forces come into play and there is a higher cost to adding more vortices (increasing $\bar{B}$). In the region $H_{c1} \ll H_a < H_{c2}$, as mentioned above, doubly quantized vortices have lower susceptibility than singles. This is indicative of the greater repulsion between vortices for doubles in this regime.

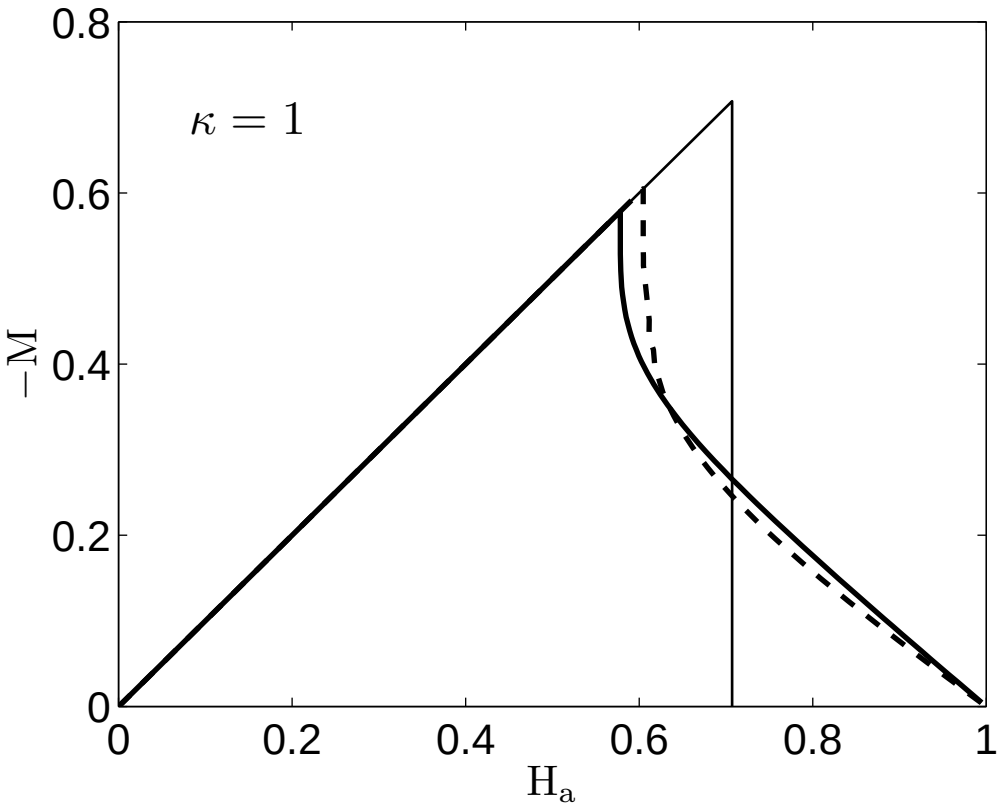

Figure 8: Magnetization Curve, $\kappa = 1$

Magnetization curve for $\kappa = 1$. The thick solid line is for singles with $H_{c1} = 0.58$, the thick dashed line for doubles with $H_{c1} = 0.60$. The thin solid line is for a Meissner↔Normal transition at $H_a = H_c$.

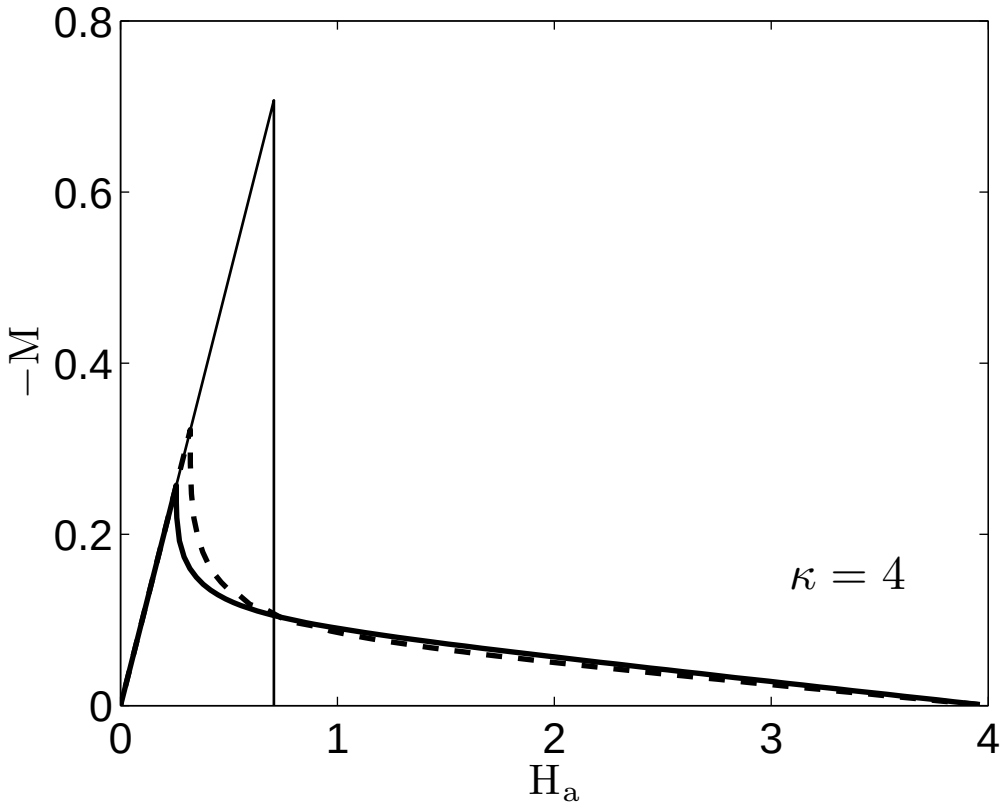

Figure 9: Magnetization Curve, $\kappa = 4$

Magnetization curve for $\kappa = 4$. Thick solid line is for singles $H_{c1} = 0.26$, the thick dashed lines for doubles with $H_{c1} = 0.32$. The thin solid line is for a Meissner↔Normal transition at $H_a = H_c$.

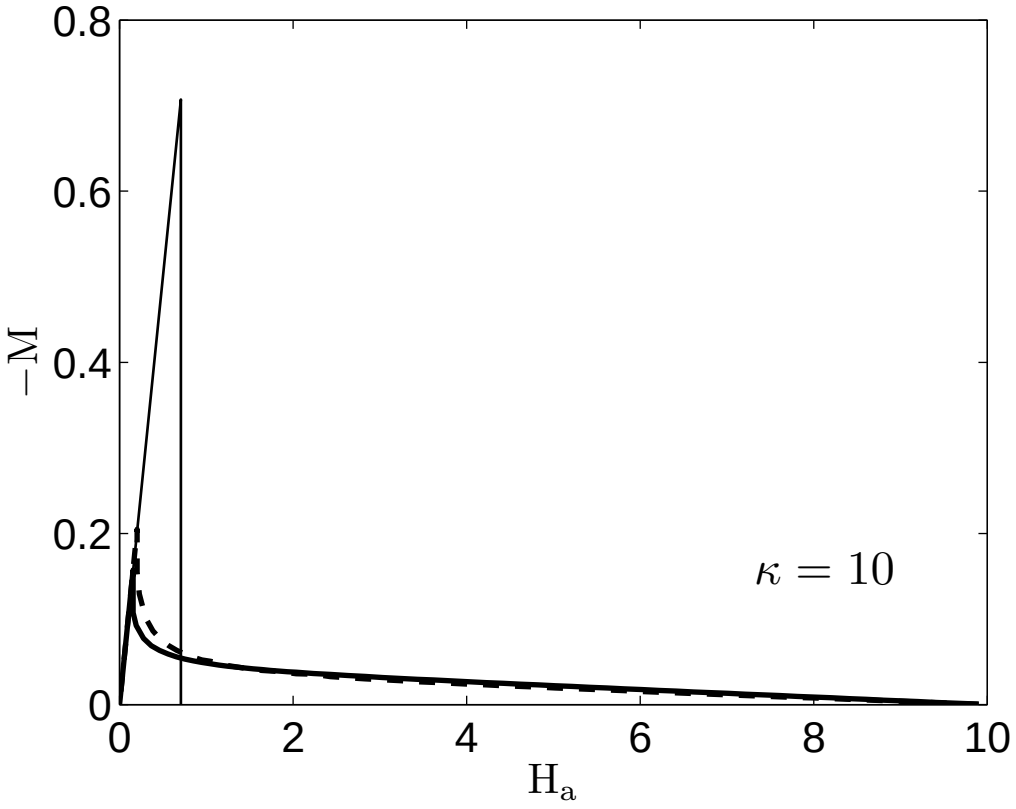

Figure 10: Magnetization curve, $\kappa = 10$.

Magnetization curve for $\kappa = 10$. The thick solid line is for singles $H_{c1} = 0.16$, the thick dashed line is for doubles with $H_{c1} = 0.20$. The thin solid line is for a Meissner↔Normal transition at $H_a = H_c$.

The calculations also yield convergent results for type-I superconductors but in such cases all vortex states are unstable with respect to the Meissner state. Even so, it is instructive to look at these results. Fig. 11 shows the order parameter and induction plots for $\kappa = 0.5$. The Gibbs free energy, Fig. 12, does show that vortex states are unstable with respect to the Meissner state but that doubles are lower in energy than for singles. Also, in this non-equilibrium case we have $H_{c2} \leq H_a \leq H_{c1}$. Finally, the magnetization plot for type-I singles and doubles, Fig. 13, shows a negative susceptibility for all values of applied field. However, even in this non-equilibrium path from Meissner state to normal state we have $\int M\, dH = -\frac{1}{2}\mu_0 H_c^2$. We show in Appendix C.2 that the area under the magnetization curve is equal to the difference in free energy between the Meissner and normal states, i.e., the condensation energy.

To conclude this section on bulk superconductors, we have produced precise numerical solutions to the GL equations consisting of infinite lattices of singly and doubly quantized vortices in bulk superconductors. The calculations can be carried out efficiently for mean inductions down to about 1% of the upper critical value. Although such solutions of the GL equations never globally minimize the GL free energy for bulk superconductors, we expect they will be useful as starting points for solving the GL equations in film geometry.

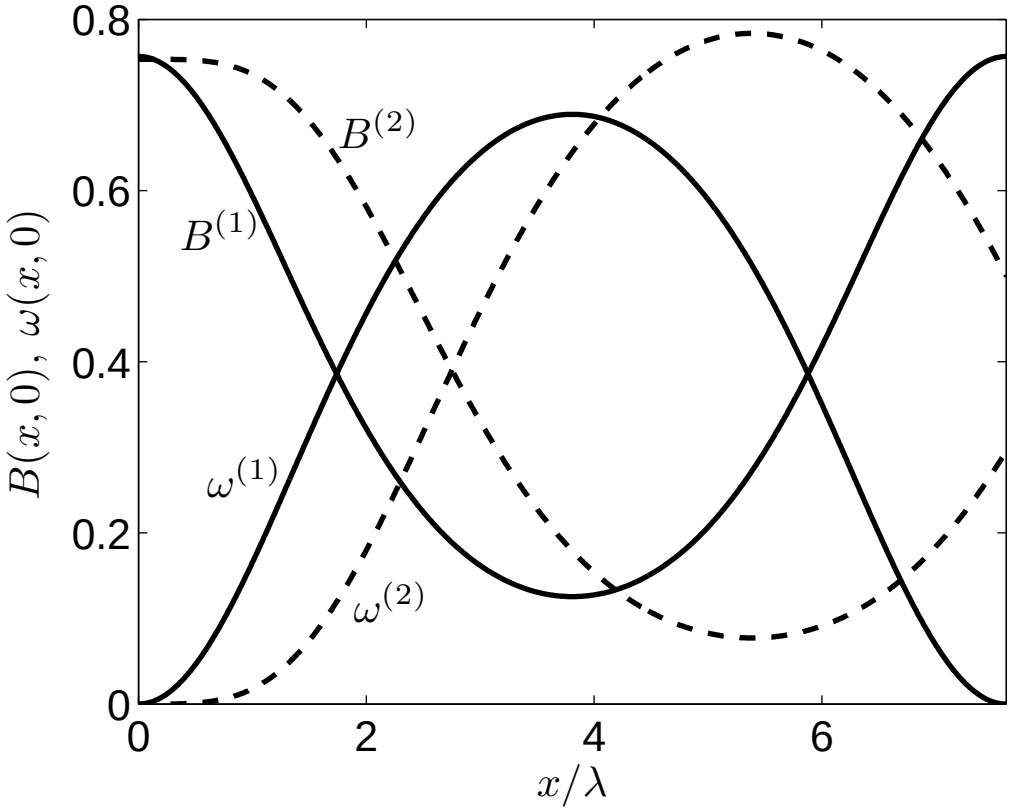

Figure 11: Cross-section $\kappa = 0.5$

Cross-section for $\kappa = 0.5$ and $\bar{B} = 0.5H_{c2}$. The solid lines are for singly quantized vortices and dashed lines for doubly quantized vortices.

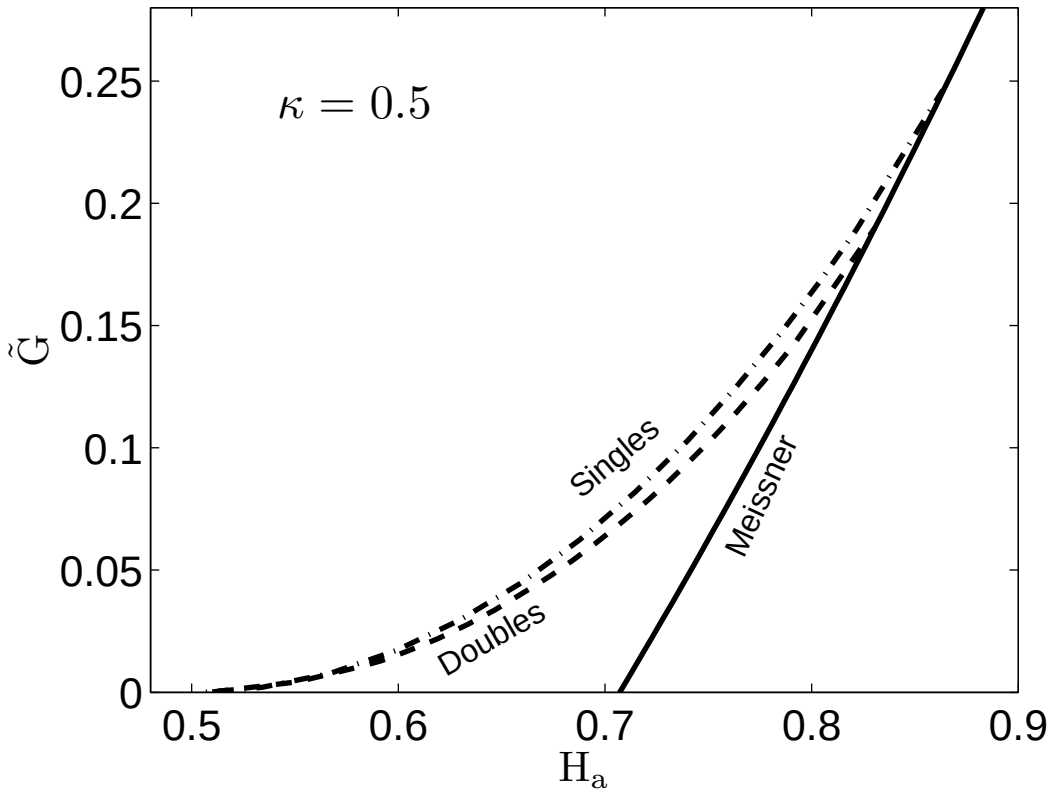

Figure 12: Gibbs Energy, $\kappa = 0.5$

Mean Gibbs free energy density, $\tilde{G}$, for $\kappa = 0.5$ referenced from normal state, i.e., $\tilde{G}_N = 0$ for all H_a. The solid line is the Meissner state energy. The dot-dash line is for singles in the mixed state between $H_{c1} = 0.86$, the dashed line is for doubles in the mixed state with $H_{c1} = 0.83$, and $H_{c2} = \kappa = 0.5$ in both cases. See Fig. 5 for more details. Note: with $\kappa < 1/\sqrt{2}$ the vortex state in bulk samples is always unstable with respect to the normal or Meissner states, but we find a lattice of doubly quantized vortices is lower in Gibbs energy than a lattice of singles.

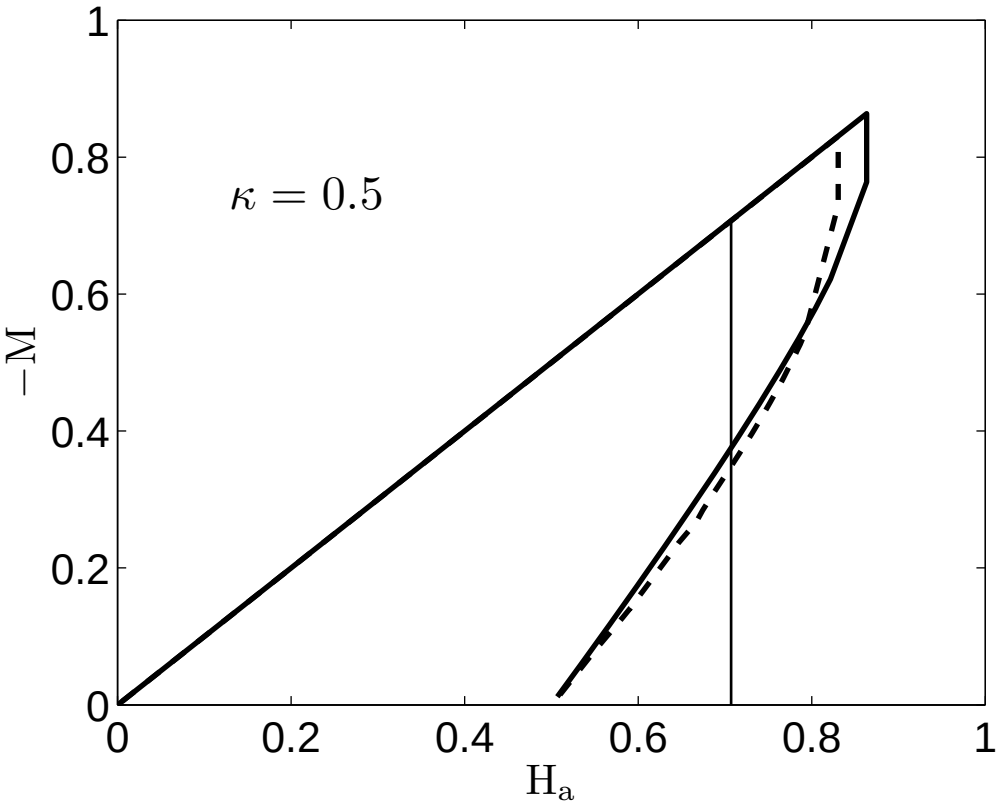

Figure 13: Magnetization Curve, $\kappa = 0.5$

Magnetization curve for $\kappa = 0.5$ in bulk. The thick solid line is for singles in the mixed state with $H_{c1} = 0.86$, the dashed lines is for the mixed state of doubles with $H_{c1} = 0.83$, and $H_{c2} = \kappa = 0.5$ in both cases. The thin solid line is for a Meissner↔Normal transition at $H_a = H_c$. Even though the mixed state is a non-equilibrium phase all three curves have $-\int M\, dH = \frac{1}{2}$, which in standard units gives $\frac{1}{2}\mu_0 H_c^2$, the Condensation Energy. A reminder: in reduced units for all κ, $H_{c2} = \kappa$ and $H_c = 1/\sqrt{2}$ (see Appendix A.2).

5 Films

As mentioned in the introduction, thin films of a bulk type-I superconductor subject to a perpendicular magnetic field can behave like bulk type-II superconductors, in that they develop a vortex lattice in which each vortex carries a single flux quantum. Pioneering theoretical treatments by Tinkham [8] and Maki [26] applied Ginzburg-Landau theory in the vicinity of the critical field where the order parameter vanishes and showed that the transition between normal state and superconducting state is continuous, just as in bulk type-II materials. Lasher [27] established that a triangular vortex lattice is favored near the upper critical field for sufficiently thin films and found that a sequence of vortex structures, starting with a square lattice and continuing to more complicated structures, develops with increasing thickness en route to the intermediate state. Some years later Callaway [28] pointed out that Lasher had not considered the most general Abrikosov-type solutions to the linearized GL equations, and he carried out a comprehensive analysis of the phase diagram for periodic vortex arrays close to the upper critical field. In the low-field limit, Pearl's [29, 30] treatment of isolated vortices within London theory shows that vortices in a sufficiently thin film have a long-range repulsion; this repulsion should lead to the development of a triangular vortex lattice. Remarkably, the structure of the vortex phase diagram at intermediate magnetic field strengths, where solution of the full GL equations is required, has remained an open theoretical problem. That problem is partially solved in the present work.

On the experimental side, magnetic decoration experiments on type-I films of Pb, Sn, and In by Dolan and Silcox [31, 32, 33] in the mid-1970s could distinguish

between lattices of single fluxoid vortices (which appear to be disordered due to pinning), intermediate state flux structures, and what they referred to as "transitional" or "multifluxoid" structures. Within linearized GL theory one can construct a flux structure phase diagram with the GL parameter κ on one axis and the product of film thickness and the square root of the magnetic field on the other [27]; Dolan and Silcox's results were reasonably consistent with this phase diagram. However, there have been no experimental observations of the distinct single-fluxoid vortex lattice structures predicted by linearized GL theory. In fact it is not obvious whether the vortex structures found by Lasher and Callaway at intermediate thicknesses survive on reducing the magnetic field. The calculations within the full GL theory presented in this work offer detailed guidance for experimental studies of such structures in type-I films.

Interesting experimental results have also appeared at very low fields. Hasegawa *et al.* [34] applied electron holography to examine the magnetic field in the space above flux structures in Pb films. They found evidence for vortices with more than one flux quantum (which they denoted MQF-A) as well as flux structures that seemed more likely to be associated with normal regions of finite cross-section (which they denoted MQF-B). "Multiply-quantized" (also known as "giant") vortices are known to arise in various circumstances. Holes in a superconductor parallel to the field trap vortices with greater fluxoid number as their radii increase [35]. Arrays of holes ("antidots") can trap multiple flux quanta per hole under appropriate conditions [36]. The repulsion of vortices from a film edge can lead to the formation of an equilibrium giant vortex in the center of a small, thin disk [37] and in other laterally confined geometries [38]. Metastable giant vortices develop in field-cooling of small cylinders [39]. None of these seem relevant to the experiment of Hasegawa *et al.*, and the search for stable lattices of multiply-quantized vortices in the phase diagram for type-I films without lateral confinement or defects was another motivation for the present work.

It is noteworthy that a bulk GL superconductor with $\kappa = 1/\sqrt{2}$ and at the critical field exhibits massive (in fact complete) degeneracy with respect to vortex configurations [40]. Luk'yanchuk [41] has carried out a thorough analysis of corrections to the GL functional, together with deviations of κ and the magnetic field from their critical values, in breaking the degeneracy. He noted that demagnetization effects also break the degeneracy, but did no calculations along those lines. A film geometry corresponds to maximum demagnetization, so it may be interesting to compare the vortex phase diagram for films with $\kappa \approx 1/\sqrt{2}$ with the phase diagrams that follow from the analysis by Luk'yanchuk.

In the present work we take the first steps towards filling out the magnetic flux structure phase diagram for the minimal model, isotropic Ginzburg-Landau theory, of thin film type-I superconductors. The competition between various phases is delicate, so precise and accurate free energy calculations for different flux structures are necessary. Consequently, we have followed the approach pioneered by Brandt for vortex lattices in bulk [42] and, more recently, thin film [43] GL superconductors. The squared magnitude of the order parameter, the supervelocity, and the magnetic field are represented as linear combinations of appropriate basis functions. The GL equations then become a set of nonlinear equations which are solved by iteration.

Sec. 5.1 describes the computational method in more detail. Brandt's papers are quite explicit, so we may be brief, and highlight the modest changes we made to Brandt's algorithm for thin film superconductors. The present calculations are restricted to magnetic flux structures consisting of singly-quantized vortices in periodic structures with one vortex per unit cell. We have found that the functional form chosen for the magnetic field in Ref. [43]limits the accuracy of the magnetic field and consequently the free energy, and we offer a correct and computationally convenient alternative. Sec. 5.2 presents the principal results of the calculations, which are based on evaluating the free energy for a large number of points in the space of vortex

lattices structures, film thickness, and applied magnetic fields (or, equivalently, mean inductions). Phase diagrams, free energy densities, and vortex lattice shear moduli are given for $\kappa = 0.5$ and 0.25. Other values of the GL parameter could have been considered but the calculations become significantly more challenging at smaller values of κ; and with results for just two values, some trends with variation of κ may be deduced. Sec. 5.3 offers various decompositions of the free energy density to facilitate the physical interpretation of the flux structure phase diagram. In Sec. 5.5 we summarize the results and note their limitations, indicate some directions for future theoretical work, and offer suggestions for experiments.

5.1 Computational Method

In order to avoid unnecessary repetition of material presented in Ref. [43], we will start by presenting only as much of it needed to make our further developments intelligible. We will first describe in detail our method for lattices of singly quantized vortices then follow with the details for lattices of doubly quantized vortices.

The standard reduced units are employed, defined in Appendix A.2. Note that in these units the upper critical mean induction is κ, and we will sometimes refer to a "reduced" induction $\bar{B}/\kappa$ which in SI units would be defined as $\bar{B}/\mu_0 H_{c2}$. We consider infinite films with $-d/2 < z < d/2$. We use our work on bulk samples in Sec. 4 as the basis for our work on films. One difference is that with a finite thickness sample we still have $\bar{\mathbf{B}} = \bar{B}\hat{z}$, but locally $\mathbf{B} \times \hat{z} \neq 0$. Therefore the variation of the induction is a vector quantity

$$\mathbf{b} = \mathbf{B} - \hat{\mathbf{z}}\bar{B}\,. \tag{69}$$

A key step in Brandt's approach is to decompose the supervelocity as $\mathbf{Q} = \mathbf{Q}_A + \mathbf{q}$ (see Sec. 3.3) with

$$\mathbf{b} = \nabla \times \mathbf{q}\,. \tag{70}$$

As with the bulk case we let S denote both the unit cell area and the unit cell itself, depending on context; for the former, $S = p\Phi_0/\bar{B}$. Note that the mean induction can be expressed as $\bar{B} = \frac{1}{S}\int_S \mathrm{d}x\mathrm{d}y \mathbf{B}(x,y,z)\cdot\hat{\mathbf{z}}$ for any value of z. The free energy per unit volume of superconductor referenced from the normal state is

$$\begin{aligned}\tilde{F}\left(T,\bar{\mathbf{B}}\right) = \frac{1}{Sd}\int_S \mathrm{d}x\mathrm{d}y \int_{-d/2}^{d/2}\mathrm{d}z \left[-\omega + \frac{1}{2}\omega^2 + \frac{|\nabla\omega|^2}{4\kappa^2\omega} + \omega Q^2 + b^2\right] \\ + \frac{2}{Sd}\int_S \mathrm{d}x\mathrm{d}y \int_{d/2}^{\infty}\mathrm{d}z[B^2 - \bar{B}^2]\end{aligned} \tag{71}$$

where the contribution of the first two terms in the first integral is the condensation free energy F_{cond}, that of the next two terms is the kinetic energy of the supercurrent F_{kin}, that of the last term is the internal field energy F_{mag}, and that of the second integral is the stray field energy F_{stray}. In order to determine the phase diagram we will compare the minimum F for different vortex lattice structures with the same value of $\bar{B}$ (and hence S). While the physical fields now have a z-dependence, the problem is the same as for the bulk case, namely, to determine ω, $\mathbf{q}$ and $\mathbf{b}$ that minimize the free energy.

5.1.1 Singly quantized vortices

We first consider the lattice of singly quantized vortices. Brandt's Ansatz for ω, $\mathbf{q}$ and $\mathbf{b}$ is as follows:

$$\omega(\mathbf{r}) = \sum_{\mathbf{K}_\perp, K_z} a_{\mathbf{K}_\perp K_z}\left[1 - \cos\left(\mathbf{K}_\perp\cdot\mathbf{r}_\perp\right)\right]\cos K_z z \tag{72}$$

$$\mathbf{q}(\mathbf{r}) = \sum_{\mathbf{K}_\perp, K_z} b_{\mathbf{K}_\perp K_z}\frac{\hat{\mathbf{z}}\times\mathbf{K}_\perp}{K_\perp^2}\sin\left(\mathbf{K}_\perp\cdot\mathbf{r}_\perp\right)\cos K_z z \tag{73}$$

$$b_z(\mathbf{r}) = \sum_{\mathbf{K}_\perp, K_z} b_{\mathbf{K}_\perp K_z}\cos\left(\mathbf{K}_\perp\cdot\mathbf{r}_\perp\right)\cos K_z z \tag{74}$$

$$\mathbf{b}_\perp(\mathbf{r}) = \sum_{\mathbf{K}_\perp, K_z} b_{\mathbf{K}_\perp K_z}\frac{\mathbf{K}_\perp K_z}{|\mathbf{K}_\perp|^2}\sin\left(\mathbf{K}_\perp\cdot\mathbf{r}_\perp\right)\sin K_z z\,. \tag{75}$$

Here $\mathbf{K}_\perp$ is the set of reciprocal lattice vectors for the vortex lattice and $K_z = (2\pi/d)\,n$ with n running over the whole numbers. Several features of this Ansatz are worth noting. Only two sets of expansion coefficients, $a_{\mathbf{K}_\perp K_z}$ and $b_{\mathbf{K}_\perp K_z}$, are required because $\mathbf{b}$ and $\mathbf{q}$ are linked by (70). The periodicity of the ω combined with the quadratic behavior of ω near the vortices suggests the form of expansion for the $\mathbf{r}_\perp$ dependence in (72), while the boundary condition for the order parameter at a superconductor-insulator interface makes the cosine expansion natural for the z dependence. Eq. (73) leads to supercurrents with, as one would anticipate, only in-plane components, as well as with the appropriate periodicity and behavior near vortex lines. The motivation for the z dependence of the expansions for $\mathbf{b}$ and $\mathbf{q}$ is that $\mathbf{q}$ and b_z are even functions of z while $\mathbf{b}_\perp$ is an odd function.

Inserting (72) and (73) into the first GL equation and applying orthogonality of trigonometric functions leads to coupled nonlinear equations for the expansion coefficients $a_{\mathbf{K}_\perp K_z}$ and $b_{\mathbf{K}_\perp K_z}$ which can be readily cast in the form of equations for the $a_{\mathbf{K}_\perp K_z}$ suitable for solution by iteration: see Eq. (83) below. More equations must come from the second GL equation inside the film, together with $\nabla \times \mathbf{b} = 0$ outside the film and the boundary conditions on the induction. The induction above the film satisfies

$$B_z = \bar{B} + \sum_{\mathbf{K}_\perp} b^{\mathrm{s}}_{\mathbf{K}_\perp} \cos \mathbf{K}_\perp \cdot \mathbf{r}_\perp e^{-K_\perp (z-d/2)} \tag{76}$$

$$\mathbf{B}_\perp = \sum_{\mathbf{K}_\perp} b^{\mathrm{s}}_{\mathbf{K}_\perp} \frac{\mathbf{K}_\perp}{K_\perp} \sin \mathbf{K}_\perp \cdot \mathbf{r}_\perp e^{-K_\perp (z-d/2)}\,, \tag{77}$$

and the continuity-of-B_z boundary condition may be expressed as

$$b^{\mathrm{s}}_{\mathbf{K}_\perp} = \sum_{K_z} b_{\mathbf{K}_\perp K_z} \cos dK_z/2\,. \tag{78}$$

It is convenient to derive the equations for the expansion coefficients by direct minimization of the free energy (including the stray field energy) with respect to the

$b_{\mathbf{K}_\perp K_z}$. Below we reproduce Eqs. (19) through (22) of Ref. [43]

$$\frac{\partial \langle b^2 \rangle}{\partial b_{\mathbf{K}_\perp K_z}} = b_{\mathbf{K}_\perp K_z} \frac{(1+\delta_{n,0})\, K_\perp^2 + (1-\delta_{n,0})\, K_z^2}{2K_\perp^2}$$

$$\frac{\partial \langle \omega Q^2 \rangle}{\partial b_{\mathbf{K}_\perp K_z}} = \frac{P_{\mathbf{K}_\perp n}}{K_\perp^2}$$

$$\frac{1}{d}\frac{\partial \langle F_{stray} \rangle}{\partial b_{\mathbf{K}_\perp K_z}} = b^{\mathrm{s}}_{\mathbf{K}_\perp} \frac{2\cos(\pi n)}{dK_\perp}$$

$$P_{\mathbf{K}_\perp n} = \langle \omega \left[Q_y K_x - Q_x K_y \right] \sin(\mathbf{K}_\perp \cdot \mathbf{r}_\perp) \cos K_z z \rangle \ .$$

From these equations and with $\frac{\partial \tilde{F}}{\partial b_{\mathbf{K}_\perp K_z}} = 0$ at the solution Brandt obtains his Eq. (23) for the $b_{\mathbf{K}_\perp K_z}$ iterations

$$b_{\mathbf{K}_\perp K_z} := \frac{-2P_{\mathbf{K}_\perp n} + c\,\langle \omega \rangle\, b_{\mathbf{K}_\perp K_z} - \frac{2}{d} K_\perp b^{\mathrm{s}}_{\mathbf{K}_\perp} \cos(\pi n)}{\delta_{n,0} K_\perp^2 + \frac{1}{2}(1-\delta_{n,0})\, K_z^2 + c\,\langle \omega \rangle} \ .$$

In these equations the integer n refers to the $K_z = (2\pi/d)\, n$ index.

In order to carry out a calculation of the expansion coefficients it is necessary to truncate the expansion, setting $a_{\mathbf{K}_\perp K_z}$ and $b_{\mathbf{K}_\perp K_z}$ to zero for $\mathbf{K}_\perp$ and K_z outside some range. It is also necessary to approximate the integrals that appear in the iteration equations as finite sums. Those integrals arise from applying orthogonality relations and, ideally, the coefficient truncation and numerical integration could be done consistently, so that the trigonometric functions retained in the expansion are orthogonal with respect to the numerical integration. This is done naturally for the z coordinates of the integration, by making the simplest choice of uniform spacing. In the xy plane Brandt employs a rectangular grid for integration but a circular domain for the allowed $\mathbf{K}_\perp$ values. Though a rectilinear domain for $\mathbf{K}_\perp$ would be more consistent we have followed Brandt's choice, on the grounds that when $K_\perp$ is large the expansion coefficients ought to be small.

What is there to object to in the method described above? In brief, Eq. (73) (and its corollaries Eqs. (74) and (75)) impose periodic boundary conditions in the z direction which are not physically appropriate. According to (75), as the film surface is approached from within, $\mathbf{b}_\perp(\mathbf{r}) \to 0$. This leads to a discontinuity in $\mathbf{b}_\perp$ across the film boundary, as can be seen from Eq. (77), and that discontinuity implies a sheet current density at the film surface which is inconsistent with the GL (or even London) theory description of a superconductor.

The consequences of this flaw in the Ansatz are surprisingly difficult to see—no clear sign of it appears in the results presented by Brandt in Ref. [43], many of which we reproduced independently. When we implemented that method the first suggestion of a problem came when we compared two calculations of the supercurrent which should have given the same results, namely $\mathbf{j} = -\omega\mathbf{Q}$ and $\mathbf{j} = \nabla \times \mathbf{B} = \nabla \times \mathbf{b}$. An example is shown in Fig. 14, for a system at fairly low mean induction. Note that the supercurrent calculated according to $\nabla \times \mathbf{B}$ actually circulates in the wrong direction for some values of z. A hint that the problem was the form of the z dependence in Eqs. (73)–(75), and not simply an error in our implementation as we first supposed, was that the disagreement become more evident as the maximum value of K_z was increased.

Our solution is to replace the cosine expansion for the z-dependence of $\mathbf{q}$ with an expansion in terms of Legendre polynomials of even order, since the latter form a complete, orthogonal set of even functions over a finite interval that allow for nonzero derivatives at the ends of the interval. Instead of Eqs. (73)–(75), take

$$\mathbf{q}(\mathbf{r}) = \sum_{\mathbf{K}_\perp, l} b_{\mathbf{K}_\perp l} \frac{\hat{\mathbf{z}} \times \mathbf{K}_\perp}{K_\perp^2} \sin \mathbf{K}_\perp \cdot \mathbf{r}_\perp P_{2l}(2z/d) \tag{79}$$

$$b_z(\mathbf{r}) = \sum_{\mathbf{K}_\perp, l} b_{\mathbf{K}_\perp l} \cos \mathbf{K}_\perp \cdot \mathbf{r}_\perp P_{2l}(2z/d) \tag{80}$$

$$\mathbf{b}_\perp(\mathbf{r}) = \sum_{\mathbf{K}_\perp, l} b_{\mathbf{K}_\perp l} \frac{-\mathbf{K}_\perp}{K_\perp^2} \sin \mathbf{K}_\perp \cdot \mathbf{r}_\perp \frac{2}{d} P'_{2l}(2z/d) \tag{81}$$

There is an additional benefit of the Legendre polynomial expansion for the accuracy of the calculations. A numerical scheme for z integration which maintains orthogonality of the Legendre polynomials is appropriate for the iterative calculation of the b coefficients, namely, Gauss-Legendre quadrature. The abscissas for Gauss-Legendre quadrature are at zeros of P_n (where n is larger than the highest order used in the Ansatz), and these zeros are more numerous near the film surfaces where the most rapid changes occur for $\mathbf{b}$ and $\mathbf{q}$. Finally, the Legendre polynomials are optimal for our purposes, compared to other sets of polynomials, because they are orthogonal with respect to a constant weight function, just like the trigonometric functions.

We now present the full scheme for generating solutions to the GL equations for films. We use $\langle \cdots \rangle_{\mathrm{U}}$ to denote the volume average over a unit cell by numerical quadrature in which the z abscissas are uniformly spaced, while $\langle \cdots \rangle_{\mathrm{G}}$ is the same, except it employs Gauss-Legendre quadrature for the z coordinate. Angle brackets without a subscript refers to an analytic expression for the volume average over the unit cell. Before beginning the iterative calculations a set of initial $a_{\mathbf{K}_\perp K_z}$ and $b_{\mathbf{K}_\perp l}$ coefficients must be chosen; we will discuss that choice following the iteration scheme.

For the order parameter coefficients we use Brandt's iteration scheme, without modification, but for completeness we include it here. Defining

$$g = |\nabla \omega|^2 / 4\kappa^2 \omega \tag{82}$$

the first GL equation leads to the iteration

$$a_{\mathbf{K}_\perp K_z} := \frac{4\langle (\omega^2 - 2\omega + \omega Q^2 + g) \cos \mathbf{K}_\perp \cdot \mathbf{r}_\perp \cos K_z z \rangle_{\mathrm{U}}}{(\delta_{K_z,0} + 1)((K_\perp^2 + K_z^2)/2\kappa^2 + 1)} \,. \tag{83}$$

This is always followed by an iteration to minimize F by multiplying all the $a_{\mathbf{K}_\perp K_z}$

by the same factor,

$$a_{\mathbf{K}_\perp K_z} := a_{\mathbf{K}_\perp K_z} \langle \omega - g - \omega Q^2 \rangle_{\mathrm{U}} / \langle \omega^2 \rangle_{\mathrm{U}} \,. \tag{84}$$

This step was introduced by Brandt in solving the GL equations in bulk superconductors; if omitted, the calculations generally do not converge.

Next comes the iteration for the $b_{\mathbf{K}_\perp l}$. Our modification of the expansions for $\mathbf{b}$ and $\mathbf{q}$ require corresponding changes to the iteration scheme compared to Ref. [43]. It is convenient to construct some auxiliary quantities such as the stray-field expansion coefficients

$$b^{\mathrm{s}}_{\mathbf{K}_\perp} = \sum_l b_{\mathbf{K}_\perp l} \tag{85}$$

(compare Ref. [43] Eqs. (10) and (21)); a quantity that arises from $\partial \langle \omega Q^2 \rangle / \partial b_{\mathbf{K}_\perp l}$,

$$D_{\mathbf{K}_\perp l} = \langle \omega \left[Q_y K_x - Q_x K_y \right] \sin \mathbf{K}_\perp \cdot \mathbf{r}_\perp P_{2l} \left(2z/d \right) \rangle_{\mathrm{G}} \tag{86}$$

(compare Ref. [43] Eqs. (20) and (22)); and

$$S_{\mathbf{K}_\perp l} = \sum_{l'=0}^{l} b_{\mathbf{K}_\perp l'} 2l' \left(2l' + 1 \right) + \sum_{l'=l+1} b_{\mathbf{K}_\perp l'} 2l \left(2l + 1 \right) \tag{87}$$

which appears in

$$\partial \langle b^2 \rangle / \partial b_{\mathbf{K}_\perp l} = 2 S_{\mathbf{K}_\perp l} / (dK_\perp)^2 + b_{\mathbf{K}_\perp l} / (4l + 1) \tag{88}$$

These last two expressions are rather more complicated than the corresponding Eq. (19) of Ref. [43] because, unlike sines and cosines, the P_{2l} and P'_{2l} are not mutually orthogonal. The second sum in Eq. (87) is finite on account of the truncation of the expansion.

With these definitions the revised iteration scheme is

$$b_{\mathbf{K}_\perp l} := \frac{-2S_{\mathbf{K}_\perp l} - 2D_{\mathbf{K}_\perp l} - 2K_\perp b^{\mathrm{s}}_{\mathbf{K}_\perp}/d + c\,\langle\omega\rangle\, b_{\mathbf{K}_\perp l}}{K_\perp^2/(4l+1) + c\,\langle\omega\rangle} \tag{89}$$

where the constant c and the order parameter mean $\langle\omega\rangle = \sum_{\mathbf{K}_\perp} a_{\mathbf{K}_\perp 0}$ are included to stabilize the iterations (compare Ref. [43] Eq. (23)).

The algorithm is started with an initial guess for the $a_{\mathbf{K}_\perp K_z}$ and $b_{\mathbf{K}_\perp l}$ coefficients. Convergence to the physical solutions is not guaranteed, and in fact it is essential to have good initial values. We have used bulk solutions [20] as initial values for $a_{\mathbf{K}_\perp 0}$ and $b_{\mathbf{K}_\perp 0}$, with the other coefficients initially zero. One repeatedly cycles through Eqs. (83), (84), and (89) until F has converged to an absolute tolerance of 1×10^{-10} or better, which typically requires about 200 iterations. This is slower convergence than is achieved with the cosine Ansatz for the z dependence for the supervelocity. A possibly related matter is that we have not found a suitable expression for the "mixing parameter" c that works well—large enough to maintain stability of the iteration scheme, small enough to allow for reasonably quick convergence—over the entire range of parameters that we have studied. What we do instead is to adjust c during the iteration cycle by monitoring the evolution of F_{mag} and F_{stray}. We have found when either of those field energies increases excessively it is a sign that an instability is developing. A scheme that works reliably is that when either F_{mag} and F_{stray} increases by more than 50% following (89) then c is multiplied by 10 and the b-iteration is re-run; independently, every 30 iterations c is divided by 2.

Although our calculations do not converge as rapidly as those reported in Ref. [43] they always lead to solutions with lower free energies, typically by 0.5% or less (with the same number of coefficients included in both calculations). These small differences are enough to produce noticeable changes in the phase boundaries. Our calculations also have the appealing feature that increasing the l cutoff for the $b_{\mathbf{K}_\perp l}$ always gives

an improved solution; the same is not true of increasing the K_z cutoff for the $b_{\mathbf{K}_\perp K_z}$. Repeating the calculations presented in Fig. 14 yields supercurrent densities from $-\omega\mathbf{Q}$ and $\nabla \times \mathbf{B}$ which are nearly coincident, and which are close to the $-\omega\mathbf{Q}$ values displayed in that figure.

All of the results presented in the following sections are for calculations at $\kappa = 0.5$ and 0.25; even with just those two values for the GL parameter some trends with decreasing κ are evident. Calculations at small κ are considerably more challenging: we have not yet been able to obtained converged solutions at $\kappa = 0.1$.

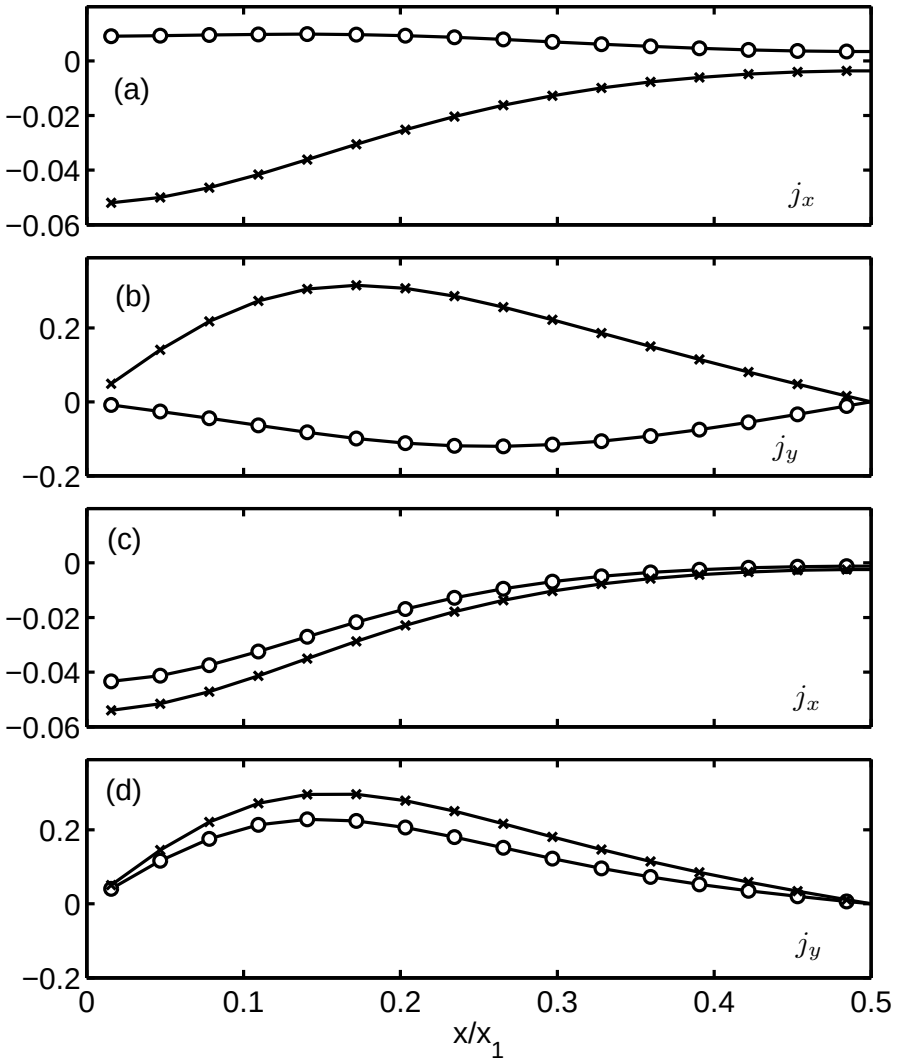

Figure 14: Supercurrent density components

Supercurrent density components j_x and j_y calculated from $-\omega\mathbf{Q}$ (crosses) and $\nabla \times \mathbf{B}$ (circles) from solutions by the method of Ref. [43] for a system with $\kappa = 0.5$, $\bar{B} = 0.4/\kappa$, $d = 4.3$, and a $32 \times 13 \times 9$ grid for real-space sampling. The vortex lattice is triangular, with one primitive translation being $x_1\hat{x}$. In these plots $y = 0.017x_1$, with $z = 0.89d/2$ for (a) and (b) and $z = 0$ for (c) and (d).

5.1.2 Doubly quantized vortices

The Ansatz for lattices of doubly quantized vortices in bulk is modified for films as follows:

$$\omega(\mathbf{r}) = \sum_{\mathbf{K}_\perp, K_z} \left[2a_{\mathbf{K}_\perp, K_z} - \frac{1}{2} a_{\mathbf{K}_\perp/2, K_z} \right] \left[1 - \cos(\mathbf{K}_\perp \cdot \mathbf{r}_\perp) \right] \cos(K_z z) \tag{90}$$

$$b_z(\mathbf{r}) = \sum_{\mathbf{K}_\perp, l} \left[2b_{\mathbf{K}_\perp l} - \frac{1}{2} b_{\mathbf{K}_\perp/2, l} \right] \cos(\mathbf{K}_\perp \cdot \mathbf{r}_\perp) \, P_{2l}(2z/d) \tag{91}$$

$$\mathbf{b}_\perp(\mathbf{r}) = \sum_{\mathbf{K}_\perp, l} \left[2b_{\mathbf{K}_\perp l} - \frac{1}{2} b_{\mathbf{K}_\perp/2, l} \right] \frac{-\mathbf{K}_\perp}{K_\perp^2} \sin(\mathbf{K}_\perp \cdot \mathbf{r}_\perp) \, \frac{2}{d} P'_{2l}(2z/d) \tag{92}$$

$$\mathbf{q}(\mathbf{r}) = \sum_{\mathbf{K}_\perp, l} \left[2b_{\mathbf{K}_\perp l} - \frac{1}{2} b_{\mathbf{K}_\perp/2, l} \right] \frac{\hat{\mathbf{z}} \times \mathbf{K}}{K_\perp^2} \sin(\mathbf{K}_\perp \cdot \mathbf{r}_\perp) \, P_{2l}(2z/d) \tag{93}$$

We then obtain the first GL equation iteration for the $a_{\mathbf{K}_\perp K_z}$ coefficients:

$$a_{\mathbf{K}_\perp K_z} := \frac{2\langle (\omega^2 - 2\omega + \omega Q^2 + g) \cos \mathbf{K}_\perp \cdot \mathbf{r}_\perp \cos K_z z \rangle_{\mathrm{U}}}{(\delta_{K_z,0} + 1)((K_\perp^2 + K_z^2)/2\kappa^2 + 1)} + \frac{1}{4} a_{\mathbf{K}_\perp/2, K_z} \tag{94}$$

If $\mathbf{K}_\perp/2$ is not a reciprocal lattice vector then $a_{\mathbf{K}_\perp/2, K_z} \equiv 0$. As in the singles case Eq. (94) is followed by Eq. (84).

The iterative equation for $b_{\mathbf{K}_\perp l}$ involves several auxiliary quantities (the derivations of the following equations are in Appendix J.3). Replacing Eq. (87) is

$$\begin{aligned} S_{\mathbf{K}_\perp l} \;=\; & \sum_{l'=0}^{l} \left(\frac{17}{4} b_{\mathbf{K}_\perp, l'} - b_{\mathbf{K}_\perp/2, l'} - \frac{1}{4} b_{2\mathbf{K}_\perp, l'} \right) 2l'(2l'+1) \\ & + \sum_{l'=l+1} \left(\frac{17}{4} b_{\mathbf{K}_\perp, l'} - b_{\mathbf{K}_\perp/2, l'} - \frac{1}{4} b_{2\mathbf{K}_\perp, l'} \right) 2l(2l+1) \end{aligned} \tag{95}$$

and replacing Eq. (86) is the expression

$$D_{\mathbf{K}_\perp, l} = \left\langle \omega(\hat{z} \cdot \mathbf{K}_\perp \times \mathbf{Q}) \left[4\sin(\mathbf{K}_\perp \cdot \mathbf{r}_\perp) - \frac{1}{2} \sin(2\mathbf{K}_\perp \cdot \mathbf{r}_\perp) \right] P_{2l}(2z/d) \right\rangle_{\mathrm{G}} \tag{96}$$

The stray-field coefficients, replacing Eq. (85), are given by

$$b^s_{\mathbf{K}_\perp} = \sum_l 2b_{\mathbf{K}_\perp l} - \frac{1}{2} b_{\mathbf{K}_\perp/2,l}$$

Then the desired iterative equation, replacing Eq. (89), is

$$\begin{aligned} b_{\mathbf{K}_\perp l} : \;=\; & \frac{1}{1 + c\,\langle\omega\rangle} \frac{4}{17} \Bigg\{ b_{\mathbf{K}_\perp/2,l} + b_{2\mathbf{K}_\perp,l} + \frac{17}{4} c\,\langle\omega\rangle\, b_{\mathbf{K}_\perp l} \\ & + \frac{4l+1}{K_\perp^2} \left[-2S_{\mathbf{K}_\perp l}/d^2 - D_{\mathbf{K}_\perp l} - 2K_\perp \left(2b^s_{\mathbf{K}_\perp} - \frac{1}{4} b^s_{2\mathbf{K}_\perp} \right) /d \right] \Bigg\} \end{aligned} \tag{97}$$

The discussion in Sec. 4.4 concerning truncation schemes for the sums representing ω, $\mathbf{b}$, and $\mathbf{q}$ is equally germane in film geometry. The calculations for double fluxoid vortex lattices converge more slowly, by roughly a factor of five, than for single fluxoid vortices. That is not unexpected, given that it holds for the bulk calculations. Furthermore, there is a narrower range of parameters in which we have been able to obtained converged results at all; surprisingly, we have encountered difficulties with mean inductions too close to the upper critical value, for which the single fluxoid vortex lattice calculations readily converge.

5.2 Phase Diagrams and Physical Properties

5.2.1 Phase Diagrams

We have carried out a series of calculations at various values of $\bar{B}$ and d, and for several kinds of vortex lattices including triangular, square, rectangular (at various aspect ratios) and two classes of oblique lattices which we will refer to as rhombohedral (which interpolate between triangular and square at fixed unit cell area, maintaining equality of the primitive vector lengths) and sheared-triangular (which interpolate between triangular and rectangular at fixed unit cell area, keeping one primitive

vector fixed). The common feature of the structures considered is that they have one vortex per unit cell, and consequently the coefficients in the expansion of the order parameter (72) are known for a bulk system just below the upper critical field [44]. The vortex structure with lowest free energy turns out to be either triangular, square, or rectangular.

Figs. 15 and 16 show the resulting phase diagrams for $\kappa = 0.5$ and 0.25. The phases found at the upper critical field extend to lower fields, but with the phase boundaries shifting to larger thicknesses as $\bar{B}$ is reduced. At sufficiently low $\bar{B}$ the interval of thickness where the square lattice is stable is seen to vanish on the $\kappa = 0.25$ phase diagram; and the same almost certainly holds for $\kappa = 0.5$, but at a lower value of $\bar{B}$ than we have considered. Contours of constant aspect ratio within the rectangular phase are shown as dotted lines. On the $\kappa = 0.5$ phase diagram we have included a dashed line where we speculate that the rectangular phase ends and more complicated structures with more than one flux quantum per unit cell begin; in drawing that line we are assuming that the aspect ratio within the rectangular phase is constant at the boundary with the adjacent phase.

Within linearized GL theory $d\bar{B}^{1/2}$ is constant on every phase boundary [27]. That is not a terrible approximation, but the numerical results are noticeably different, with the domain of stability of the triangular phase reduced compared to the linearized GL theory. The critical endpoint for the square to rectangular transition is a qualitative feature that only emerges from the full GL treatment.

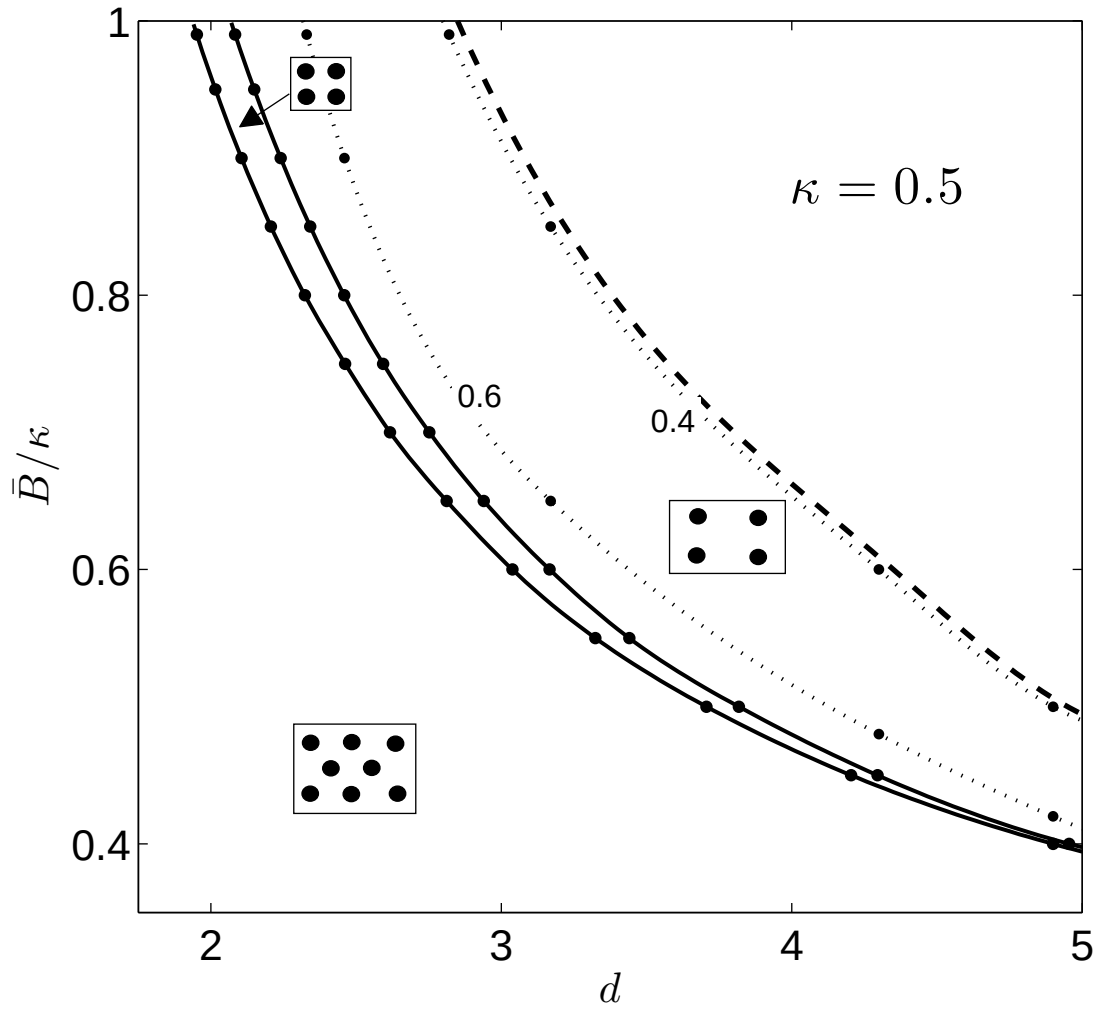

Figure 15: Vortex lattice phase diagram, $\kappa = 0.5$

The triangular-square transition is discontinuous while the square-rectangular transition is continuous. Inside the rectangular phase, the dotted lines labeled 0.6 and 0.4 are contours of constant aspect ratio. The dashed line corresponds to the aspect ratio of 0.38, which is the smallest aspect ratio for which a rectangular lattice is stable at the upper critical field ($\bar{B}/\kappa = 1$), following Callaway [28].

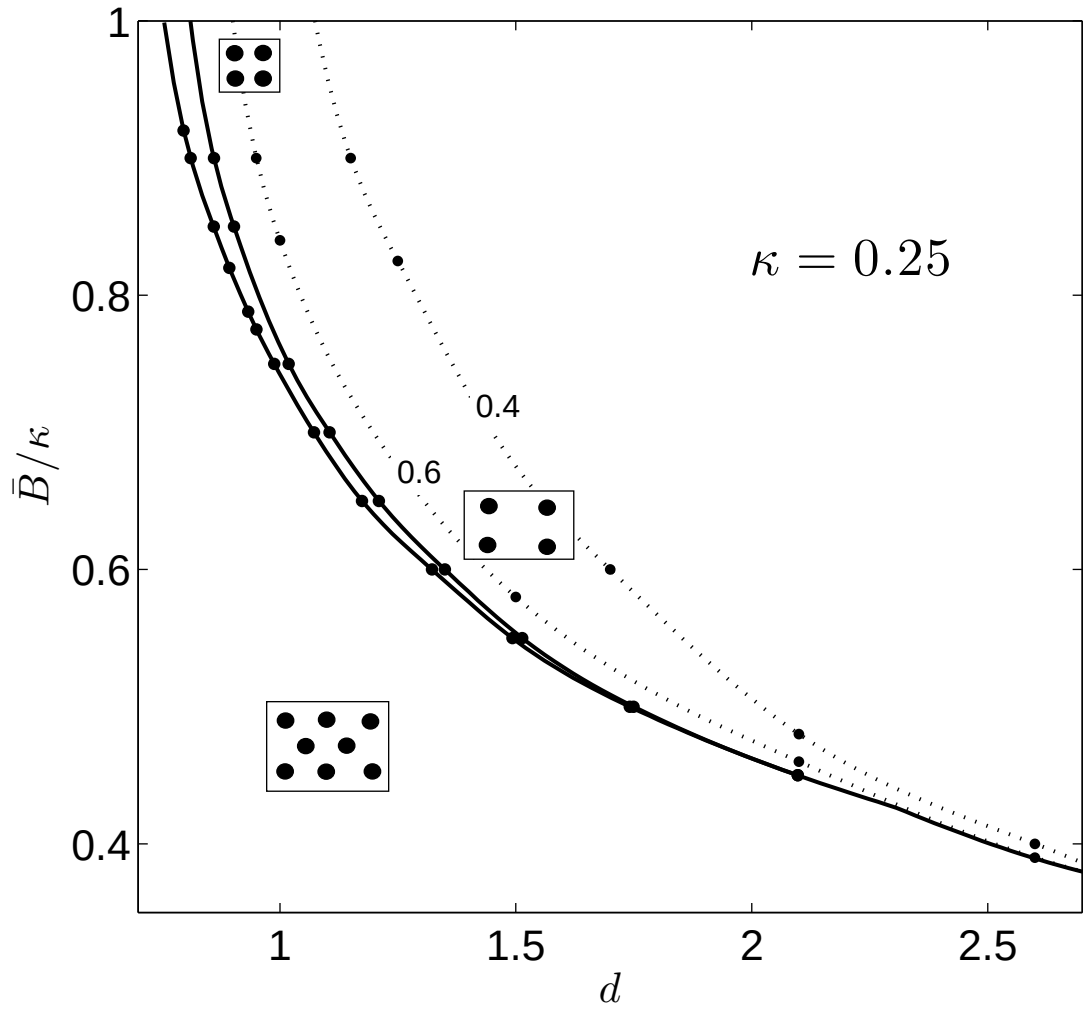

Figure 16: Vortex lattice phase diagram, $\kappa = 0.25$

Same as Fig. 15, but for $\kappa = 0.25$. Note the critical endpoint for the square-rectangular transition at $d \approx 2.1$.

Our results for double fluxoid vortex lattices are very limited compared to those for single fluxoid vortices and lattices of doubles do not appear in the phase diagrams in Figs. 15 and 16. In the portion of parameter space where states of one flux quantum per primitive cell are not the equilibrium flux configuration, there are many competing states, and those with one double fluxoid vortex per primitive cell form a small subset. In fact, Callaway's results[28] suggest that such states are never the global free energy minimal close to the upper critical field. Consequently there is no point in doing extensive calculations to arrive at a phase diagram for double fluxoid vortex lattices analogous to Fig. 15. What we can do, instead, is offer some support for the speculated phase boundary in Fig. 15 between the single fluxoid vortex lattice structures and flux structures with more than one flux quantum per primitive cell, by showing that the double-fluxoid vortex lattices have greater free energy in the region of parameter space we claim the single fluxoid lattices are stable.

In Figs. 17 and 18 present free energy densities referenced to the normal state as a function of film thickness for a $\kappa = 1/2$ superconductor at mean inductions which are 90% and 70%, respectively of the critical value. Triangular and square lattices of single and double fluxoid vortices are compared. (The minimum free energy rectangular lattices of single fluxoid vortices lie close enough to the square lattices for this purpose.) At 90% of the critical $\bar{B}$, the speculated boundary between rectangular vortex lattice and more complicated structures is at $d \approx 3.2$, while a double fluxoid structure does not yield a lower free energy than the single fluxoid square lattice until $d > 4.5$. At 70% of the critical $\bar{B}$, the corresponding values are $d \approx 4.0$ and $d > 4.5$. If that trend continues, it is possible that at sufficiently small $\bar{B}$ and large d the phase diagram Fig. 15 will require revision; however we have not been able to carry out the double fluxoid vortex lattice calculations at low enough mean induction to make a definite claim.

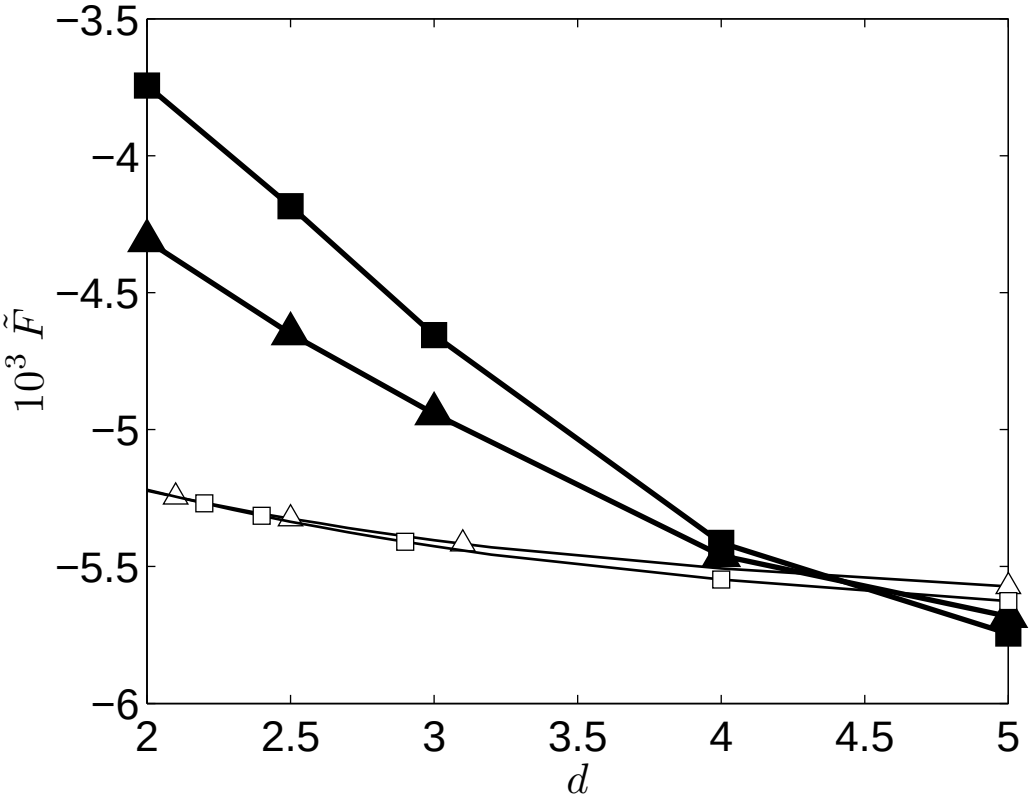

Figure 17: F vs. d, Singles and Doubles $b = 0.9$

Free energy densities of several vortex lattice structures as a function of film thickness at mean induction $\bar{B} = 0.9\mu_0 H_{c2}$ for $\kappa = 0.5$. Triangle symbols are for triangular lattices and square symbols are for square lattices; open symbols are for single-fluxoid vortices and solid symbols are for double-fluxoid vortices. Lines are guides to the eye.

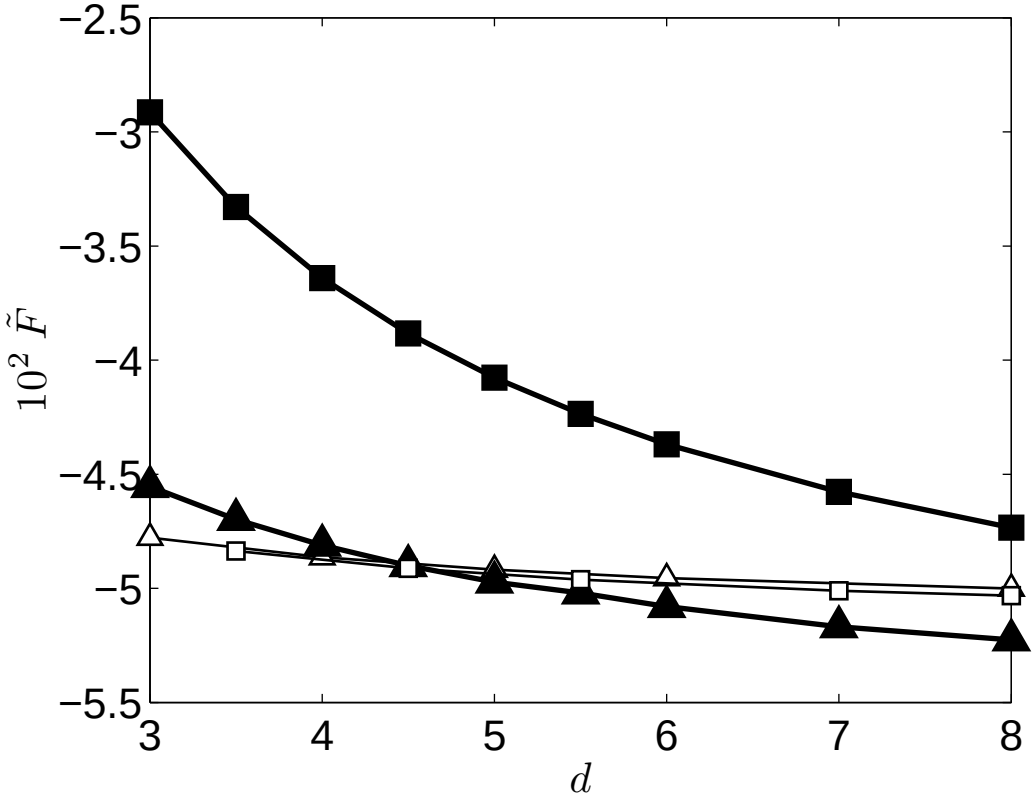

Figure 18: F vs. d, Singles and Doubles $b = 0.7$

Same as Fig. 17, but for mean induction $\bar{B} = 0.7\mu_0 H_{c2}$.

5.2.2 Free Energies

The lattices that do appear as the equilibrium state in our phase diagrams can be categorized by whether they have a rectangular or rhombohedral primitive unit cell. Recall that the primitive lattice vectors are $\mathbf{R}_{10} = x_1\hat{x}$ and $\mathbf{R}_{01} = x_2\hat{x} + y_2\hat{y}$ and for a fixed mean induction the unit cell area, $x_1 y_2$, is constant. We can then differentiate the two types by noting that rectangles have $x_2 = 0$ and rhombs have $x_2^2 + y_2^2 = x_1^2$. A square lattice is a special case that is both a rectangle and a rhomb, and the triangular lattice is a special case rhomb that has the largest nearest neighbor distance for a fixed unit cell area. With both types of lattices we can subcategorize them by the ratio y_2/x_1; squares have $y_2/x_1 = 1$ and triangles have $y_2/x_1 = \sqrt{3}/2$. In general we always assume the long side of the unit cell lies along x_1 (so $x_1 \geq x_2,\ y_2$). For rhombs y_2/x_1 is the sine of the angle between $\mathbf{R}_{10}$ and $\mathbf{R}_{01}$ but we will refer to this ratio as the aspect-ratio of the unit cell. A rectangular lattice that starts as a square and undergoes a sequence of pure shears will get wider and shorter with a decreasing aspect ratio and a decreasing nearest neighbor distance. A sequence of rhombs that start as a square lattice will also have decreasing aspect ratio but the nearest neighbor distance will rise to a maximum for the triangular lattice and then monotonically decrease.

It is of interest to look at the free energies that underlie the phase diagrams, to see the scale of the free energy differences. In the lower panel of Fig. 19, F is presented as a function of mean induction for $\kappa = 0.5$ and $d = 2.4$, while Fig. 20 does the same for $\kappa = 0.25$ and $d = 0.94$ (the latter thickness is chosen so that the phase transitions in the two figures are at roughly the same values of $\bar{B}/\kappa$). The rhombohedral lattice free energies, not shown in those figures, are nearly degenerate with the free energies of square and triangular lattices at the $\Delta \leftrightarrow \square$ phase transition, and close to the transition their free energies almost linearly interpolate between square and triangular lattice free energies.

Looking in more detail at the free energies underlying our $\kappa = 0.5$ phase diagram (Fig. 15) we focus on three different points where we have either a rectangle, square or triangle as the equilibrium lattice. In Fig. 21 we plot at $d = 2.5$ and $\bar{B}/\kappa = 0.99$ the mean free energy density as a function of aspect ratio. Here the rectangular lattice with $y_2/x_1 = 0.5$ is the lowest energy configuration, while the rhomb minimum is only slightly higher in free energy and lies at $y_2/x_1 = 0.46$. Also, the triangular lattice, with largest nearest neighbor distance, is a local maximum. From this point as we reduce $\bar{B}/\kappa$ or d the rectangle minimum shifts towards $y_2/x_1 = 1$, which we show in Fig. 22 at the point $d = 2.4$ and $\bar{B}/\kappa = 0.80$ where squares are the equilibrium lattice. The continuous change in aspect ratio is accompanied by a continuous change in free energy for the equilibrium rectangular lattices, i.e., these are a second-order phase changes. Moving from this second point on the phase diagram we examine the free energies at the point $d = 2.4$, $\bar{B}/\kappa = 0.70$ in the triangular phase shown in Fig. 23. Here the rectangular lattices have monotonically decreasing free energy as a function of aspect ratio but their minimum is still higher in energy than the triangular lattice. Near the square-triangle line the free energy differences between the two phases are extremely small. However, our data suggests that for rhombs in the range $\sqrt{3}/2 \leq y_2/x_1 \leq 1$ the free energy is either monotonically increasing or decreasing, and that squares and triangles are the only possible equilibrium rhombs.

5.2.3 Shear Moduli

Shear moduli have been evaluated for the three lattice structures which appear on the phase diagram; see the upper panels of Figs. 19 and 20. For triangular lattices the only shear modulus is $c_{66} = \frac{1}{2}(c_{11} - c_{12})$. For square lattices there are two distinct types of shear, with moduli c_{66} and $\frac{1}{2}(c_{11} - c_{12})$: the former preserves equality of primitive lattice vector length, while the latter preserves orthogonality of primitive lattice vectors. We present both on the figures because the latter vanishes at the

continuous square-rectangular transition and the former is anomalously small at the discontinuous triangular-square transition. For the rectangular lattices we considered only the shear mode which preserves orthogonality of primitive lattice vectors; the corresponding modulus is $\frac{1}{2}((c_{11} + c_{22})/2 - c_{12})$. In every case the shear modulus is calculated by evaluating the energy difference between the reference lattice structure and a slightly sheared lattice. One can see in the figures the small domains of metastability for the triangular and square lattice phases. It is also apparent that the vortex lattices at these values of κ and d are anomalously soft for a wide range of mean inductions. Details of how the moduli are defined and calculated are in Appendix D.

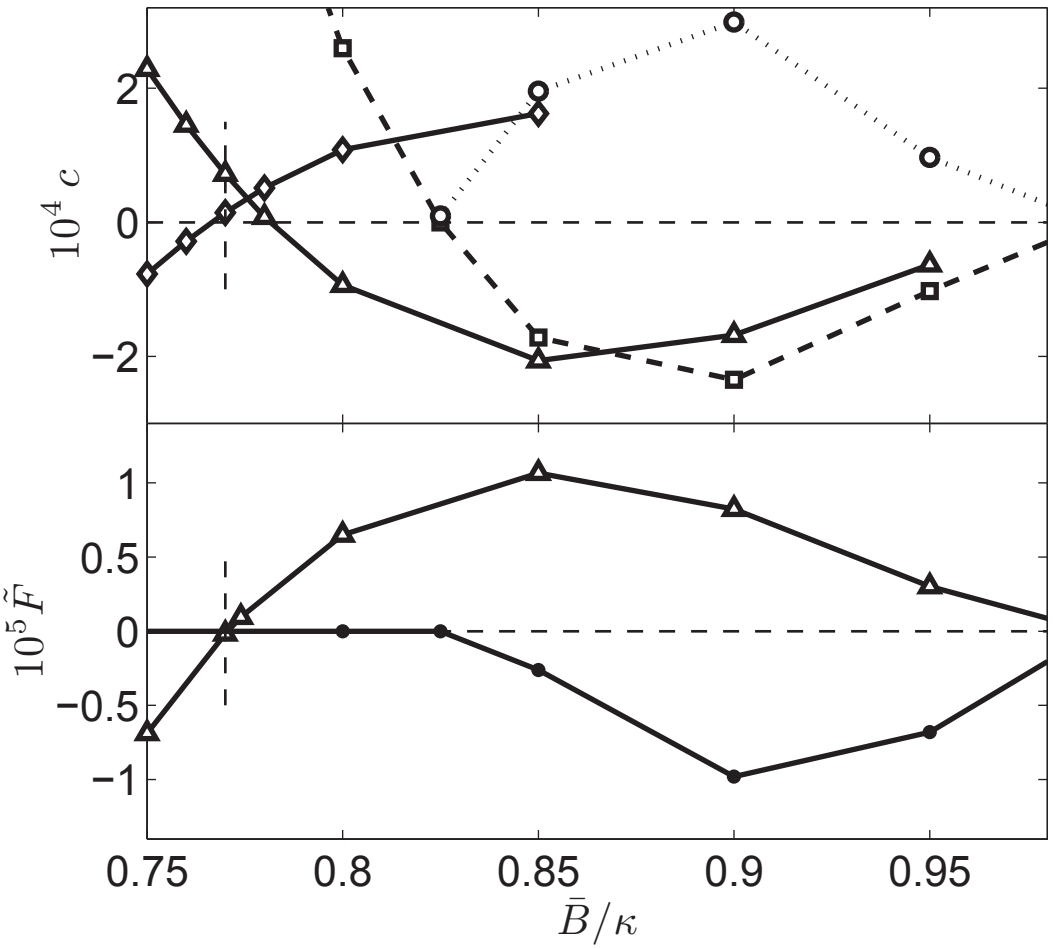

Figure 19: Shear moduli, $\kappa = 0.5$

Shear moduli and free energies per unit volume for triangular, square, and rectangular lattices, at $\kappa = 0.5$ and $d = 2.4$, for mean inductions around the domain of stability of the square lattice. Free energies are referenced to value for the square lattice; on that graph the triangular lattice values are the triangles and the minimum-F rectangular lattice values are the circles. The vertical dashed segments in both plots indicate the transition between triangular and square lattices, to make clear the discontinuity in shear modulus. On the shear modulus plot, triangles are c_{66} for the triangular lattice, diamonds are c_{66} for the square lattice, squares are $\frac{1}{2}(c_{11} - c_{12})$ for the square lattice, and circles are $\frac{1}{2}((c_{11} + c_{22})/2 - c_{12})$ for the minimum-F rectangular lattice. Both F and c are in units of $\mu_0 H_C^2$.

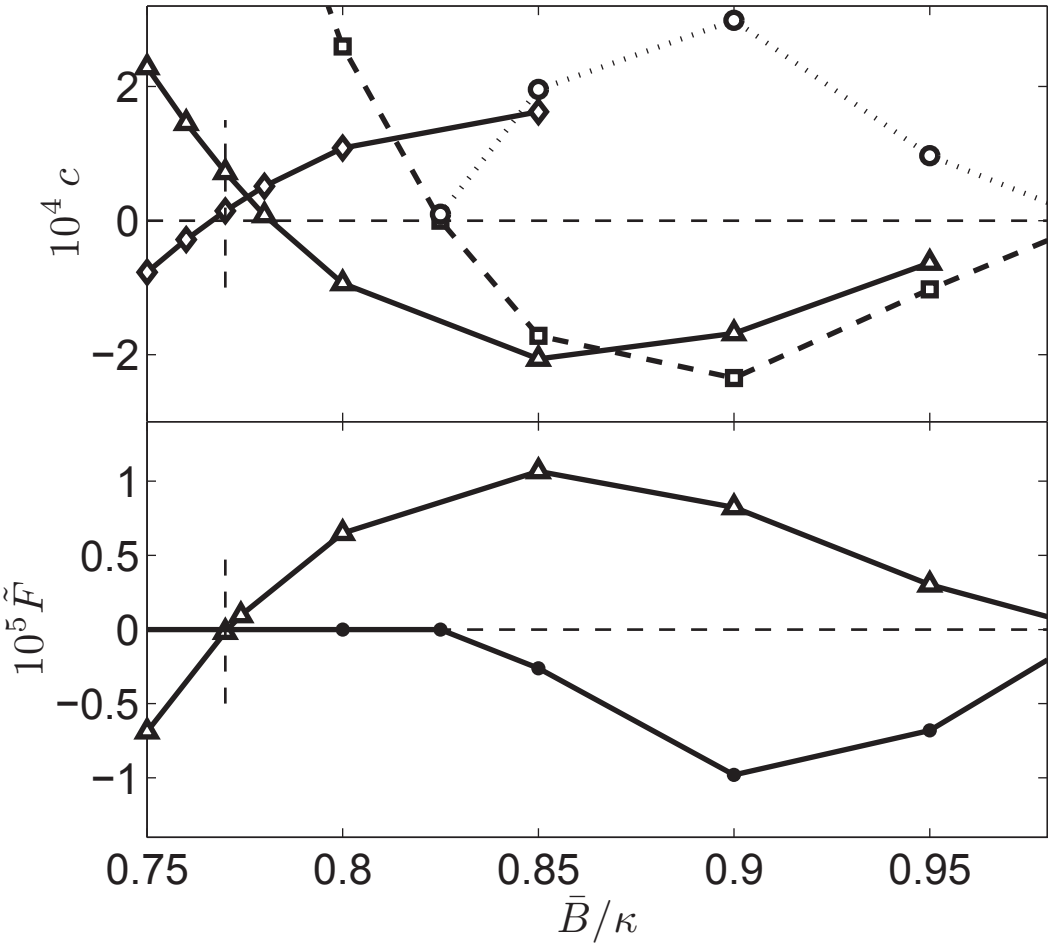

Figure 20: Shear moduli, $\kappa = 0.25$.

Same as Fig. 19, but for $\kappa = 0.25$ and $d = 0.94$.

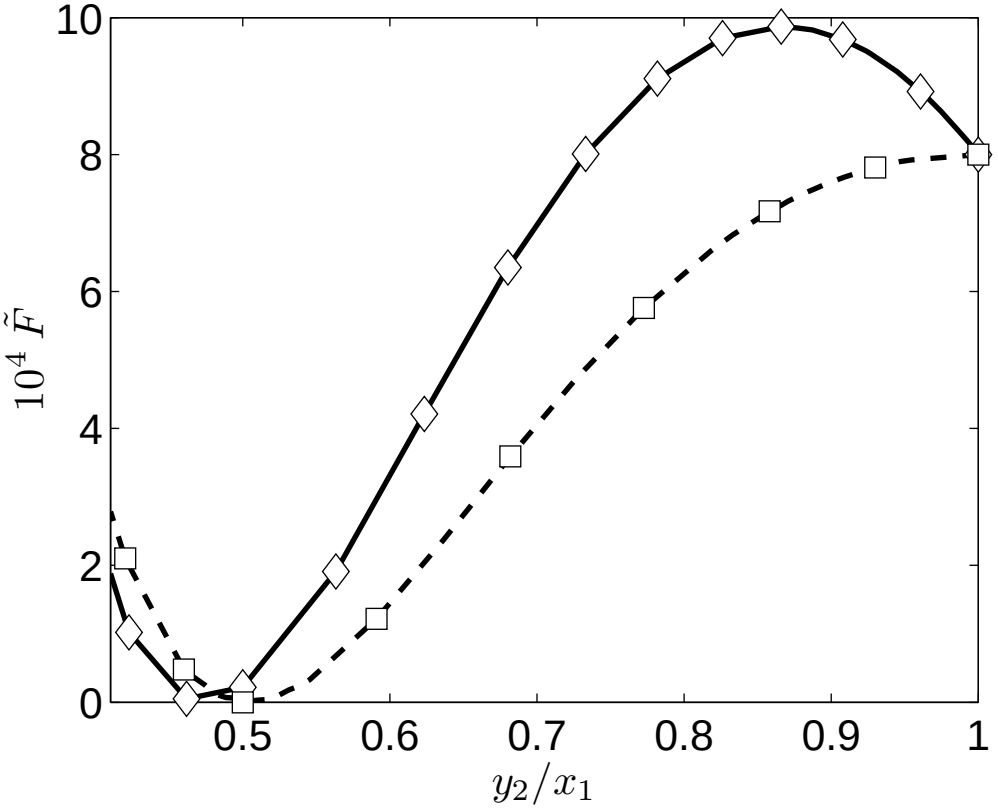

Figure 21: $\tilde{F}$ vs. y_2/x_1, $b = .99$

Free energy for $\kappa = 0.5$, $d = 2.5$, $\bar{B}/\kappa = 0.99$ (see phase diagram in Fig. 15) as a function of aspect ratio y_2/x_1 and referenced from the minimum. Sheared rhombs are plotted as solid lines with $\diamondsuit$, and rectangles are plotted as dashed lines with $\square$. The minimum $\tilde{F} = -5.46 \times 10^{-5}$ occurs for rectangles with $y_2/x_1 = 0.5$. Note that $y_2/x_1 = 0.866$ (the triangular lattice) is a local maximum.

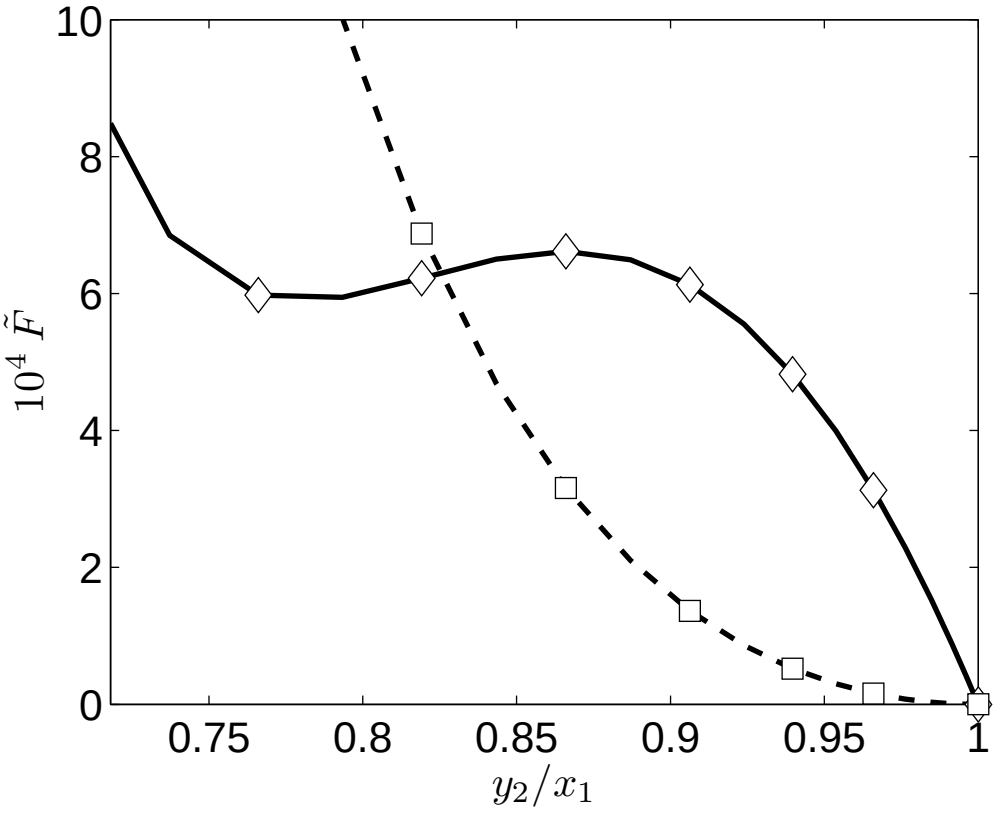

Figure 22: $\tilde{F}$ vs. y_2/x_1, $b = .80$

Same as Fig. 21 but for $\kappa = 0.5$, $d = 2.4$, $b = 0.80$. Minimum $\tilde{F} = -2.10 \times 10^{-2}$ occurs for the square lattice. Here, as in Fig. 21, the triangular lattice is a local maximum.

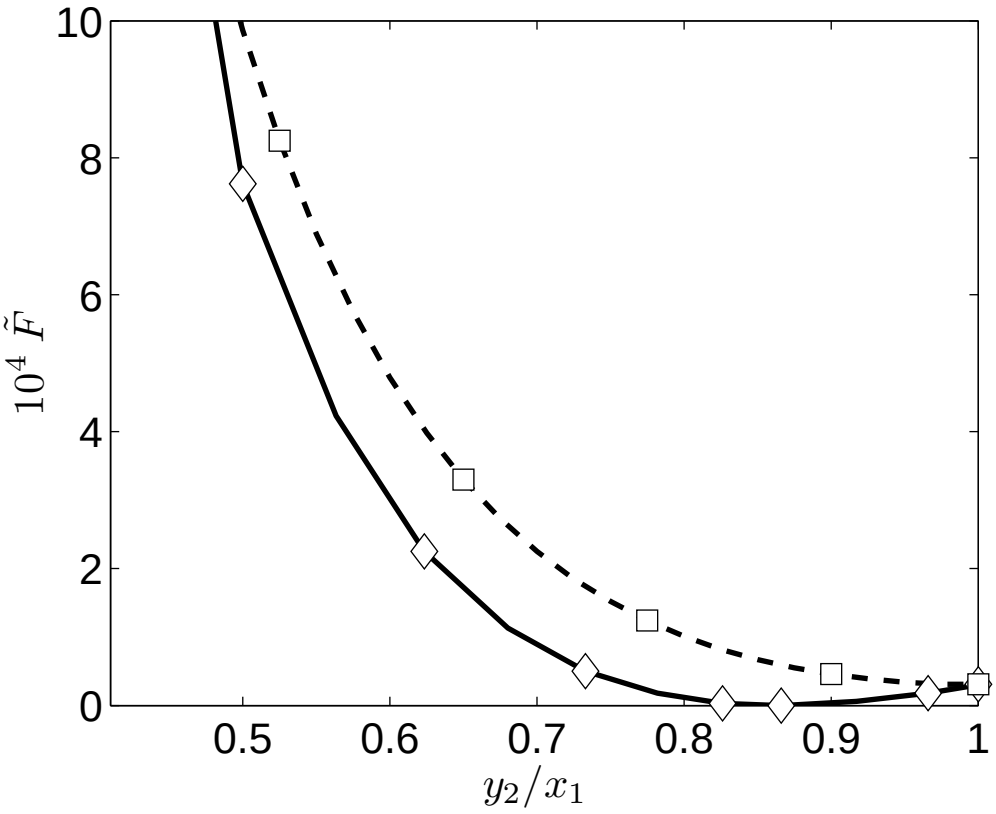

Figure 23: $\tilde{F}$ vs. y_2/x_1, $b = .70$

Same as Fig. 21 but for $\kappa = 0.5$, $d = 2.4$, $b = 0.70$. Minimum $\tilde{F} = -4.70 \times 10^{-2}$ occurs for the triangular lattice.

5.3 Free Energy Decompositions

The preceding section presented the main physical results of the calculations, but further insight might be gained by comparing not just F for different lattice structures but also various "components" of the free energy.

One decomposition is into the condensation, kinetic, and magnetic terms described following Eq. (71). Let us first consider $\kappa = 0.5$, $\bar{B}/\kappa = 0.825$, and $d = 2.0$, which is in the triangular phase but not far from the square phase. For a bulk system at the same GL parameter and mean induction, the square lattice has lower free energy density than the triangular lattice. Why is the relative stability reversed? In Table 2 on page 84 we present the differences in free energy density components between the film and the bulk system for both triangular and square vortex lattices. The signs of all those differences may be understood as a consequence of suppression of the order parameter in the film compared to the bulk. However, the exchange of stability is a more subtle matter, since that depends on the difference (triangular minus square lattice values) of those free energy density differences. Alternatively, we can compare the triangular and square lattice free energy density components for films of different thickness, as presented in Table 3 on page 84. It is then evident that with increasing thickness, the transition to the square vortex lattice is favored only by the condensation term.

We can also examine the z-dependence of the free energy density, integrating in Eq. (71) only over x and y and dividing only by S to define $F(z)$. (F_{stray} is taken as a z-independent contribution to $F(z)$.) Figure 24 on page 85 compares square and triangular vortex lattices for $\kappa = 0.5$ just below the upper critical field for $d = 1.5$, 2.0, and 2.5. The triangular lattice has lower total free energy only for $d = 1.5$. However, in every case $F(z)$ is lower for the triangular lattice when $z \approx d/2$, and, with decreasing z, $F(z)$ decreases more rapidly for the square lattice than for the triangular lattice. Figure 24 on page 85 is thus consistent with the interior of the

film being more bulk-like than the surface; and in fact $F(0)$ approaches F for a bulk system with as d increases. In terms of the free energy components, the condensation term is nearly independent of z, as is ω (as pointed out by Brandt for films of type-II superconductors [43]). The kinetic term is responsible for the z-dependence seen in Figure 24 on page 85, since the magnetic term is smaller at the surface, where the field lines spread out, than in the center of the film.

	$\triangle$	$\square$
$10^4\,\Delta F_{\text{cond}}$	161.	180.
$10^4\,\Delta F_{\text{kin}}$	-116.	-129.
$10^4(\Delta F_{\text{mag}} + \Delta F_{\text{stray}})$	-25.5	-29.0

Table 2: Film Minus Bulk Energy Terms

Film minus bulk energy terms for $\kappa = 0.5$, $\bar{B}/\kappa = 0.825$ and $d = 2.0$.

	$d = 2.0$	$d = 2.33$	$d = 2.6$
$10^4\,\Delta F_{\text{cond}}$	-4.44	-2.64	-1.37
$10^4\,\Delta F_{\text{kin}}$	6.55	5.29	4.42
$10^4(\Delta F_{\text{mag}} + \Delta F_{\text{stray}})$	-2.31	-2.60	-2.81

Table 3: F Δ vs. $\square$

Differences in free energy density terms (triangular lattice minus square lattice) at $\kappa = 0.5$ and $\bar{B}/\kappa = 0.825$ for several values of d. Note that $\Delta F < 0$ for $d = 2.0$ but is positive at the other thicknesses.

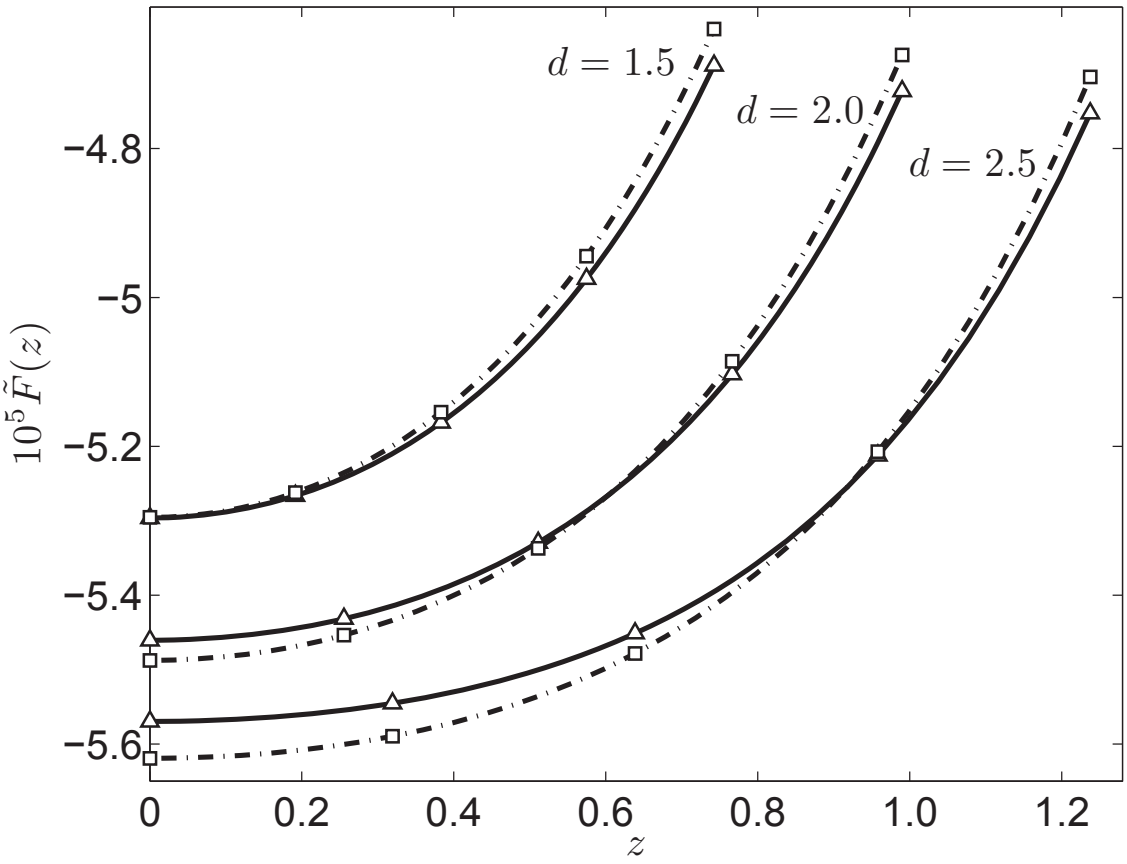

Figure 24: $\tilde{F}(z)$ for $\kappa = 0.5$

Free energy density dependence on z for films of various thickness with $\kappa = 0.5$ and $\bar{B} = 0.99/\kappa$, for square and triangular vortex lattices (indicated by the squares and triangles).

5.4 Low Induction Regime

The work of Hasegawa *et al.* [34] suggests for the film model we adopt that multiply quantized vortices may be found in the low induction regime. Our goal was to adapt the circular cell method for bulk samples, Sec. 4.6.1, to films in the same manner as we did for the flux line lattice. In this manner we hoped to explore the possibility of the stability of doubly quantized vortices in type-I films. We did develop complete Ansätze for singly and doubly quantized vortices, along with an iteration scheme much like the FLL for films described in Sec. 5.1. Our results for the film circular cell were successful with singly quantized vortices. However, our efforts for doubly quantized vortices yield convergent results that are not physically sensible. We have included the details for our work on the CC in films in Appendix K but at this point it is still an open problem.

5.5 Conclusions

We have improved Brandt's method [43] for solving the GL equations for thin-film superconductors in perpendicular magnetic fields, and applied it to a series of calculations for various vortex lattice structures with one vortex per primitive cell in type-I superconductor films of intermediate thickness ($d \sim \lambda$). The phase diagrams presented in Sec. 5.2 are the first step beyond the linearized theory towards the development of an accurate equilibrium flux structure phase diagram for films of type-I GL superconductors. The results suggest that non-triangular flux lattice structures (square and rectangular) may arise at mean inductions well below the upper critical value. For future work we wish to carry out similar calculations for flux structures with more that one vortex per primitive cell, as well as lattices of multiply-quantized vortices and various intermediate state models; these will require different expansions for the in-plane variation of ω, $\mathbf{q}$ and $\mathbf{b}$ but Legendre function expansions for the z dependence should still be applicable.

The anomalous softness of the vortex lattice in and near the domain of stability for the square vortex lattice offers hope that some features of the theoretical phase diagram might be observed in critical current measurements, in the form of a "peak effect" [45] well below the upper critical field. However, quantitative comparison between the theoretical phase diagrams and experimental results will necessarily be complicated by anisotropy and, possibly, thermal fluctuations [46].

A Units

A.1 CGS to SI

quantity	CGS	SI
B	1 Gauss (G)	10^{-4} Tesla (T)
H	1 Oersted	$10^3/4\pi$ A/m
M	1 emu/cm^3	10^3 A/m
Φ_0	$\frac{hc}{2e} = 2 \times 10^{-7}$ G $\cdot$ cm^2	$\frac{2\pi\hbar}{2e} = 2 \times 10^{-15}$ T $\cdot$ m^2
μ_0	1	$4\pi \times 10^{-7}$ N/A^2

Table 4: CGS to SI Units

Much of the classic literature uses CGS units, when using real units we use SI and this combined with the definitions for magnetic field and magnetic induction can lead to confusion.

A.2 Reduced Units

We use Abrikosov's [17] reduced units scheme, below are the conversions from SI units. The key constants are the penetration depth λ, the thermodynamic critical field H_c and the Meissner state order parameter $\psi_\infty = \sqrt{\frac{-\alpha}{\beta}}$ ($\alpha < 0$, see Sec. 2.6).

- Length: $\mathbf{r}' := \frac{1}{\lambda}\mathbf{r}$
- Derivatives: $\nabla' := \lambda\nabla$
- Magnetic Field: $\mathbf{H}' := \frac{1}{\sqrt{2}H_C}\mathbf{H}$
- Magnetic Induction: $\mathbf{B}' := \frac{1}{\mu_0\sqrt{2}H_C}\mathbf{B}$
- Vector Potential: $\mathbf{A}' := \frac{\lambda}{\mu_0\sqrt{2}H_C}\mathbf{A}$
- Current: $\mathbf{j}' := \frac{1}{\lambda\sqrt{2}H_C}\mathbf{j}$
- Free Energy Density: $F' := \frac{1}{\mu_0 H_C^2}F$
- Order Parameter: $\psi' := \psi/\psi_\infty$

The primes are dropped from equations used in this manuscript. In these units, one has:

- Coherence Length: $\xi \Rightarrow \frac{1}{\kappa}$
- Thermodynamic Critical Field: $H_C \Rightarrow \frac{1}{\sqrt{2}}$ for all values of κ
- Upper Critical Field: $H_{C2} \Rightarrow \kappa$
- "The" Condensation Energy: $\frac{1}{2}\mu_0 H_c^2 \Rightarrow \frac{1}{2}$
- Condensate Energy density: $\alpha\left|\psi\right|^2 + \frac{\beta}{2}\left|\psi\right|^4 \Rightarrow -\left|\psi\right|^2 + \frac{1}{2}\left|\psi\right|^4$ (for Meissner state this is $-\frac{1}{2}$)
- Kinetic Energy density: $\frac{1}{2m}\left|(-i\hbar\nabla - q\mathbf{A})\,\psi\right|^2 \Rightarrow \left|\left(-\frac{i}{\kappa}\nabla - \mathbf{A}\right)\psi\right|^2$

- Magnetic Field Energy density: $\frac{1}{2\mu_0}|\mathbf{B}|^2 \Rightarrow |\mathbf{B}|^2$
- Flux Quantum: $\Phi_0 \Rightarrow \frac{2\pi}{\kappa}$
- Gibbs Free Energy density: $G \Rightarrow F - 2H_a\bar{B}$ (see Sec. C)

	SI	Reduced units
κ	0.44	0.44
$\mu_0 H_c$	15.3 mT	$1/\sqrt{2}$
λ	110 nm	1
ξ	250 nm	2.27
$\mu_0 H_c^2$	186 J/m^3	1

Table 5: Values for Pb

In this work we present results for a type I superconductor with $\kappa = 0.5$. It is useful to use lead as an example of how our results will compare to real unit values. For this table we assume the temperature is ninety percent of T_c.

B Magnetic Fields

Even without superconductivity there is mixed usage in the terminology for the vector fields associated with magnetism: "magnetic field", "magnetic induction", "magnetic flux density", etc. We have tried to be consistent and call $\mathbf{B}$ the magnetic induction and $\mathbf{H}$ the magnetic field. While the mean dipole moment per unit volume in superconductors has a different source than in normal magnetic materials this quantity is still called the magnetization, $\mathbf{M}$. From this magnetization we then have the magnetic susceptibility tensor: $\chi_{ij} = \frac{\partial M_i}{\partial H_j}$. We also make some simplifying assumptions in our work: we have a static magnetic field and no electric field, $\frac{\partial \mathbf{H}}{\partial t} = 0$, $\frac{\partial \mathbf{E}}{\partial t} = 0$ and $\mathbf{E} = 0$. As usual the induction can be determined from a vector potential, $\mathbf{A}$, such that $\mathbf{B} = \nabla \times \mathbf{A}$ and from Maxwell's equations we have $\nabla \cdot \mathbf{B} = 0$. Also, we assume the superconducting materials, when in the normal state, are otherwise non-magnetic with permeability $\mu = \mu_0$. In this case the usually defined magnetic susceptibility is zero. However, there is a large diamagnetic response with superconductors and while there are no microscopic magnetic dipoles inside the sample we can thermodynamically define $\mathbf{M}$, $\mathbf{H}$ and χ for the superconducting state (see Eqs (118), (117) and (119) in Appendix C). Lastly, we consider a single current density $\mathbf{j}$ and do not separate that into free and bound currents. With these definitions and using the London gauge , $\nabla \cdot \mathbf{A} = 0$, we have the following equations in SI units:

$$\begin{aligned} \mathbf{B} &= \mu_0 \left(\mathbf{H} + \mathbf{M}\right) \\ \nabla \times \mathbf{B} &= \mu_0 \mathbf{j} \\ -\nabla^2 \mathbf{A} &= \mu_0 \mathbf{j} \end{aligned} \tag{98}$$

and in reduced units:

$$\begin{aligned} \mathbf{B} &= \mathbf{H} + \mathbf{M} \\ \nabla \times \mathbf{B} &= \mathbf{j} \\ -\nabla^2 \mathbf{A} &= \mathbf{j} \end{aligned} \tag{99}$$

These equations apply to the film and to the free space outside the sample where $\mathbf{M} = \mathbf{j} = 0$. Finally since much of the literature uses CGS units we include the same equations for CGS:

$$\begin{aligned} \mathbf{B} &= \mathbf{H} + 4\pi\mathbf{M} \\ \nabla \times \mathbf{B} &= \tfrac{4\pi}{c}\mathbf{j} \\ -\nabla^2 \mathbf{A} &= \tfrac{4\pi}{c}\mathbf{j} \end{aligned} \tag{100}$$

C Thermodynamics

The superconducting state is determined by temperature and magnetic field and does not depend on the magnetic history of the sample (in the absence of defects or impurities). Therefore it is correct to call it a thermodynamic state. Ginzburg-Landau theory is based on a free energy density expanded in powers of an order parameter. This free energy is a function of temperature and magnetic induction $\mathbf{B}$. In determining the equilibrium phase of the mixed state in film and bulk superconductors it is more useful to have a the free energy as a function of the externally applied magnetic field $\mathbf{H}_a$. There are many versions of free energy used in the literature with a variety of notations. This section is intended as a coherent summary of the thermodynamics of superconductors for the configurations we consider (based on Landau, Pittaevskii and Lifshitz [12]) and with clear definitions of the thermodynamic variables and quantities of interest. A note on the particulars of the systems we work with: we treat the sample macroscopically and with fields parallel to the z-axis: mean induction $\bar{\mathbf{B}} = \bar{B}\hat{z}$, external applied field $\mathbf{H}_a = H_a\hat{z}$ and magnetization $\mathbf{M} = M\hat{z}$. The magnetic susceptibility is then a simple scalar: $\chi = \frac{\partial M}{\partial H_a}$.

C.1 Thermodynamic Potentials

In GL theory we start from free energy $\mathcal{F} = \mathcal{F}\left(T, \bar{\mathbf{B}}\right)$, but in order to be able to make comparisons to experiment it is more useful if we have an energy as a function of the applied field, $\mathbf{H}_a$. That is, we would like to get the Gibbs free energy $\mathcal{G} = \mathcal{G}\left(T, \mathbf{H}_a\right)$ where $\bar{\mathbf{B}}$ and $\mathbf{H}_a$ are conjugate thermodynamic variables. We can write these energies

as volume integrals of free energy densities F and G:

$$\mathcal{F} = \int F\left(\mathbf{r}, T, \bar{\mathbf{B}}\right) d^3r \qquad \mathcal{G} = \int G\left(\mathbf{r}, T, \mathbf{H}_a\right) d^3r$$

Where $F\left(\mathbf{r}, T, \bar{\mathbf{B}}\right)$ is the GL free energy functional. We will be working with structures that are periodic with unit cell volume V so we can work with mean densities:

$$\bar{F}\left(T, \bar{\mathbf{B}}\right) = \frac{1}{V}\int_V F\left(\mathbf{r}, T, \bar{\mathbf{B}}\right) d^3r \qquad \bar{G}\left(T, \mathbf{H}_a\right) = \frac{1}{V}\int_V G\left(\mathbf{r}, T, \mathbf{H}_a\right) d^3r$$

The thermodynamic state of the system can then be determined from these mean free energy densities.

Now, we would like to establish how we can get the Gibbs energy from $\bar{F}$. In addition, we will define two new thermodynamic potentials and determine how we can get quantities like H_a, M, etc. from these potentials. First, we assume a constant pressure and volume (i.e., no $p\,dV$ work) and with entropy density s we have

$$d\bar{F} = -s dT + \mathbf{H}_a \cdot d\bar{\mathbf{B}}\,. \tag{101}$$

Then we can define the Gibbs energy density by a Legendre transformation

$$\bar{G}\left(T, \mathbf{H}_a\right) \equiv \bar{F}\left(T, \bar{\mathbf{B}}\right) - \mathbf{H}_a \cdot \bar{\mathbf{B}}\,, \tag{102}$$

which gives us

$$d\bar{G} = -s dT - \bar{\mathbf{B}} \cdot d\mathbf{H}_a \tag{103}$$

and we note that in the Meissner state

$$\bar{G}\left(T, \mathbf{H}_a\right)_{\bar{B}=0} = \bar{F}\left(T, 0\right)\,. \tag{104}$$

We assume the sample is non-magnetic so in the normal state the energy comes solely from the magnetic field energy. Also, in the normal state $\bar{\mathbf{B}} = \mu_0 \mathbf{H}_a$ and $\mathbf{H}_a \cdot \bar{\mathbf{B}} = \frac{1}{\mu_0}\bar{B}^2 = \mu_0 H_a^2$. So the normal state free energies are

$$\bar{F}_N\left(T, \bar{\mathbf{B}}\right) = \frac{1}{2\mu_0}\bar{B}^2\,, \tag{105}$$

$$\bar{G}_N\left(T, \mathbf{H}_a\right) = -\frac{1}{2}\mu_0 H_a^2 \tag{106}$$

and Eq. (104) also applies (in this case $\bar{B} = 0$ requires that $H_a = 0$) and

$$\bar{G}_N\left(T, \mathbf{H}_a = 0\right) = \bar{F}_N\left(T, \bar{\mathbf{B}} = 0\right)\,. \tag{107}$$

The free energy difference in zero field between the normal state and the Meissner state is what defines the thermodynamic critical field for type-II superconductors,

$$\bar{F}_N\left(T, 0\right) - \bar{F}\left(T, 0\right) = \frac{1}{2}\mu_0 H_c^2\,. \tag{108}$$

Also, for the Gibbs energy from Eqs. (104) and (107) we find that

$$\bar{G}_N\left(T, 0\right) - \bar{G}\left(T, \mathbf{H}_a\right)_{\bar{B}=0} = \frac{1}{2}\mu_0 H_c^2\,. \tag{109}$$

The free energy $\bar{F}$, by our definition in Eq. (101), includes the field energy $\bar{F}_N\left(T, \bar{\mathbf{B}}\right)$. This field energy is present whether our sample is there or not. We would like to redefine what is our thermodynamic system and exclude the normal state field energy. This leads us to new free energy definitions

$$\tilde{F}\left(T, \bar{\mathbf{B}}\right) \equiv \bar{F}\left(T, \bar{\mathbf{B}}\right) - \bar{F}_N\left(T, \bar{\mathbf{B}}\right) \tag{110}$$

and

$$\tilde{G}\left(T,\mathbf{H}_a\right) \equiv \bar{G}\left(T,\mathbf{H}_a\right) - \bar{G}_N\left(T,\mathbf{H}_a\right) . \tag{111}$$

We can then get the differential form of these energies:

$$\begin{aligned} d\tilde{F} &= d\bar{F} - \frac{1}{\mu_0}\bar{\mathbf{B}}\cdot d\bar{\mathbf{B}} \qquad & d\tilde{G} &= d\bar{G} + \mu_0\mathbf{H}_a\cdot d\mathbf{H}_a \\ d\tilde{F} &= dF - (\mathbf{H}_a+\mathbf{M})\cdot d\bar{\mathbf{B}} \qquad & d\tilde{G} &= -sdT - \bar{\mathbf{B}}\cdot d\mathbf{H}_a + \mu_0\mathbf{H}_a\cdot d\mathbf{H}_a \end{aligned}$$

$$d\tilde{F} = -sdT - \mathbf{M}\cdot d\bar{\mathbf{B}} \tag{112}$$

$$d\tilde{G} = -sdT - \mu_0\mathbf{M}\cdot d\mathbf{H}_a \tag{113}$$

We started from the free energy density $F\left(\mathbf{r},T,\bar{\mathbf{B}}\right)$ and then derived several relationships and defined some new quantities. To be clear F is the Ginzburg-Landau free energy density from Eq. (6) and we repeat the definition

$$F\left(\mathbf{r},T,\bar{\mathbf{B}}\right) = \alpha\left|\psi\right|^2 + \frac{\beta}{2}\left|\psi\right|^4 + \frac{1}{2m}\left|\left(-i\hbar\nabla - q\mathbf{A}\right)\psi\right|^2 + \frac{1}{2\mu_0}\left|\mathbf{B}\right|^2 . \tag{114}$$

Our $\tilde{F}\left(T,\bar{\mathbf{B}}\right)$ is a mean free energy density and we define a local version

$$\tilde{F}\left(\mathbf{r},T,\bar{\mathbf{B}}\right) = \alpha\left|\psi\right|^2 + \frac{\beta}{2}\left|\psi\right|^4 + \frac{1}{2m}\left|\left(-i\hbar\nabla - q\mathbf{A}\right)\psi\right|^2 + \frac{1}{2\mu_0}\left|\mathbf{b}\right|^2 \tag{115}$$

where $\mathbf{b}\left(\mathbf{r}\right) = \mathbf{B}\left(\mathbf{r}\right) - \bar{\mathbf{B}}$.

From the definitions for $\tilde{F}\left(T,\bar{\mathbf{B}}\right)$ and $\tilde{G}\left(T,\mathbf{H}_a\right)$ (Eq. (110) and Eq. (111)) and from Eq. (115) it is clear that the normal state will have a zero energy for any value of $\bar{\mathbf{B}}$ or $\mathbf{H}_a$. For this reason we sometimes refer to these energies, $\tilde{F}$ and $\tilde{G}$, as referenced from the normal state. In the Meissner state we have $\bar{G}\left(T,\mathbf{H}_a\right)_{\bar{B}=0} = \bar{F}\left(T,0\right) = -\frac{1}{2}\mu_0 H_c^2$ for any value of $\mathbf{H}_a$. We say that F and G are referenced from the Meissner state. More fundamentally, the difference between $\left[\bar{F},\bar{G}\right]$ and $\left[\tilde{F},\tilde{G}\right]$ comes from a change in the definition of the thermodynamic system. $\bar{F}\left(T,\bar{\mathbf{B}}\right)$ includes the

energy of the superconductor's diamagnetic response and the energy in creating the magnetic field, $\tilde{F}\left(T,\bar{\mathbf{B}}\right)$ only includes the energy of the diamagnetic response.

In GL theory we start from an assumed mean induction and then find a minimum for the functional $\bar{F}\left(T,\bar{\mathbf{B}}\right)=\frac{1}{V}\int_V F\left(\mathbf{r},T,\bar{\mathbf{B}}\right)\,d^3r$. Then to get $\bar{G}\left(T,\mathbf{H}_a\right)=\bar{F}\left(T,\bar{\mathbf{B}}\right)-\mathbf{H}_a\cdot\bar{\mathbf{B}}$ we need to know the applied field $\mathbf{H}_a$. Rather than calculate the derivative $\frac{\partial\bar{F}}{\partial\bar{B}}$ numerically, in practice it is easier for us to calculate $\mathbf{H}_a$ via the virial theorem method of Klein and Pöttinger [24] where

$$\mathbf{H}_a\cdot\bar{\mathbf{B}}=\frac{1}{V}\int_V \alpha\left|\psi\right|^2+\beta\left|\psi\right|^4+\frac{1}{2m}\left|\left(-i\hbar\nabla-q\mathbf{A}\right)\psi\right|^2+\frac{1}{2\mu_0}\left|\mathbf{B}\right|^2\,d^3r\,. \tag{116}$$

In our work the macroscopic fields are all aligned with the z-axis. so we can divide the integral by the mean induction to get H_a. We have confirmed that, from solutions to our iteration scheme, this does match the result from the thermodynamic relation

$$\left(\frac{\partial\bar{F}}{\partial\bar{B}}\right)_T=H_a\,. \tag{117}$$

Finally, to get the magnetization and susceptibility from the thermodynamic relations:

$$-\left(\frac{\partial\tilde{F}}{\partial\bar{B}}\right)_T=-\frac{1}{\mu_0}\left(\frac{\partial\tilde{G}}{\partial H_a}\right)_T=M \tag{118}$$

$$-\frac{1}{\mu_0}\left(\frac{\partial^2\tilde{G}}{\partial H_a^2}\right)_T=\chi \tag{119}$$

and in reduced units:

$$\frac{1}{2}\left(\frac{\partial\bar{F}}{\partial\bar{B}}\right)_T=H_a \tag{120}$$

$$-\frac{1}{2}\left(\frac{\partial\tilde{F}}{\partial\bar{B}}\right)_T=-\frac{1}{2}\left(\frac{\partial\tilde{G}}{\partial H_a}\right)_T=M \tag{121}$$

$$-\frac{1}{2}\left(\frac{\partial^2 \tilde{G}}{\partial H_a^2}\right)_T = \chi \tag{122}$$

C.2 Magnetization Work

We wish to calculate the work done (at constant temperature) in magnetizing a superconducting sample from the Meissner state in zero applied field to the normal state. We integrate Eq. (113) from $H_a = 0$ to $H_a = H_{c2}$:

$$-\mu_0 \int_0^{H_{c2}} M\left(H_a\right)\, dH_a = \tilde{G}\left(H_{c2}\right) - \tilde{G}\left(0\right)$$

At H_{c2} the mixed state is in equilibrium with the normal state and $\tilde{G}\left(H_{c2}\right) = \tilde{G}_N\left(H_{c2}\right)$. By definition $\tilde{G}_N\left(H_a\right) = 0$. At the lower limit we have $\tilde{G}\left(0\right) = \bar{G}\left(0\right) - \bar{G}_N\left(0\right)$ from the definition of $\tilde{G}$ in Eq. (111). While Eq. (109) tells us that $\bar{G}\left(0\right) - \bar{G}_N\left(0\right) = -\frac{1}{2}\mu_0 H_c^2$.

$$-\mu_0 \int_0^{H_{c2}} M\left(H_a\right)\, dH_a = 0 - \left[-\frac{1}{2}\mu_0 H_c^2\right]$$

$$-\mu_0 \int_0^{H_{c2}} M\left(H_a\right)\, dH_a = \frac{1}{2}\mu_0 H_c^2 \tag{123}$$

This gives us the result that the area under the magnetization curve is equal to the condensation energy. This will be of practical value in our work as a validity check on our results. In reduced units we have:

$$-\int_0^{H_{c2}} M\left(H_a\right)\, dH_a = \frac{1}{2} \tag{124}$$

D Elasticity Theory

In comparing stability of different lattice types it is useful to compare various shear moduli. To be clear, we are talking about shear, stresses and strains in the flux line lattice not the crystal lattice. In this section we present background in linear elastic theory and follows Landau and Lifshitz [47]. We consider a deformation inside a body which changes a position from $\mathbf{r}$ to $\mathbf{r}'$ ($r_1 = x$, $r_2 = y$ and $r_3 = z$) and define the displacement $\mathbf{u} = \mathbf{r}' - \mathbf{r}$. For small deformations the strain tensor is defined as $u_{ij} = \frac{1}{2}\left(\frac{\partial u_i}{\partial r_j} + \frac{\partial u_j}{\partial r_i}\right)$ and is dimensionless. The total force on the body can be written as a volume integral over a force density, $\mathbf{F} = \int \mathbf{f}\, dV$. Then the force density can be written as the divergence of a rank 2 tensor, $f_i = \frac{\partial \sigma_{ij}}{\partial r_j}$ where σ_{ij} is the strain tensor with units force/area (or energy/volume). There is an implied summation when using subscripts. For small deformations in a solid body Hooke's Law is

$$\sigma_{ij} = C_{ijkl} u_{kl} \,. \tag{125}$$

Both the strain and stress are symmetric rank two tensors with six independent components each and C_{ijkl} is the elasticity tensor with units force/area. The elasticity tensor is a rank four tensor with 81 components but symmetry requirements for the stress and strain tensor reduces the number of terms to 36 and requirements on the associated strain energy reduces the number of independent terms in C_{ijkl} to 21.The full $6x6$ matrix representation of Hooke's Law can be found in many texts (e.g. [48]) but in our two dimensional vortex lattices require only a $3x3$ matrix. We ignore any

tilting of the flux lines along the z-direction. So Hooke's law becomes:

$$\begin{bmatrix} \sigma_{xx} \\ \sigma_{yy} \\ \sigma_{xy} \end{bmatrix} = \begin{bmatrix} C_{11} & C_{12} & C_{16} \\ C_{12} & C_{22} & C_{26} \\ C_{16} & C_{26} & C_{66} \end{bmatrix} \begin{bmatrix} u_{xx} \\ u_{yy} \\ 2u_{xy} \end{bmatrix}. \tag{126}$$

The stress and strain, as second-order tensors, must transform as $\sigma'_{ij} = Q_{ik}Q_{jl}\sigma_{kl}$ and $u'_{ij} = Q_{ik}Q_{jl}u_{kl}$, where Q_{ij} is an orthogonal tensor with $Q_{il}Q_{jl} = \delta_{ij}$. In this work we are primarily interested in three lattices: triangular, square and rectangular. These lattices have symmetries and corresponding requirements on the transformation tensors, Q_{ij}, that further reduce the number of elastic moduli. In all three lattices of interest $C_{16} = C_{26} = 0$. Both triangular and square lattices have $C_{22} = C_{11}$. Finally, we are concerned with constant volume deformation, that is pure shears, where the strain tensor is trace-less and $u_{yy} = -u_{xx}$.

For triangular lattices $C_{66} = (C_{11} - C_{12})/2$

$$\begin{bmatrix} \sigma_{xx} \\ \sigma_{yy} \\ \sigma_{xy} \end{bmatrix} = C_{66} \begin{bmatrix} 2 & 0 \\ -2 & 0 \\ 0 & 1 \end{bmatrix} \begin{bmatrix} u_{xx} \\ 2u_{xy} \end{bmatrix} \tag{127}$$

square lattices

$$\begin{bmatrix} \sigma_{xx} \\ \sigma_{yy} \\ \sigma_{xy} \end{bmatrix} = \begin{bmatrix} (C_{11} - C_{12}) & 0 \\ -(C_{11} - C_{12}) & 0 \\ 0 & C_{66} \end{bmatrix} \begin{bmatrix} u_{xx} \\ 2u_{xy} \end{bmatrix} \tag{128}$$

and rectangular lattices

$$\begin{bmatrix} \sigma_{xx} \\ \sigma_{yy} \\ \sigma_{xy} \end{bmatrix} = \begin{bmatrix} (C_{11} - C_{12}) & 0 \\ -(C_{22} - C_{12}) & 0 \\ 0 & C_{66} \end{bmatrix} \begin{bmatrix} u_{xx} \\ 2u_{xy} \end{bmatrix}. \tag{129}$$

D.1 Thermodynamics

Work is done when deforming a solid body this leads to an energy change, called the strain energy, $\Delta F_{strain} \equiv \frac{1}{2}\sigma_{ij}u_{kl}$. Then for Helmholtz free energy density F, and Gibbs free energy density G:

$$\left(\frac{\partial F}{\partial u_{ij}}\right)_{T,\bar{B}} = \sigma_{ij} \tag{130}$$

$$\left(\frac{\partial G}{\partial \sigma_{ij}}\right)_{T,H} = -u_{ij}\,. \tag{131}$$

In the elastic regime we have the Hooke's Law relationship $\sigma_{ij} = \frac{1}{2}C_{ijkl}u_{ij}$ and $\Delta F_{strain} = \frac{1}{2}C_{ijkl}u_{ij}u_{kl}$. Our interests are in how stiff or soft the vortex lattice is for small deformations.

The strain energies for the lattices of interest are:

$$\Delta F_{strain}^{(TRI)} = 2C_{66}u_{xy}^2 \tag{132}$$

$$\Delta F_{strain}^{(SQ)} = \left(C_{11} - C_{12}\right)u_{xx}^2 + 2C_{66}u_{xy}^2 \tag{133}$$

$$\Delta F_{strain}^{(RECT)} = \left[\frac{1}{2}\left(C_{11} + C_{22}\right) - C_{12}\right]u_{xx}^2 + 2C_{66}u_{xy}^2 \tag{134}$$

D.2 Calculating Shear Moduli

A lattice unit cell is defined by the vectors $\mathbf{R}_{10} = x_1\hat{x}$ and $\mathbf{R}_{01} = x_2\hat{x} + y_2\hat{y}$ and has area $S = |\mathbf{R}_{10} \times \mathbf{R}_{01}| = x_1y_2$. A simple shear that takes the lattice to $\mathbf{R}'_{01} = \left(x_2 \pm \delta y_2\right)\hat{x} + y_2\hat{y}$ (these are small deformations: $\delta \ll 1$) can be used to calculate C_{66} ($\mathbf{R}'_{10} = \mathbf{R}_{10}$). In this case $\mathbf{u} = \pm\delta y\hat{x}$, $u_{xx} = u_{yy} = 0$, $u_{xy} = \pm\frac{1}{2}\delta$ and $C_{66} = \frac{1}{\delta^2}\Delta F_{strain}$.

All rectangular unit cells have $x_2 = 0$ and a rectangle to rectangle pure shear has $\mathbf{R}'_{10} = x_1\left(1+\delta\right)\hat{x}$ and $\mathbf{R}'_{01} = y_2\left(\frac{1}{1+\delta}\right)\hat{y}$. Again we have $\delta \ll 1$ so $\mathbf{R}'_{01} \approx y_2\left(1-\delta\right)\hat{y}$. For this case $\mathbf{u} = \delta x\hat{x} - \delta y\hat{y}$, $u_{xx} = \delta$, $u_{yy} = -\delta$, $u_{xy} = 0$. Squares are a special case of rectangles with $y_2 = x_1$. We attempt to compare shear moduli for the lattices on

an equal footing and with the triangular case having $C_{66} = (C_{11} - C_{12})/2$, we define $C_{SQ} = (C_{11} - C_{12})/2$ and $C_{RECT} = \frac{1}{4}(C_{11} + C_{22}) - \frac{1}{2}C_{12}$. Then $C_{SQ} = \frac{1}{2\delta^2}\Delta F_{strain}^{(SQ)}$ and $C_{RECT} = \frac{1}{2\delta^2}\Delta F_{strain}^{(RECT)}$.

In order to calculate the moduli we first run our iteration scheme, with fixed κ and $\bar{B}$, to convergence for lattices defined by $[\mathbf{R}_{10},\mathbf{R}_{01}]$ and $[\mathbf{R}'_{10},\mathbf{R}'_{01}]$. These results yield the strain energy: $\Delta F_{strain} = F' - F$.

E Small $r_\perp$ Behavior for ψ

We reproduce a derivation due to Tinkham [10] Sec. 5.1. We start by assuming for a p-quanta vortex the order parameter has the form $\psi = cr_\perp^n e^{ip\theta}$, $n > 0$ for small values of $r_\perp$. In this region all fields are radially symmetric and we have $\mathbf{A} = A(r_\perp)\hat{\theta}$ and $B_z = \frac{1}{r_\perp}\frac{\partial}{\partial r_\perp}(r_\perp A)$

$$A(r_\perp) = \frac{1}{r_\perp}\int_0^{r_\perp} r' B_z(r')\, dr' \tag{135}$$

Near the core, this becomes

$$A(r_\perp) = \frac{1}{2}B_z(0)\, r_\perp \tag{136}$$

and the supervelocity (see Sec. 3.3) is:

$$Q(r_\perp) = \frac{1}{2}B_z(0)\, r_\perp - \frac{p}{\kappa r_\perp} \tag{137}$$

Applying the first GL Equation Eq. (12):

$$\frac{1}{\kappa^2}n^2 r_\perp^{n-2} = cr^n\left(\frac{1}{2}B_z(0)\, r_\perp - \frac{p}{\kappa r_\perp}\right)^2 - cr_\perp^n + cr_\perp^{3n} \tag{138}$$

Grouping like powers:

$$\frac{1}{\kappa^2}\left[p^2 - n^2\right] r_\perp^{n-2} - \left(1 + B_z(0)\frac{p}{\kappa}\right) r_\perp^n + \frac{1}{4}B_z^2(0)\, r_\perp^{n+2} + r_\perp^{3n} = 0 \tag{139}$$

As $r \to 0$, this is dominated by the first term. For this to vanish $p = n$ and we conclude that for a p-quanta vortex that $\psi(r_\perp) = cr_\perp^p e^{ip\theta}$

F Linearized GL Equation

In this section we derive necessary relationships for our method in Appendix H for finding ω_A for doubly quantized vortices. The full treatment for the linearized Ginzburg-Landau equation can be found in Abrikosov [17]. Our version is intended to generalize some of Abrikosov's findings for the p-quanta vortex. We don't rederive one of these results but assume *a priori*

$$H_{c2} = \sqrt{2}\kappa H_c \tag{140}$$

where in reduced units we have $H_c = \frac{1}{\sqrt{2}}$ and $H_{c2} = \kappa$.

In high induction regimes, $H_{c2} - H_a \ll 1$, where the superconducting state is just beginning to nucleate the order parameter will be small and the first GL equation simplifies to

$$\left(-\frac{i}{\kappa}\nabla - \mathbf{A}\right)^2 \psi_A = \psi_A \tag{141}$$

We use the subscript "A" to indicate these fields are for the linearized GL equation (often the solution here is referred to as the Abrikosov solution). This equation is equivalent to Schrödinger's equation for a charged particle in a magnetic field. In this limiting case the induction in the sample will be nearly uniform, $\nabla \times \mathbf{A} = \kappa\hat{z}$ ($H_{c2} = \kappa$ in reduced units) and we can choose a gauge so $\mathbf{A} = \frac{\kappa}{2}\hat{z} \times \mathbf{r}_\perp = \frac{\kappa}{2}(-y\hat{x} + x\hat{y})$. Then $\Pi_x = -\frac{i}{\kappa}\frac{\partial}{\partial x} + \frac{\kappa}{2}y$, $\Pi_y = -\frac{i}{\kappa}\frac{\partial}{\partial y} - \frac{\kappa}{2}x$ and $\Pi_z = 0$. $a = \Pi_x + i\Pi_y$, $a^\dagger = \Pi_x - i\Pi_y$ and $\left[a, a^\dagger\right] = 2$. Then the "Hamiltonian" above becomes $\Pi^2 = a^\dagger a + 1$

$$\left(a^\dagger a + 1\right)\psi_A = \psi_A$$

$$\left(a^{\dagger}a\right)\psi_A = 0$$

with ψ_a corresponding to the lowest Landau level. In that case applying the lowering operator gives $a\psi_A = 0$. Then expressing the order parameter as $\psi_A = |\psi_A| \exp[i\varphi]$ we get

$$\left(-\frac{i}{\kappa}\frac{\partial}{\partial x} - A_x + \frac{1}{\kappa}\frac{\partial}{\partial y} - iA_y\right)|\psi_A| \exp[i\varphi] = 0\,.$$

Applying the operators and grouping the terms as pure real or pure imaginary leads to

$$\left(-A_x|\psi_A| + |\psi_A|\frac{1}{\kappa}\frac{\partial\varphi}{\partial x} + \frac{1}{\kappa}\frac{\partial|\psi_A|}{\partial y}\right) + i\left(-A_y|\psi_A| + |\psi_A|\frac{1}{\kappa}\frac{\partial\varphi}{\partial y} - \frac{1}{\kappa}\frac{\partial|\psi_A|}{\partial x}\right) = 0$$

The real part and imaginary part must both equal zero. This gives the following relationships:

$$\frac{\partial|\psi_A|}{\partial y} = \kappa|\psi_A|\left(A_x - \frac{1}{\kappa}\frac{\partial\varphi}{\partial x}\right)$$

$$\frac{\partial|\psi_A|}{\partial x} = \kappa|\psi_A|\left(-A_y + \frac{1}{\kappa}\frac{\partial\varphi}{\partial y}\right)$$

Taking derivatives of the modulus squared $\frac{\partial|\psi_A|^2}{\partial y} = 2|\psi_A|\frac{\partial|\psi_A|}{\partial y}$ and $\frac{\partial|\psi_A|^2}{\partial x} = 2|\psi_A|\frac{\partial|\psi_A|}{\partial x}$. Then substitute in the above $\frac{\partial|\psi_A|}{\partial x}$ and $\frac{\partial|\psi_A|}{\partial y}$:

$$\frac{\partial|\psi_A|^2}{\partial y} = -2\kappa|\psi_A|^2\left(-A_x + \frac{1}{\kappa}\frac{\partial\varphi}{\partial x}\right)$$

$$\frac{\partial|\psi_A|^2}{\partial x} = 2\kappa|\psi_A|^2\left(-A_y + \frac{1}{\kappa}\frac{\partial\varphi}{\partial y}\right)$$

The supercurrent is $\mathbf{j} = |\psi_A|^2\left(-\mathbf{A} + \frac{1}{\kappa}\nabla\varphi\right)$ and $\omega_A = |\psi_A|^2$

$$j_x = -\frac{1}{2\kappa}\frac{\partial\omega_A}{\partial y}$$

$$j_y = \frac{1}{2\kappa}\frac{\partial \omega_A}{\partial x}$$

equivalently:

$$\mathbf{j} = -\frac{1}{2\kappa}\nabla\omega_A \times \hat{z} \tag{142}$$

Equation (142) tells us that the supercurrent is perpendicular to the order parameter gradient, or in other words the lines of current lie on the contours of constant ω_A. The last equation can be written as $\mathbf{j} = \nabla \times \left(-\frac{1}{2\kappa}\omega_A \hat{z}\right)$. Further, with $\mathbf{B} = B\hat{z}$, Ampère's law in reduced units is $\mathbf{j} = \nabla \times (B\hat{z})$ and we obtain:

$$\nabla \times \left[\left(B + \frac{1}{2\kappa}\omega_A\right)\hat{z}\right] = 0$$

So the local induction is equal to $-\frac{1}{2\kappa}\omega_A$ plus the gradient of some function $f(\mathbf{r}_\perp, z)$ (this is not the order parameter magnitude). $B\hat{z} = -\frac{1}{2\kappa}\omega_A\hat{z} + \nabla f$, where $f = f(\mathbf{r}_\perp, z)$ is some unknown function with $\nabla_\perp f = 0$.

$$B(\mathbf{r}_\perp) = -\frac{1}{2\kappa}\omega_A(\mathbf{r}_\perp) + \frac{\partial f}{\partial z}$$

$\frac{\partial f}{\partial z}$ must be a constant and with $\omega_A(0) = 0$:

$$B(\mathbf{r}_\perp) = B(0) - \frac{1}{2\kappa}\omega_A(\mathbf{r}_\perp) \tag{143}$$

This is true at all locations and for flux lines of any multiplicity. In the high induction regime the validity of the Linearized GL Equation, Eq. (141), comes from the fact that the order parameter magnitude is small. This is also the case close to the core of a vortex at any induction. So, in this region, $r_\perp \ll \lambda, \xi$, we have:

$$B(\mathbf{r}_\perp) \approx B(0) - \frac{1}{2\kappa}\omega(\mathbf{r}_\perp) \tag{144}$$

For the special case $\kappa^2 = \frac{1}{2}$ we have $H_{c1} = H_{c2} = H_c$, and in reduced units $H_{c2} = \kappa$. The above derivations for ω_A were for $H_a \approx H_{c2}$ and in general for the mixed state $H_{c1} \leq H_a \leq H_{c2}$. Also in general, at the vortex core (again in reduced units) $B(0) \leq H_{c2}$ - otherwise the superconductivity would be suppressed in a finite radius. Of course $B(0)$ must be larger than the lower critical field. So $B(0) = \kappa$ for this special case $\kappa^2 = \frac{1}{2}$

$$\frac{1}{\sqrt{2}} B(\mathbf{r}_\perp) = 1 - \omega(\mathbf{r}_\perp) \tag{145}$$

This special case also has the odd result that for a constant applied field, $H_a = H_c$, all vortex states are degenerate in free energy. This value of κ straddles the line between type-I and type-II. Luk'yanchuk [41] showed that this degeneracy is lifted by including higher order terms in the Ginzburg-Landau free energy functional, Eq. (6). We keep to the standard GL functional but as a test of our model Eq. (145) is quite useful.

Finally, a useful result from Eq. (142):

$$\mathbf{Q}_A = \frac{1}{2\kappa} \frac{\nabla \omega_A \times \hat{z}}{\omega_A} \tag{146}$$

where $\mathbf{Q}_A$ is the Abrikosov supervelocity. Note that $\mathbf{Q}_A$ is independent of $\langle \omega_A \rangle$.

G Fourier Expansion for $\mathbf{Q}_A$

Much of this appendix is reformulating results from Brandt [42, 43]. Brandt only considered singles and we wish to generalize his results because having a Fourier expansion for the Abrikosov supervelocity, $\mathbf{Q}_A$, is key to our solution of the linearized GL equation for doubles in Appendix H.

The supervelocity, $\mathbf{Q}$, is the velocity field for the condensed state. Multiplied by the charge and density of superconducting electrons it gives the supercurrent. From section 2.6 in reduced units the supervelocity is defined $\mathbf{Q} \equiv \mathbf{A} - \frac{1}{\kappa}\nabla\varphi$, with the order parameter phase, φ, being indeterminate at the vortex core. For small $r_\perp$ $\varphi = p\theta$ and we can say about its gradient that $\nabla\varphi = \frac{p}{r_\perp}\hat{\theta} = -p\frac{\mathbf{r}_\perp \times \hat{z}}{r_\perp^2}$. This tells us that $\mathbf{Q}$ is singular at $r = 0$. However, the two physical quantities involving the supervelocity, the current $-|\psi|^2 \mathbf{Q}$ and kinetic energy density term $|\psi|^2 |\mathbf{Q}|^2$, are dominated by the small $r_\perp$ behavior of the order parameter and both quantities go to zero as $r_\perp \to 0$.

The curl of a gradient is zero except that $\nabla\varphi$ is singular at a vortex core. Stokes's theorem yields the result that $\nabla \times \nabla\varphi = p2\pi\delta_2(\mathbf{r}_\perp - \mathbf{R}_{mn})\hat{z}$, where $\mathbf{R}_{mn}$ is a lattice vector of the vortex array. With $\frac{1}{\kappa} = \Phi_0/2\pi$ in reduced units (see Appendix A) this gives $\nabla \times \mathbf{Q} = \nabla \times \mathbf{A} - p\Phi_0\delta_2(\mathbf{r}_\perp - \mathbf{R}_{mn})\hat{z}$. So at all points , except for $\mathbf{r}_\perp = \mathbf{R}_{mn}$, $\mathbf{B} = \nabla \times \mathbf{Q}$. Further, the average value of the curl of the supervelocity over the unit cell is: $\frac{1}{S}\int_S (\nabla \times \mathbf{Q}) \cdot \hat{z}\, dx\, dy = \bar{B} - p\Phi_0 = 0$. This is true at any induction.

Separating the induction in the sample $\mathbf{B}(\mathbf{r}_\perp, z) = \bar{B}\hat{z} + \mathbf{b}(\mathbf{r}_\perp, z)$ leads to a similar separation for the supervelocity $\mathbf{Q}(\mathbf{r}_\perp, z) = \mathbf{Q}_A(\mathbf{r}_\perp) + \mathbf{q}(\mathbf{r}_\perp, z)$ so that $\nabla \times \mathbf{Q}_A = \left[\bar{B} - p\Phi_0\delta_2(\mathbf{r}_\perp - \mathbf{R}_{mn})\right]\hat{z}$ and $\nabla \times \mathbf{q} = \mathbf{b}$. Here we've generalized the Abrikosov supervelocity, $\mathbf{Q}_A$, to any case where the induction is uniform across the sample. $\mathbf{Q}_A$,

is singular at the vortex cores $\mathbf{r}_\perp = \mathbf{R}_{mn}$ and it can be expressed as:

$$\mathbf{Q}_A(\mathbf{r}_\perp) = \hat{z} \times \left[\frac{\bar{B}}{2}\mathbf{r}_\perp - \frac{p}{\kappa} \sum_{m,n} \frac{\mathbf{r}_\perp - \mathbf{R}_{mn}}{|\mathbf{r}_\perp - \mathbf{R}_{mn}|^2} \right] \tag{147}$$

This is identical in form to the supervelocity for the linearized GL equation with the mean induction, $\bar{B}$, replacing the upper critical field value. If we set $\mathbf{b} = 0$ then we get solutions identical to the linearized GL equation differing only in that the unit cell area is larger by a factor $\kappa/\bar{B}$ with the order parameter different by a scaling factor. Just as we generalized the supervelocity we also generalize the order parameter ω_A, it must satisfy Eq. (146) and we set the mean value of the order parameter, $\langle \omega_A \rangle = 1$. The important result is:

$$\omega_A \mathbf{Q}_A = \frac{1}{2\kappa} \nabla \omega_A \times \hat{z} \tag{148}$$

Taking the Fourier transform of Eq. (147)

$$\mathbf{Q}_A(\mathbf{r}_\perp) = \hat{z} \times \sum_{\mathbf{K}_{mn} \neq 0} i\bar{B} \frac{\mathbf{K}_{mn}}{K_{mn}^2} \exp\left[i\mathbf{K}_{mn} \cdot \mathbf{r}_\perp \right] \tag{149}$$

where $\mathbf{K}_{mn}$ are the reciprocal lattice vectors.

H Solving the Linearized GL equation in Terms of the $a_{\mathbf{K}}$

In his pioneering work on vortex lattices in superconductors, Abrikosov [17] showed that for an applied field just below H_{c2}, the first GL equation (when expressed as an equation for the order parameter) has the form of Schrödinger's equation for a charged particle confined to a plane and subject to a magnetic field. With an assumed periodicity of the vortex lines and one flux quantum per vortex, an analytic solution ψ_A exists and can be expressed [17, 18, 49] in terms of a Jacobi theta function,

$$\psi_A(x,y) = e^{-\pi y^2/x_1 y_2}\vartheta_1\left(\frac{\pi}{x_1}(x+iy), \frac{x_2+iy_2}{x_1}\right) \tag{150}$$

where $\vartheta_1(z,\tau) \equiv 2\sum_{n=0}^{\infty}(-)^n e^{i\pi\tau\left(n+\frac{1}{2}\right)^2}\sin(2n+1)z$ and the lattice parameters x_1, x_2 and y_2 were defined just below Eq. (31). With this form for ψ_A its modulus squared, $\omega_A \equiv |\psi_A|^2$, is expressed as a double sum. This leads [42] to the Fourier like expansion of real terms, $\omega_A = \sum_{\mathbf{K}} a^A_{\mathbf{K}}[1-\cos(\mathbf{K}\cdot\mathbf{r})]$, with $a^A_{\mathbf{K}} = -(-)^{m+mn+n} e^{-K^2_{mn}S/8\pi}$. Note that the sum over $\mathbf{K}$ is still a double sum over m and n.

Lasher [50] pointed out that for vortices of multiplicity p, $\psi^{(p)}_A(r) = \left[\psi_A\left(r/\sqrt{p}\right)\right]^p$ is a corresponding solution of the linearized GL equations. In principle one could use this form to determine $a^A_{\mathbf{K}}$ for doubles in the expansion (28), starting from (150), but we did not attempt to carry that through.

We have taken an alternative approach based on numerical solution of a linear system for the $a^A_{\mathbf{K}}$ derived from the linearized GL equations. Combing Eq. (148) and

Eq. (149)

$$\frac{1}{2\kappa}\nabla\omega_A \times \hat{\mathbf{z}} = -\omega_A \left[\sum_{\mathbf{K}_{mn}\neq 0} i\bar{B}\frac{\mathbf{K}_{mn}}{K_{mn}^2}\exp\left[i\mathbf{K}_{mn}\cdot\mathbf{r}_\perp\right]\right]\times\hat{z} \tag{151}$$

Combining with (29), then applying uniqueness of Fourier series leads to the linear system

$$\sum_{\mathbf{K}_i} A_{ji} a^A_{\mathbf{K}_i} = -\langle\omega_A\rangle \tag{152}$$

with

$$A_{ji} \equiv C_{ji} - \delta_{\mathbf{K}_i,\mathbf{K}_j}\frac{1}{2\bar{B}\kappa}\left|\mathbf{K}_j\right|^2 + \delta_{\mathbf{K}_i,\mathbf{K}_j/2}\frac{1}{8\bar{B}\kappa}\left|\mathbf{K}_j\right|^2 \tag{153}$$

and

$$\begin{aligned} C_{ji} \equiv &-\frac{\left|\mathbf{K}_j\right|^2 - \mathbf{K}_i\cdot\mathbf{K}_j}{\left|\mathbf{K}_j-\mathbf{K}_i\right|^2} - \frac{\left|\mathbf{K}_j\right|^2 + \mathbf{K}_i\cdot\mathbf{K}_j}{\left|\mathbf{K}_j+\mathbf{K}_i\right|^2} \\ &+ \frac{\left|\mathbf{K}_j\right|^2 - 2\mathbf{K}_i\cdot\mathbf{K}_j}{4\left|\mathbf{K}_j-2\mathbf{K}_i\right|^2} + \frac{\left|\mathbf{K}_j\right|^2 + 2\mathbf{K}_i\cdot\mathbf{K}_j}{4\left|\mathbf{K}_j+2\mathbf{K}_i\right|^2} \end{aligned} \tag{154}$$

We follow Brandt's convention that $\langle\omega_A\rangle = 1$, so $(3/2)\sum_{\mathbf{K}} a^A_{\mathbf{K}} = 1$.

The infinite system of equations (152) could be rendered finite by setting $a^A_{\mathbf{K}} = 0$ for $|\mathbf{K}| > K_{\max}$; however, this is not a good closure assumption because of slow convergence with increasing $K_{\max}$. Eq. (153) shows the strong connection between $a^A_{\mathbf{K}}$ and $a^A_{\mathbf{K}/2}$ previously mentioned in Sec. 4.4. In particular, for $K_{\max}/2 < |\mathbf{K}| \leq K_{\max}$ the corresponding $a^A_{\mathbf{K}}$ are connected to coefficients associated with vectors beyond the cutoff. In addition, as $|\mathbf{K}_j| \to \infty$, $C_{ji} \to -3/2$, which leads to $a^A_{\mathbf{K}} \approx a^A_{\mathbf{K}/2}/4$ at large $|\mathbf{K}|$. (For large $|\mathbf{K}_j|$, $\sum_{\mathbf{K}_i} C_{ji} a^A_{\mathbf{K}_i} \approx -(3/2)\sum_{\mathbf{K}} a^A_{\mathbf{K}} = -\langle\omega_A\rangle$, hence the latter two terms on the right side of Eq. (153) must sum to zero.) We therefore set $a^A_{2\mathbf{K}} = a^A_{\mathbf{K}}/4$, $a^A_{4\mathbf{K}} = a^A_{\mathbf{K}}/16$, and so on for $K_{\max}/2 < |\mathbf{K}| \leq K_{\max}$ and this leads to a modified linear

system with coefficients A'_{ji}. For i such that $K_{\max}/2 < |\mathbf{K}_i| \leq K_{\max}$,

$$A'_{ji} = A_{ji} + \sum_{l=1}^{\infty} 4^{-l} C_{j,2^l i} \tag{155}$$

with $\mathbf{K}_{2^l i} \equiv 2^l \mathbf{K}_i$. We truncate the sum at $l = 4$ after finding no change in the results for $a^A_{\mathbf{K}}$ when further terms are included.

In Figs. 25 and 26 we show the results of numerically solving the linear system for $\kappa = 1$ and $K_{\max} = 36$. In the former only $a^A_{\mathbf{K}}$ for fundamental reciprocal lattice vectors are shown; while in the latter $a^A_{\mathbf{K}}$ for reciprocal lattice vectors that are powers of two times several different fundamentals are displayed, showing that $a^A_{\mathbf{K}} \approx a^A_{\mathbf{K}/2}/4$ holds even for $|\mathbf{K}|$ not very large.

Finally, let us note that as a check on this approach to solving the linearized GL equations we have carried an analogous analysis for singles. The numerical results from solving the corresponding linear equation for the $a^A_{\mathbf{K}}$ match the exact, analytic results.

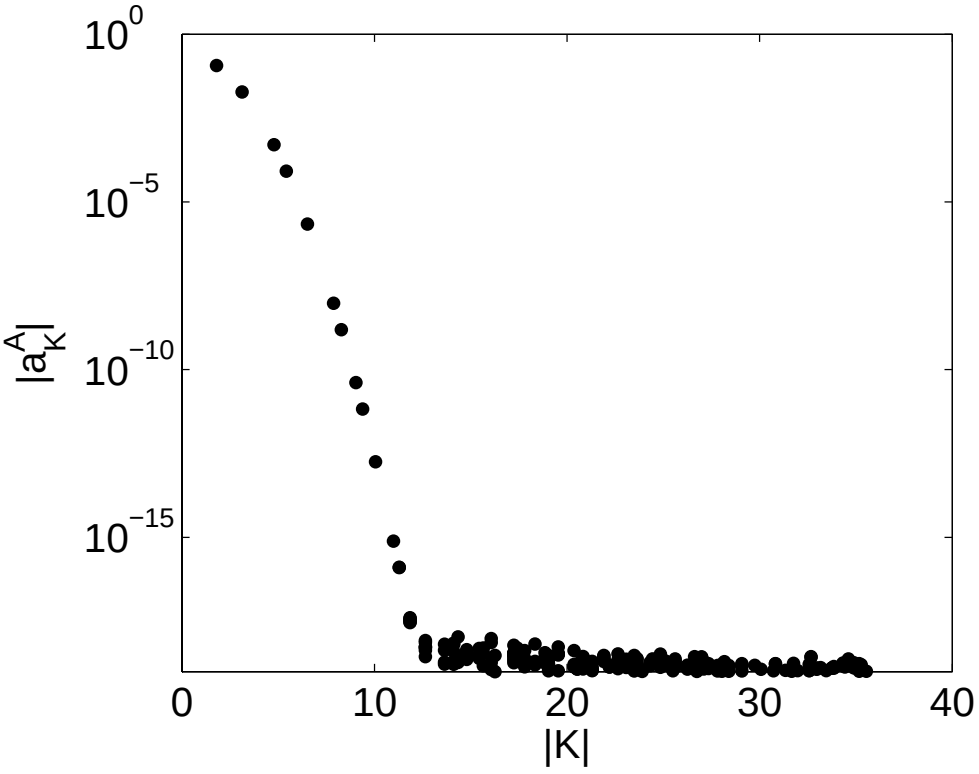

Figure 25: $a_{\mathbf{K}}^A$ Fundamentals

Solutions to the linear system for the $a_{\mathbf{K}}^A$ associated with fundamental reciprocal lattice vectors. See Appendix H.

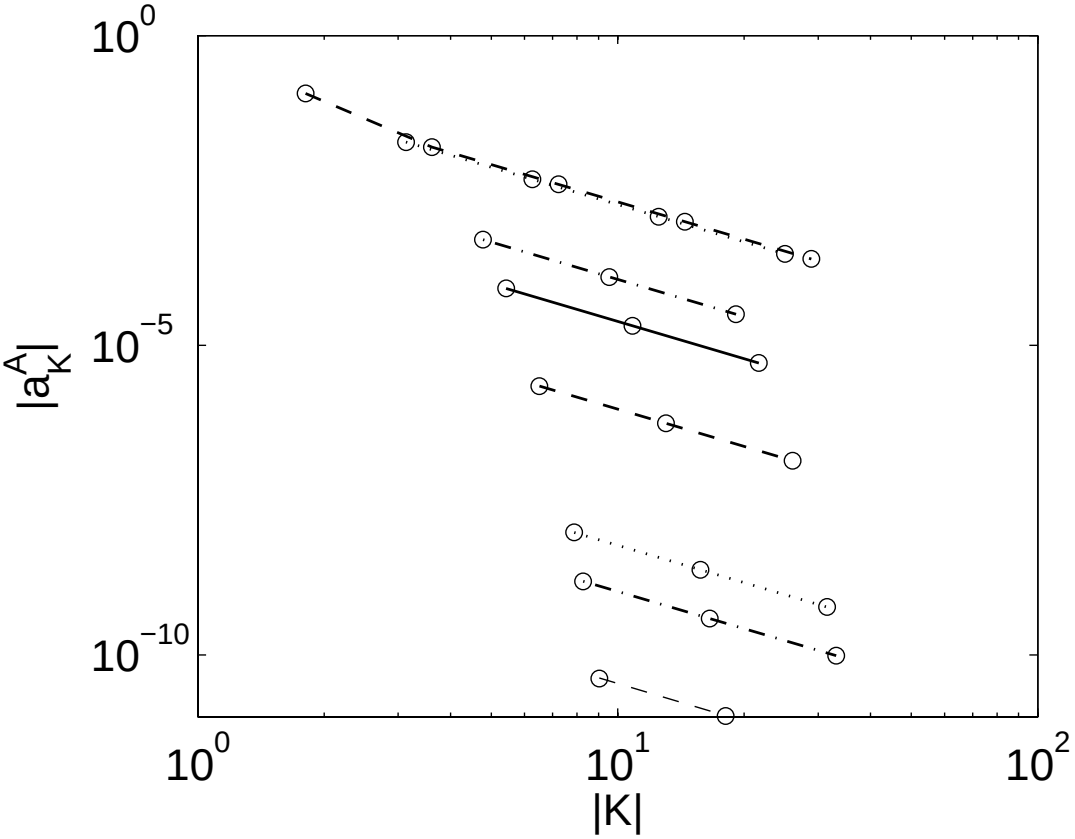

Figure 26: $a^A_{\mathbf{K}}$ Families

Solutions to the linear system for the $a^A_{\mathbf{K}}$ associated with eight fundamental reciprocal lattice vectors and those vectors multiplied by powers of two. The lines are guides to the eye connecting $a^A_{\mathbf{K}}$, $a^A_{2\mathbf{K}}$, $a^A_{4\mathbf{K}}$,...

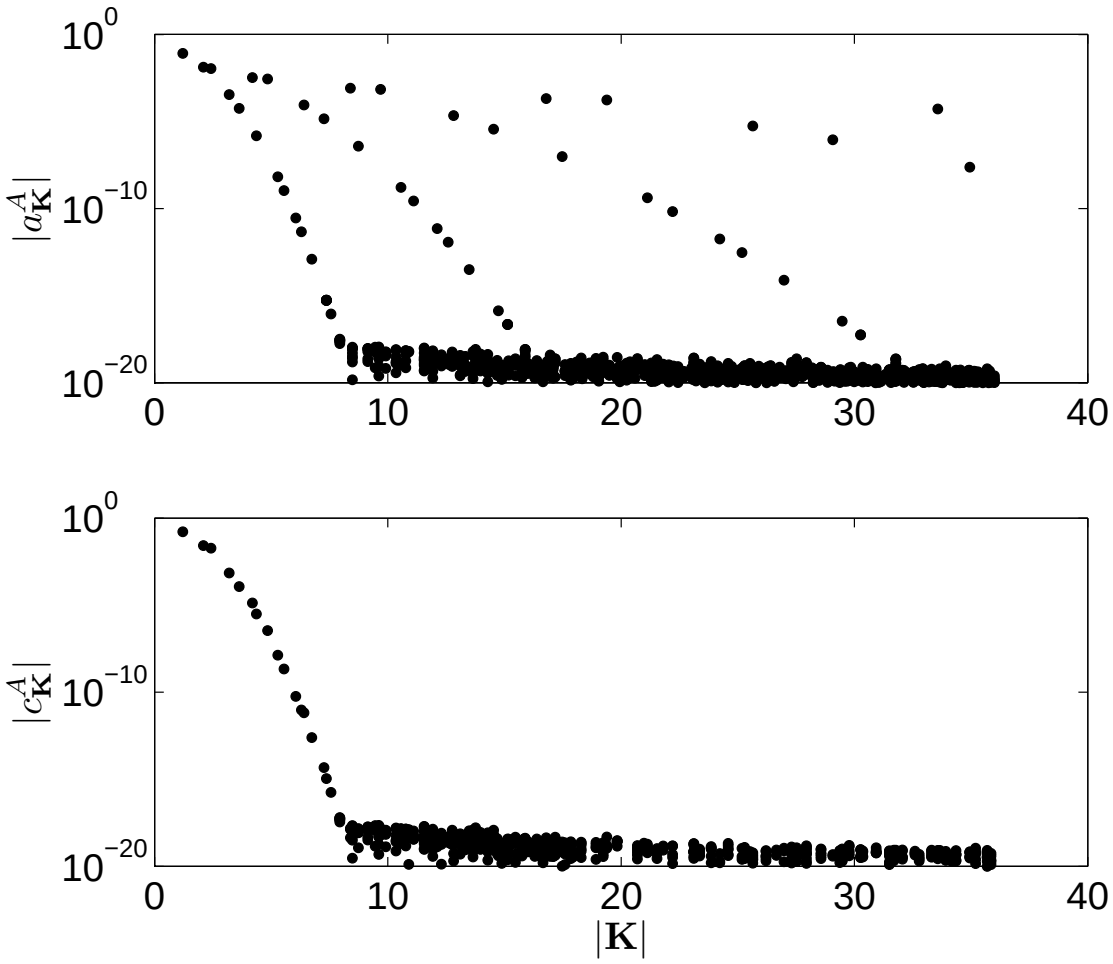

Figure 27: $a^A_{\mathbf{K}}$ and $c^A_{\mathbf{K}}$

Upper plot shows all $a^A_{\mathbf{K}}$ from our solution to the linear system. Lower plot shows $c^A_{\mathbf{K}} = 2a^A_{\mathbf{K}} - \frac{1}{2}a^A_{\mathbf{K}/2}$.

I Second GL Equation Iteration

In this section we will derive the second GL equation iteration step. Brandt [20] gives the starting step, his Eq. (10), and result, Eq. (13), but its not entirely clear that one follows from the other. Also, the earlier result appears to differ from a later result, Eq. (B12) in [21]. However, in both papers there is a typo in the expansion of $\nabla\omega \times \mathbf{Q}$. For those reasons we wish to show the full derivation. We start from the second GL equation, Eq. (16)

$$\nabla \times \mathbf{B} = -\omega\mathbf{Q}$$

take the curl of both sides

$$\nabla \times (\nabla \times \mathbf{B}) = \nabla \times (-\omega\mathbf{Q})$$

$$\nabla \left[\nabla \cdot \mathbf{B}\right] - \nabla^2\mathbf{B} = \nabla \times (-\omega\mathbf{Q})$$

$$\nabla^2\mathbf{B} = \nabla \times (\omega\mathbf{Q})$$

Expand the right hand side

$$\nabla^2\mathbf{B} = \nabla\omega \times \mathbf{Q} + \omega\nabla \times \mathbf{Q}$$

$$\nabla^2\mathbf{B} = \nabla\omega \times \mathbf{Q} + \omega\nabla \times \left(\mathbf{A} - \frac{1}{\kappa}\nabla\varphi\right)$$

$$\nabla^2\mathbf{B} = \nabla\omega \times \mathbf{Q} + \omega\nabla \times \mathbf{A} - \frac{1}{\kappa}\omega\nabla \times \nabla\varphi$$

$$\nabla^2\mathbf{B} = \nabla\omega \times \mathbf{Q} + \omega\mathbf{B} - \frac{1}{\kappa}\omega\nabla \times \nabla\varphi$$

We must consider the term $\omega\nabla\times\nabla\varphi$. Away from a vortex core the curl of the phase gradient will be zero. Near the core we have $\nabla\varphi=\left(\frac{p}{r}\hat{\theta}\right)$ and $\omega=cr^{2p}$ (see Appendix E). The phase is undefined at the vortex core and as $r\to 0$, $|\nabla\varphi|\to\infty$. The curl of this gradient gives a delta function but we wish to show that $\omega\nabla\times\nabla\varphi$ is well behaved at all locations.

$$\omega\nabla\times\nabla\varphi=\nabla\times(\omega\nabla\varphi)-\nabla\omega\times\nabla\varphi$$

$$\omega\nabla\times\nabla\varphi=c\left[\nabla\times\left(r^{2p}\frac{p}{r}\hat{\theta}\right)-2pr^{2p-1}\hat{r}\times\left(\frac{p}{r}\hat{\theta}\right)\right]$$

$$\omega\nabla\times\nabla\varphi=c\left[\nabla\times\left(pr^{2p-1}\hat{\theta}\right)-2p^2r^{2p-2}\hat{z}\right]$$

For the first term in brackets we have $\nabla\times\left(pr^{2p-1}\hat{\theta}\right)=p\frac{1}{r}\frac{\partial}{\partial r}\left(rr^{2p-1}\right)\hat{z}=2p^2r^{2p-2}\hat{z}$. We obtain the result (true at all locations):

$$\omega\nabla\times\nabla\varphi=0 \tag{156}$$

Returning to the derivation,

$$\nabla^2\mathbf{B}=\nabla\omega\times\mathbf{Q}+\omega\mathbf{B}\,,$$

we add a stabilizing term, $-\overline{\omega}\mathbf{B}$ to both sides

$$\left(\nabla^2-\overline{\omega}\right)\mathbf{B}=\nabla\omega\times\mathbf{Q}+\left(\omega-\overline{\omega}\right)\mathbf{B}\,.$$

$\overline{\omega}$ is the mean value of the order parameter. We use this expression only in the bulk case where $\mathbf{B}=B\hat{z}$ and $\frac{\partial\omega}{\partial z}=0$ (in equilibrium, in all cases, $Q_z=0$). We then obtain a London like inhomogeneous equation:

$$\left(\nabla^2-\overline{\omega}\right)B=\left(\frac{\partial\omega}{\partial x}Q_y-\frac{\partial\omega}{\partial y}Q_x\right)+\left(\omega-\overline{\omega}\right)B \tag{157}$$

It is this equation which is the basis for both Brandt's original iteration equation for singles and our iteration equation for doubles.

For the singly quantized vortices

$$B(\mathbf{r}) = \bar{B} + \sum_{\mathbf{K}} b_{\mathbf{K}} \cos(\mathbf{K} \cdot \mathbf{r})$$

and with $\langle \cos(\mathbf{K} \cdot \mathbf{r}) \cos(\mathbf{K}' \cdot \mathbf{r}) \rangle = \frac{1}{2}\delta_{KK'}$, we find

$$-\frac{1}{2}\left(|\mathbf{K}|^2 + \overline{\omega}\right) b_{\mathbf{K}} = \left\langle \left[\left(\frac{\partial \omega}{\partial x} Q_y - \frac{\partial \omega}{\partial y} Q_x \right) + (\omega - \overline{\omega}) B \right] \cos(\mathbf{K} \cdot \mathbf{r}) \right\rangle .$$

Yielding the correct iteration equation for singles:

$$b_{\mathbf{K}} = -\frac{2}{|\mathbf{K}|^2 + \overline{\omega}} \left\langle \left[\left(\frac{\partial \omega}{\partial x} Q_y - \frac{\partial \omega}{\partial y} Q_x \right) + (\omega - \overline{\omega}) B \right] \cos(\mathbf{K} \cdot \mathbf{r}) \right\rangle$$

J Free Energy Functional Integrals and Gradient

In this appendix we define, derive and summarize several of the quantities and relations used in Sec. 5. The primary purpose is show the derivations for the expressions used in the iterative $b_{\mathbf{K}_\perp l}$ coefficient updates described in Sec. 5.1. The free energy functional, referenced from normal state, with just induction term dependencies is: $F_b = \langle \omega Q^2 + b_\perp^2 + b_z^2 \rangle + \frac{1}{d} F_{Stray}$.

J.1 Orthogonality

First we repeat the conventions used for averaging over the unit cell. The angle bracket notation is used for averaging over the unit cell area, film thickness or both.

$$\langle \ldots \rangle_{xy} \equiv \frac{1}{S} \int_S \ldots \, dx \, dy \tag{158}$$

$$\langle \ldots \rangle_{z} \equiv \frac{1}{d} \int_{-d/2}^{d/2} \ldots \, dz \tag{159}$$

$$\langle \ldots \rangle \equiv \frac{1}{Sd} \int_{-d/2}^{d/2} \int_S \ldots \, dx \, dy \, dz \tag{160}$$

We then have the following orthogonality relations for the basis functions we employ:

$$\langle \cos\left(\mathbf{K}_\perp \cdot \mathbf{r}_\perp\right) \cos\left(\mathbf{K}'_\perp \cdot \mathbf{r}_\perp\right) \rangle_{xy} = \frac{1}{2} \delta_{\mathbf{K}_\perp, \mathbf{K}'_\perp} \tag{161}$$

$$\langle \sin\left(\mathbf{K}_\perp \cdot \mathbf{r}_\perp\right) \sin\left(\mathbf{K}'_\perp \cdot \mathbf{r}_\perp\right) \rangle_{xy} = \frac{1}{2} \delta_{\mathbf{K}_\perp, \mathbf{K}'_\perp} \tag{162}$$

$$\langle \cos\left(K_z z\right) \cos\left(K'_z z\right) \rangle_{z} = \frac{1}{2} \delta_{K_z, K'_z} \left(1 + \delta_{K_z, 0}\right) \tag{163}$$

$$\left\langle P_{2l}\left(\frac{2}{d}z\right)P_{2l'}\left(\frac{2}{d}z\right)\right\rangle_z = \delta_{ll'}\frac{1}{4l+1} \tag{164}$$

Recursively applying the recurrence relations for Legendre polynomials gives the following two identities:

$$\left\langle \frac{d}{dz}P_{2l}\left(\frac{2}{d}z\right)\frac{d}{dz}P_{2l'}\left(\frac{2}{d}z\right)\right\rangle_z = \frac{2}{d^2}2n\left(2n+1\right),\ n=\min\left(l,l'\right) \tag{165}$$

$$\left\langle \frac{d^2}{dz^2}P_{2l}\left(\frac{2}{d}z\right)P_{2l'}\left(\frac{2}{d}z\right)\right\rangle_z = \frac{2}{d^2}\left[2l\left(2l+1\right)-2l'\left(2l'+1\right)\right],\ l\geq l' \tag{166}$$

J.2 Singles

For the lattice of singly quantized vortices in films we use Brandt's Ansatz [43] for the order parameter unchanged but we do modify the induction terms. We repeat our Ansatz for $\mathbf{b}$ and $\mathbf{q}$ from Sec. 5:

$$b_z\left(\mathbf{r}_\perp,z\right) = \sum_{\mathbf{K}_\perp,l} b_{\mathbf{K}_\perp l}\cos\left(\mathbf{K}_\perp\cdot\mathbf{r}_\perp\right)P_{2l}\left(2z/d\right) \tag{167}$$

$$\mathbf{b}_\perp\left(\mathbf{r}_\perp,z\right) = \sum_{\mathbf{K}_\perp,l} b_{\mathbf{K}_\perp l}\frac{-\mathbf{K}_\perp}{K_\perp^2}\sin\left(\mathbf{K}_\perp\cdot\mathbf{r}_\perp\right)\frac{2}{d}P'_{2l}\left(2z/d\right) \tag{168}$$

$$\mathbf{q}\left(\mathbf{r}_\perp,z\right) = \sum_{\mathbf{K}_\perp,l} b_{\mathbf{K}_\perp l}\frac{\hat{\mathbf{z}}\times\mathbf{K}}{|\mathbf{K}^2|}\sin\left(\mathbf{K}_\perp\cdot\mathbf{r}_\perp\right)P_{2l}\left(2z/d\right) \tag{169}$$

We then obtain the following analytic derivatives for the energy components:

$$\left\langle b_z^2\right\rangle = \frac{1}{2}\sum_{\mathbf{K}_\perp,l} b_{\mathbf{K}_\perp l}^2\frac{1}{4l+1} \tag{170}$$

$$\left\langle b_\perp^2\right\rangle = \frac{1}{d^2}\sum_{\mathbf{K}_\perp}\frac{1}{K_\perp^2}\sum_{l=0}^{N_l-1} b_{\mathbf{K}_\perp l}\left[\sum_{l'=0}^{l} b_{\mathbf{K}_\perp l'}2l'\left(2l'+1\right)+\sum_{l'=l+1}^{N_l-1} b_{\mathbf{K}_\perp l'}2l\left(2l+1\right)\right] \tag{171}$$

$$\frac{1}{d}F_{stray} = \frac{1}{d}\sum_{\mathbf{K}_\perp}\frac{1}{K_\perp}\left(b^S_{\mathbf{K}_\perp}\right)^2,\ b^S_{\mathbf{K}_\perp} \equiv \sum_l b_{\mathbf{K}_\perp,l} \tag{172}$$

Since we minimize the free energy functional directly with respect to $b_{\mathbf{K}_\perp l}$ we need the following gradient terms:

$$\frac{\partial}{\partial b_{\mathbf{K}_\perp l}}\left\langle b_z^2\right\rangle = b_{\mathbf{K}_\perp l}\frac{1}{4l+1} \tag{173}$$

$$\frac{\partial}{\partial b_{\mathbf{K}_\perp l}}\left\langle b_\perp^2\right\rangle = \frac{1}{d^2}\frac{2}{K_\perp^2}\left[\sum_{l'=0}^{l} b_{\mathbf{K}_\perp l'}2l'\left(2l'+1\right) + \sum_{l'=l+1}^{N_l-1} b_{\mathbf{K}_\perp l'}2l\left(2l+1\right)\right] \tag{174}$$

$$\frac{\partial}{\partial b_{\mathbf{K}_\perp l}}\frac{1}{d}F_{stray} = \frac{2}{d}\frac{1}{K_\perp}b^S_{\mathbf{K}_\perp} = \frac{2}{d}\frac{1}{K_\perp}\sum_{l'} b_{\mathbf{K}_\perp,l'} \tag{175}$$

While the supercurrent energy term, $\langle\omega Q^2\rangle_{\mathrm{G}}$, and its gradient must be integrated numerically we can somewhat simplify the latter's form. First note that

$$\frac{\partial}{\partial b_{\mathbf{K}_\perp l}}\left\langle\omega Q^2\right\rangle = 2\left\langle\omega\mathbf{Q}\cdot\frac{\partial\mathbf{q}}{\partial b_{\mathbf{K}_\perp l}}\right\rangle_{\mathrm{G}} \tag{176}$$

$$\frac{\partial}{\partial b_{K_\perp,l}}\mathbf{q} = \frac{\hat{\mathbf{z}}\times\mathbf{K}}{K_\perp^2}\sin\left(\mathbf{K}_\perp\cdot\mathbf{r}_\perp\right)P_{2l}\left(\frac{2}{d}z\right) \tag{177}$$

$$\frac{\partial}{\partial b_{K_\perp,l}}\left\langle\omega Q^2\right\rangle_{\mathrm{G}} = \frac{2}{K_\perp^2}\left\langle\omega\left(Q_yK_x - Q_xK_y\right)\sin\left(\mathbf{K}_\perp\cdot\mathbf{r}_\perp\right)P_{2l}\left(\frac{2}{d}z\right)\right\rangle_{\mathrm{G}} \tag{178}$$

and with the definition $D_{\mathbf{K}_\perp l} \equiv \left\langle\omega\left(Q_yK_x - Q_xK_y\right)\sin\left(\mathbf{K}_\perp\cdot\mathbf{r}_\perp\right)P_{2l}\left(\frac{2}{d}z\right)\right\rangle_{\mathrm{G}}$ we obtain

$$\frac{\partial}{\partial b_{K_\perp,l}}\left\langle\omega Q^2\right\rangle_{\mathrm{G}} = \frac{2}{K_\perp^2}D_{\mathbf{K}_\perp l} \tag{179}$$

J.3 Doubles

For the doubly quantized vortices in films we again repeat our Ansatz for the induction terms,

$$b_z(\mathbf{r}_\perp, z) = \sum_{\mathbf{K}_\perp, l} \left[2b_{\mathbf{K}_\perp l} - \frac{1}{2} b_{\mathbf{K}_\perp/2, l} \right] \cos(\mathbf{K}_\perp \cdot \mathbf{r}_\perp) P_{2l}(2z/d) \tag{180}$$

$$\mathbf{b}_\perp(\mathbf{r}_\perp, z) = \sum_{\mathbf{K}_\perp, l} \left[2b_{\mathbf{K}_\perp l} - \frac{1}{2} b_{\mathbf{K}_\perp/2, l} \right] \frac{-\mathbf{K}_\perp}{K_\perp^2} \sin(\mathbf{K}_\perp \cdot \mathbf{r}_\perp) \frac{2}{d} P'_{2l}(2z/d) \tag{181}$$

$$\mathbf{q}(\mathbf{r}_\perp, z) = \sum_{\mathbf{K}_\perp, l} \left[2b_{\mathbf{K}_\perp l} - \frac{1}{2} b_{\mathbf{K}_\perp/2, l} \right] \frac{\hat{\mathbf{z}} \times \mathbf{K}}{K_\perp^2} \sin(\mathbf{K}_\perp \cdot \mathbf{r}_\perp) P_{2l}(2z/d) \tag{182}$$

The orthogonality relationships and Legendre polynomial identities from Sec. J.1 allow us to analytically integrate the following free energy terms:

- $\langle b_z^2 \rangle = \frac{1}{2} \sum_{K_\perp, l} \left[2b_{\mathbf{K}_\perp l} - \frac{1}{2} b_{\mathbf{K}_\perp/2, l} \right]^2 \frac{1}{4l+1}$
- $\langle b_\perp^2 \rangle = \frac{1}{d^2} \sum_{\mathbf{K}_\perp, l, l'} \frac{1}{K_\perp^2} \left[2b_{\mathbf{K}_\perp, l} - \frac{1}{2} b_{\mathbf{K}_\perp/2, l} \right] \left[2b_{\mathbf{K}_\perp, l'} - \frac{1}{2} b_{\mathbf{K}_\perp/2, l'} \right] m_{l,l'}$
  - $m_{l,l'} \equiv \min(2l, 2l') (\min(2l, 2l') + 1)$
- $\frac{1}{d} F_{stray} = \frac{1}{d} \sum_{\mathbf{K}_\perp} \frac{1}{K_\perp} \left(b^S_{\mathbf{K}_\perp} \right)^2$, $b^S_{\mathbf{K}_\perp} \equiv \sum_l \left[2b_{\mathbf{K}_\perp, l} - \frac{1}{2} b_{\mathbf{K}_\perp/2, l} \right]$

The remaining free energy term, $\langle \omega Q^2 \rangle_{\mathrm{G}}$, must be evaluated numerically.

J.3.1 Gradient

The (possibly tedious) details of the calculation of the free energy gradient with respect to the $b_{\mathbf{K}_\perp l}$ coefficients for doubles is included below.

First for the b_z energy:

- $\frac{\partial}{\partial b_{\mathbf{K}'_\perp, l'}} \langle b_z^2 \rangle = \sum_{K_\perp, l} \left[2b_{K_\perp, l} - \frac{1}{2} b_{K_\perp/2, l} \right] \frac{1}{4l+1} \left[2 \frac{\partial}{\partial b_{\mathbf{K}'_\perp, l'}} b_{K_\perp, l} - \frac{1}{2} \frac{\partial}{\partial b_{\mathbf{K}'_\perp, l'}} b_{K_\perp/2, l} \right]$
- $\frac{\partial}{\partial b_{\mathbf{K}'_\perp, l'}} \langle b_z^2 \rangle = \sum_{K_\perp, l} \left[2b_{K_\perp, l} - \frac{1}{2} b_{K_\perp/2, l} \right] \frac{1}{4l+1} \delta_{l,l'} \left[2\delta_{K,K'} - \frac{1}{2} \delta_{K/2,K'} \right]$
- $\frac{\partial}{\partial b_{\mathbf{K}'_\perp, l'}} \langle b_z^2 \rangle = \sum_{K_\perp} \left[2b_{K_\perp, l'} - \frac{1}{2} b_{K_\perp/2, l'} \right] \frac{1}{4l'+1} \left[2\delta_{K,K'} - \frac{1}{2} \delta_{K,2K'} \right]$

- $\frac{\partial}{\partial b_{\mathbf{K}'_\perp,l'}} \langle b_z^2 \rangle = \frac{1}{4l'+1} \sum_{K_\perp} \left[2b_{K_\perp,l'} - \frac{1}{2} b_{K_\perp/2,l'} \right] \left[2\delta_{K,K'} - \frac{1}{2}\delta_{K,2K'} \right]$
- $\frac{\partial}{\partial b_{\mathbf{K}'_\perp,l'}} \langle b_z^2 \rangle = \frac{1}{4l'+1} \left\{ 2 \left[2b_{K'_\perp,l'} - \frac{1}{2} b_{K'_\perp/2,l'} \right] - \frac{1}{2} \left[2b_{2K'_\perp,l'} - \frac{1}{2} b_{K'_\perp,l'} \right] \right\}$
- $\frac{\partial}{\partial b_{\mathbf{K}'_\perp,l'}} \langle b_z^2 \rangle = \frac{1}{4l'+1} \left\{ 4b_{K'_\perp,l'} - b_{K'_\perp/2,l'} - b_{2K'_\perp,l'} + \frac{1}{4} b_{K'_\perp,l'} \right\}$
- $\frac{\partial}{\partial b_{\mathbf{K}'_\perp,l'}} \langle b_z^2 \rangle = \frac{1}{4l'+1} \left\{ \frac{17}{4} b_{K'_\perp,l'} - b_{K'_\perp/2,l'} - b_{2K'_\perp,l'} \right\}$
- $\frac{\partial}{\partial b_{\mathbf{K}'_\perp,l'}} \langle b_z^2 \rangle = \frac{1}{4l'+1} \left\{ \frac{17}{4} b_{K'_\perp,l'} - b_{K'_\perp/2,l'} - b_{2K'_\perp,l'} \right\}$

$$\frac{\partial}{\partial b_{\mathbf{K}_\perp,l}} \langle b_z^2 \rangle = \frac{1}{4l+1} \left\{ \frac{17}{4} b_{K_\perp,l} - b_{K_\perp/2,l} - b_{2K_\perp,l} \right\} \tag{183}$$

Next for the $b_\perp$ energy:

- $\frac{\partial}{\partial \left(b_{\mathbf{K},l}\right)''} \langle b_\perp^2 \rangle = \begin{array}{c} \frac{1}{d^2} \sum_{\mathbf{K},l,l'} \frac{1}{K_\perp^2} \left\{ \left[2\delta_{K,K''}\delta_{l,l''} - \frac{1}{2}\delta_{K,2K''}\delta_{l,l''} \right] \left[2b_{\mathbf{K},l'} - \frac{1}{2} b_{\mathbf{K}/2,l'} \right] + \\ \left[2b_{\mathbf{K},l} - \frac{1}{2} b_{\mathbf{K}/2,l} \right] \left[2\delta_{K,K''}\delta_{l',l''} - \frac{1}{2}\delta_{K,2K''}\delta_{l',l''} \right] \right\} m_{l,l'} \end{array}$
- $\frac{\partial}{\partial \left(b_{\mathbf{K},l}\right)''} \langle b_\perp^2 \rangle = \begin{array}{c} \frac{1}{d^2} \left\{ \sum_{\mathbf{K},l'} \frac{1}{K_\perp^2} \left[2\delta_{K,K''} \left[2b_{\mathbf{K},l'} - \frac{1}{2} b_{\mathbf{K}/2,l'} \right] \right. \right. \\ \left. -\frac{1}{2}\delta_{K,2K''} \left[2b_{\mathbf{K},l'} - \frac{1}{2} b_{\mathbf{K}/2,l'} \right] m_{l'',l'} \right] \\ \left. + \sum_{\mathbf{K},l} \frac{1}{K^2} \left[2b_{\mathbf{K},l} - \frac{1}{2} b_{\mathbf{K}/2,l} \right] \left[2\delta_{K,K''} - \frac{1}{2}\delta_{K,2K''} \right] m_{l'',l} \right\} \end{array}$
- $\frac{\partial}{\partial \left(b_{\mathbf{K},l}\right)''} \langle b_\perp^2 \rangle = \begin{array}{c} \frac{2}{d^2} \sum_{l'} \left[\frac{4}{(K'')^2} b_{\mathbf{K}'',l'} - \frac{1}{(K'')^2} b_{\mathbf{K}''/2,l'} \right. \\ \left. -\frac{1}{4(K'')^2} b_{2\mathbf{K}'',l'} + \frac{1}{4(K'')^2} b_{\mathbf{K}'',l'} \right] m_{l'',l'} \end{array}$
- $\frac{\partial}{\partial b_{\mathbf{K},l}} \langle b_\perp^2 \rangle = \frac{2}{d^2 K_\perp^2} \sum_{l'} \left[4b_{\mathbf{K},l'} - b_{\mathbf{K}/2,l'} - \frac{1}{4} b_{2\mathbf{K},l'} + \frac{1}{4} b_{\mathbf{K},l'} \right] m_{l,l'}$
- $\frac{\partial}{\partial b_{\mathbf{K},l}} \langle b_\perp^2 \rangle = \frac{2}{d^2 K_\perp^2} \sum_{l'} \left[\frac{17}{4} b_{\mathbf{K},l'} - b_{\mathbf{K}/2,l'} - \frac{1}{4} b_{2\mathbf{K},l'} \right] m_{l,l'}$

$$\frac{\partial}{\partial b_{\mathbf{K}_\perp,l}} \langle b_\perp^2 \rangle = \frac{2}{d^2 K_\perp^2} \sum_{l'} \left[\left(\frac{17}{4} b_{K_\perp,l'} - b_{K_\perp/2,l'} - \frac{1}{4} b_{2K_\perp,l'} \right) m_{l,l'} \right] \tag{184}$$

Then the stray field energy:

- $\frac{\partial}{\partial b_{\mathbf{K}_\perp l}} \frac{1}{d} F_{stray} = \frac{2}{d} \sum_{\mathbf{K}'_\perp} \frac{1}{K'_\perp} b^S_{\mathbf{K}'_\perp} \frac{\partial b^S_{\mathbf{K}'_\perp}}{\partial b_{\mathbf{K}_\perp l}}$
- $\frac{\partial}{\partial b_{\mathbf{K}_\perp l}} \frac{1}{d} F_{stray} = \frac{2}{d} \sum_{\mathbf{K}'_\perp} \frac{1}{K'_\perp} b^S_{\mathbf{K}'_\perp} \left[2\delta_{K_\perp,K'_\perp} - \frac{1}{2}\delta_{K_\perp,K'_\perp/2} \right]$
- $\frac{\partial}{\partial b_{\mathbf{K}_\perp l}} \frac{1}{d} F_{stray} = \frac{2}{d} \sum_{\mathbf{K}'_\perp} \frac{1}{K'_\perp} b^S_{\mathbf{K}'_\perp} \left[2\delta_{K_\perp,K'_\perp} - \frac{1}{2}\delta_{2K_\perp,K'_\perp} \right]$

- $\frac{\partial}{\partial b_{\mathbf{K}_\perp l}} \frac{1}{d} F_{stray} = \frac{2}{d} \left[\frac{1}{K_\perp} b^S_{\mathbf{K}_\perp} 2 - \frac{1}{2K_\perp} b^S_{2\mathbf{K}_\perp} \frac{1}{2} \right]$
- $\frac{\partial}{\partial b_{\mathbf{K}_\perp l}} \frac{1}{d} F_{stray} = \frac{2}{d} \left[\frac{1}{K_\perp} 2 b^S_{\mathbf{K}_\perp} - \frac{1}{K_\perp} \frac{1}{4} b^S_{2\mathbf{K}_\perp} \right]$

$$\frac{\partial}{\partial b_{\mathbf{K}\perp,l}} \left(\frac{1}{d} F_{stray} \right) = \frac{2}{dK_\perp} \left[2 b^S_{\mathbf{K}_\perp} - \frac{1}{4} b^S_{2\mathbf{K}_\perp} \right] \tag{185}$$

Finally, the supercurrent energy and gradient integrals must be done numerically but we can somewhat simplify the gradient expression:

- $\frac{\partial}{\partial b_{\mathbf{K}_\perp l}} \langle \omega Q^2 \rangle = 2 \left\langle \omega \mathbf{Q} \cdot \frac{\partial \mathbf{q}}{\partial b_{\mathbf{K}_\perp l}} \right\rangle$
  - $\frac{\partial}{\partial b_{\mathbf{K}_\perp l}} \mathbf{q} = \frac{\hat{\mathbf{z}} \times \mathbf{K}}{K_\perp^2} \left[2 \sin\left(\mathbf{K}_\perp \cdot \mathbf{r}_\perp \right) - \frac{1}{4} \sin\left(\mathbf{K}_\perp \cdot \mathbf{r}_\perp \right) \right] P_{2l} \left(\frac{2}{d} z \right)$
- $\frac{\partial}{\partial b_{\mathbf{K}_\perp l}} \langle \omega Q^2 \rangle = \frac{2}{K_\perp^2} \left\langle \omega (Q_y K_x - Q_x K_y) \left[2 \sin(\mathbf{K}_\perp \cdot \mathbf{r}_\perp) - \frac{1}{4} \sin(2\mathbf{K}_\perp \cdot \mathbf{r}_\perp) \right] P_{2l} \left(\frac{2}{d} z \right) \right\rangle$
  - $D_{\mathbf{K}_\perp,l} \equiv \left\langle \omega (Q_y K_x - Q_x K_y) \left[4 \sin(\mathbf{K}_\perp \cdot \mathbf{r}_\perp) - \frac{1}{2} \sin(2\mathbf{K}_\perp \cdot \mathbf{r}_\perp) \right] P_{2l} \left(\frac{2}{d} z \right) \right\rangle_{\mathrm{G}}$

$$\frac{\partial}{\partial b_{\mathbf{K}_\perp l}} \langle \omega Q^2 \rangle = \frac{1}{K_\perp^2} D_{\mathbf{K}_\perp,l} \tag{186}$$

In the above equations terms like $b_{2K_\perp,l}$, $b^S_{2\mathbf{K}_\perp}$ and $\sin\left(2\mathbf{K}_\perp \cdot \mathbf{r}_\perp\right)$ that have $2|\mathbf{K}_\perp| > K_{MAX}$ are set to zero. These arise from fundamental $\mathbf{K}$ that are excluded due to the coupling between coefficients while working with a finite set of vectors (see discussion on truncation issues in Secs. 4.4 and H).

The order parameter iterations use the first GL equation and our doubles implementation with Eq. (90) leads to the iteration update Eq. (94) that follows quite simply from Brandt's [43] singles implementation.

K Circular Cell for Film Samples

Going from the bulk circular cell to the film circular cell is very similar to the case of the flux line lattice. In Sec. 4.6.1 we defined the bulk CC Ansätze for singles and doubles in terms of the order parameter basis functions $f_m(r)$, Eqs. (45), (57), and the induction terms basis functions $b_{r,n}(r)$ and $b_{z,n}(r)$, Eqs. (46), (58), and Eqs. (47), (59), respectively. Then we can write the order parameter for singles and doubles in the film generically as an expansion of basis functions with the unknown coefficients f_{G,K_z},

$$f(r,z) = \sum_{K_z=0} \sum_{m=1} f_{G,K_z} f_m(r) \cos(K_z z), \; K_z = l\frac{2\pi}{d} \tag{187}$$

where as in the FLL case we use $\cos(K_z z)$ for the z-dependence of the order parameter.

The induction terms are expanded in terms of the unknown coefficients $a_{n,l}$ and we use Legendre functions for the z-dependence

$$B_z(r,z) = \sum_{l=0} \sum_{n=1} a_{n,l} b_{z,n}(r) P_{2l}\left(\frac{2}{d}z\right) + \overline{B} \tag{188}$$

$$b_r(r,z) = -\sum_{l=0} \sum_{n=1} a_{n,l} b_{r,n}(r) \frac{d}{dz}\left[P_{2l}\left(\frac{2}{d}z\right)\right] \tag{189}$$

$$A(r,z) = \sum_{l=0} \sum_{n=1} a_{n,l} b_{r,n}(r) P_{2l}\left(\frac{2}{d}z\right) + \frac{\overline{B}}{2}r \tag{190}$$

$$Q(r,z) = \sum_{l=0} \sum_{n=1} a_{n,l} b_{r,n}(r) P_{2l}\left(\frac{2}{d}z\right) + \frac{\overline{B}}{2}r - \frac{p}{\kappa r} \tag{191}$$

where in the last term p is the fluxoid multiplicity. Finally, the supercurrent

$$j(r,z) = \sum_{l=0}\sum_{n=1} a_{n,l}\left\{-b_{r,n}(r)\frac{d^2}{dz^2}\left[P_{2l}\left(\frac{2}{d}z\right)\right] - \frac{d}{dr}\left[b_{z,n}(r)\right]P_{2l}\left(\frac{2}{d}z\right)\right\} \quad (192)$$

As we discussed in Sec. 4.6.2 in cylindrical coordinates the Bessel functions are the natural choice of basis functions for the radial dependence. But it seems for $p > 1$ there is not tractable combination of Bessel functions that meet the near core requirements. In the free space outside the film the requirements are simpler:

1. $B_z(r,z)$ must be continuous at the film boundary, $|z| = d/2$
2. In addition, we assume no sheet currents so $b_r(r,z)$ must also be continuous at the film boundary
3. As $z \to \infty$, $\mathbf{B}(r,z) \to \bar{B}\hat{z}$
4. No flux passes through the sides of the circular cell so $b_r(R,z) = 0$
5. It is a source free region so $\nabla^2\mathbf{B} = 0$

From these conditions we can conclude that for a fixed z-position $B_z(r,z)$ is maximal at $r = 0$, and for any z that $b_r(0,z) = 0$. So in the space external to the film we have

$$b_r(r,z) = \sum_{m=1} c_m J_1(l_m r)\exp\left(-l_m\left(z - \frac{d}{2}\right)\right) \quad (193)$$

$$b_z(r,z) = \sum_{m=1} c_m J_0(l_m r)\exp\left(-l_m\left(z - \frac{d}{2}\right)\right) \quad (194)$$

$$l_m \equiv \alpha_{1n}/R \quad (195)$$

with $B_z(r,z) = \bar{B} + b_z(r,z)$. Using the Bessel functions in this coordinate system

allows an analytic integral for the stray field energy

$$\frac{1}{d}F_{Stray} = \frac{2R}{d}\sum_{m=1}\frac{c_m^2}{\alpha_{1m}}J_0^2\left(\alpha_{1m}\right)\,. \tag{196}$$

However the unknown c_m coefficients must be determined from a numerical integral based on matching B_z across the film boundary:

$$c_m = \left[\frac{R^2}{2}\left[J_0\left(\alpha_{1m}\right)\right]^2\right]^{-1}\int_0^R b_z\left(r,\frac{d}{2}\right)J_0\left(\alpha_{1m}\frac{r}{R}\right)rdr\,. \tag{197}$$

With this scheme we are successful for the singly quantized vortices - success being defined as convergent solutions that are physically reasonable and match FLL calculations for $\bar{B}$ that is not too low (regions where the FLL and CC are both applicable). However, with doubly quantized vortices in the film CC we did not succeed. The iterations do converge, but they consistently converge on a non-physical result. For any combination of κ, $\bar{B}$, number of coefficients, etc. we get results that are characterized by a local minimum (a dip) in the film for $B_z\left(r,z\right)$ at $r=0$, see Fig. 28.

In our implementation of the CC in films we use the same code for singles and doubles with the appropriate substitution for $b_{z,n}\left(r\right)$ and $b_{r,n}\left(r\right)$. The film implementation uses the same code from the bulk case for the radial dependency and in bulk we do not see the "dip" for doubles. At this point it is still an open problem and it appears that it is an error in our algorithm and not in its implementation.

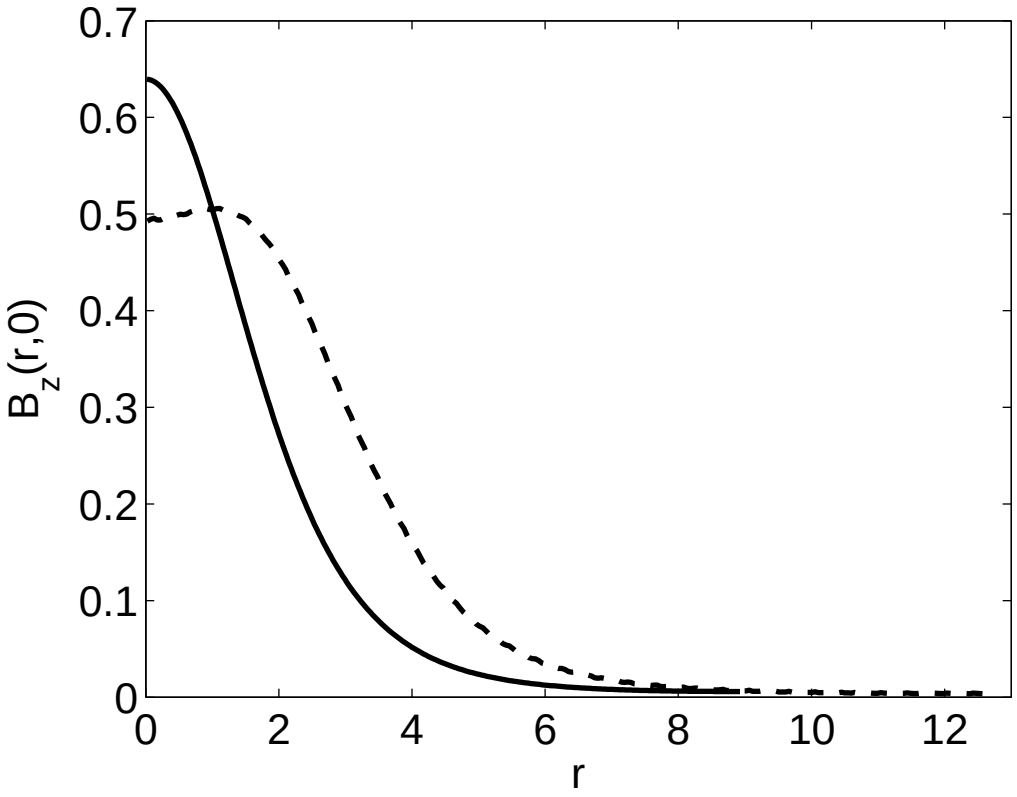

Figure 28: Film Circular Cell

Results for circular cell in film with parameters: $\kappa = 0.5$, $b = 0.1$, $d = 3$. We plot $B_z(r)$ at the midplane, $z = 0$, for a singly quantized vortex (solid line) with a circular cell radius $R = 8.9$, and a doubly quantized vortex (dashed line). At $r = 0$ the double shows the local minimum, or "dip", that is characteristic of our unphysical results for doubly quantized vortices in films using the circular cell method.

References

[1] J. Matricon and G. Waysand, *The cold wars: a history of superconductivity.* Rutgers University Press, 2003.

[2] A. J. Leggett, *Quantum liquids: Bose condensation and Cooper pairing in condensed-matter systems.* Oxford University Press, 2006.

[3] C. J. Gorter and H. Casimir, "On supraconductivity I," *Physica*, vol. 1, no. 1-6, pp. 306–320, 1934.

[4] F. London and H. London, "The Electromagnetic Equations of the Supraconductor," *Proc. R. Soc. A*, vol. 149, pp. 71–88, 1935.

[5] J. Bardeen, L. N. Cooper, and J. R. Schrieffer, "Theory of Superconductivity," *Phys. Rev.*, vol. 108, pp. 1175–1204, 1957.

[6] V. L. Ginzburg and L. D. Landau, "On the theory of superconductors," *Sov. Phys. JETP*, vol. 20, p. 1064, 1950.

[7] Gor'kov, "Microscopic derivation of the Ginzburg-Landau equations in the theory of Superconductivity," *Zh. Eksp. Teor. Fiz.*, vol. 36, p. 1918, 1959.

[8] M. Tinkham, "Effect of Fluxoid Quantization on Transitions of Superconducting Films," *Phys. Rev.*, vol. 129, no. 6, p. 2413, 1963.

[9] P. de Gennes, *Superconductivity of metals and alloys.* New York: W.A. Benjamin, 1966.

[10] M. Tinkham, *Introduction to superconductivity.* New York: McGraw Hill, 2nd ed. ed., 1996.

[11] A. B. Pippard, "An Experimental and Theoretical Study of the Relation between Magnetic Field and Current in a Superconductor," *Proc. R. Soc. A*, vol. 216, no. 1127, pp. 547–568, 1953.

[12] L. D. Landau, L. P. Pitaevskii, and E. Lifshitz, *Electrodynamics of Continuous Media, Second Edition: Volume 8.* Butterworth-Heinemann, 2 ed., 1984.

[13] F. London, "On the Problem of the Molecular Theory of Superconductivity," *Physical Review*, vol. 74, no. 5, p. 562, 1948.

[14] B. S. Deaver and W. M. Fairbank, "Experimental Evidence for Quantized Flux in Superconducting Cylinders," *Phys. Rev. Lett.*, vol. 7, no. 2, p. 43, 1961.

[15] R. Doll and M. Näbauer, "Experimental Proof of Magnetic Flux Quantization in a Superconducting Ring," *Phys. Rev. Lett.*, vol. 7, no. 2, p. 51, 1961.

[16] L. D. Landau and E. Lifshitz, *Statistical Physics, Third Edition, Part 1: Volume 5.* Butterworth-Heinemann, 3 ed., 1980.

[17] A. A. Abrikosov, "Magnetic Properties of Superconductors of the Second Group," *Zh. Eksp. Teor. Fiz.*, vol. 32, p. 1442, 1957.

[18] W. H. Kleiner, L. M. Roth, and S. H. Autler, "Bulk Solution of Ginzburg-Landau Equations for Type II Superconductors: Upper Critical Field Region," *Phys. Rev.*, vol. 133, no. 5A, p. A1226, 1964.

[19] J. Matricon, *Étude de quelques cas de pénétration du champ magnétique dans un supraconducteur.* PhD thesis, Universite' de Paris, 1966.

[20] E. H. Brandt, "Precision Ginzburg-Landau Solution of Ideal Vortex Lattices for Any Induction and Symmetry," *Phys. Rev. Lett.*, vol. 78, no. 11, p. 2208, 1997.

[21] E. H. Brandt, "Properties of the Ideal Ginzburg-Landau Vortex Lattice," *Physical Review B*, vol. 68, no. 5, p. 054506, 2003.

[22] W. W. Hager and H. Zhang, "Algorithm 851: CG_DESCENT, a conjugate gradient method with guaranteed descent," *ACM Trans. Math. Software*, vol. 32, no. 1, pp. 113–137, 2006.

[23] J. Nocedal and S. J. Wright, *Numerical optimization*. Springer, 1999.

[24] U. Klein and B. Pöttinger, "Virial theorem and Abrikosov's solution of the Ginzburg-Landau equations," *Phys. Rev. B*, vol. 44, no. 14, p. 7704, 1991.

[25] M. M. Doria, J. E. Gubernatis, and D. Rainer, "Virial theorem for Ginzburg-Landau theories with potential applications to numerical studies of type-II superconductors," *Phys. Rev. B*, vol. 39, no. 13, p. 9573, 1989.

[26] K. Maki, "Fluxoid Structure in Superconducting Films," *Ann. Phys. (N.Y.)*, vol. 34, no. 3, p. 363, 1965.

[27] G. Lasher, "Mixed State of Type-I Superconducting Films in a Perpendicular Magnetic Field," *Phys. Rev.*, vol. 154, p. 345, 1967.

[28] D. J. E. Callaway, "Magnetic flux patterns in the superconducting intermediate state," *Ann. Phys. (N.Y.)*, vol. 213, no. 1, p. 166, 1992.

[29] J. Pearl, "Current Distribution in Superconducting Films Carrying Quantized Fluxoids," *Appl. Phys. Lett.*, vol. 5, no. 4, p. 65, 1964.

[30] J. Pearl, *Vortex Theory of Superconductive Memories*. PhD thesis, Polytechnic Institute of Brooklyn, June 1965.

[31] G. J. Dolan and J. Silcox, "Critical Thicknesses in Superconducting Thin Films," *Phys. Rev. Lett.*, vol. 30, no. 13, p. 603, 1973.

[32] G. J. Dolan, "Critical thicknesses for the transition from intermediate- to mixed-state behavior in superconducting thin films of Pb, Sn, and In," *J. Low Temp. Phys.*, vol. 15, no. 1, pp. 133–160, 1974.

[33] G. J. Dolan, "Direct observations of the magnetic structure in thin films of Pb, Sn, and In," *J. Low Temp. Phys.*, vol. 15, no. 1, pp. 111–132, 1974.

[34] S. Hasegawa, T. Matsuda, J. Endo, N. Osakabe, M. Igarashi, T. Kobayashi, M. Naito, A. Tonomura, and R. Aoki, "Magnetic-flux quanta in superconducting thin films observed by electron holography and digital phase analysis," *Phys. Rev. B*, vol. 43, no. 10, p. 7631, 1991.

[35] G. S. Mkrtchyan and V. V. Shmidt, "Interaction between a cavity and a vortex in a superconductor of the second kind," *Sov. Phys. JETP*, vol. 34, no. 1, p. 195, 1972.

[36] G. R. Berdiyorov, M. V. M. sević, and F. M. Peeters, "Novel Commensurability Effects in Superconducting Films with Antidot Arrays," *Phys. Rev. Lett.*, vol. 96, no. 20, p. 207001, 2006.

[37] V. A. Schweigert, F. M. Peeters, and P. S. Deo, "Vortex Phase Diagram for Mesoscopic Superconducting Disks," *Phys. Rev. Lett.*, vol. 81, no. 13, p. 2783, 1998.

[38] G. R. Berdiyorov, A. D. Hernandez, and F. M. Peeters, "Confinement Effects on Intermediate-State Flux Patterns in Mesoscopic Type-I Superconductors," *Phys. Rev. Lett.*, vol. 103, no. 26, p. 267002, 2009.

[39] V. V. Moshchalkov, X. G. Qiu, and V. Bruyndoncx, "Paramagnetic Meissner effect from the self-consistent solution of the Ginzburg-Landau equations," *Phys. Rev. B*, vol. 55, no. 17, p. 11793, 1997.

[40] E. B. Bogomolnyi *Sov. J. Nucl. Phys.*, vol. 24, p. 449, 1976.

[41] I. Lukyanchuk, "Theory of Superconductors with κ close to 1/2," *Phys. Rev. B*, vol. 63, no. 17, p. 174504, 2001.

[42] E. H. Brandt, "Ginsburg-Landau Theory of the Vortex Lattice in Type-II Superconductors for all Values of κ and B," *Phys. Status Solidi B*, vol. 51, no. 1, pp. 345–358, 1972.

[43] E. H. Brandt, "Ginzburg-Landau Vortex Lattice in Superconductor Films of Finite Thickness," *Phys. Rev. B*, vol. 71, no. 1, p. 014521, 2005.

[44] E. H. Brandt, "Treatment of Stacking in Vortex Lattices of Type-II Superconductors Near H_{c2}," *Phys. Status Solidi*, vol. 36, no. 1, p. 381, 1969.

[45] A. B. Pippard, "A Possible Mechanism for the Peak Effect in Type-II Superconductors," *Phil. Mag.*, vol. 19, no. 158, p. 217, 1969.

[46] J. Hove, S. Mo, and A. Sudbo, "Vortex interactions and thermally induced crossover from type-I to type-II superconductivity," *Phys. Rev. B*, vol. 66, no. 6, p. 064524, 2002.

[47] L. D. Landau, E. M. Lifshitz, A. M. Kosevich, and L. P. Pitaevskii, *Theory of Elasticity.* Elsevier, 1986.

[48] M. H. Sadd, *Elasticity: Theory, Applications, and Numerics.* Academic Press, 2009.

[49] E. H. Brandt, "Die Behandlung von Fehlern im Flußliniengitter der Supraleiter 2," *Phys. Status Solidi B*, vol. 36, no. 1, p. 381, 1969.

[50] G. Lasher, "Series Solution of the Ginzburg-Landau Equations for the Abrikosov Mixed State," *Phys. Rev.*, vol. 140, p. A523, 1965.

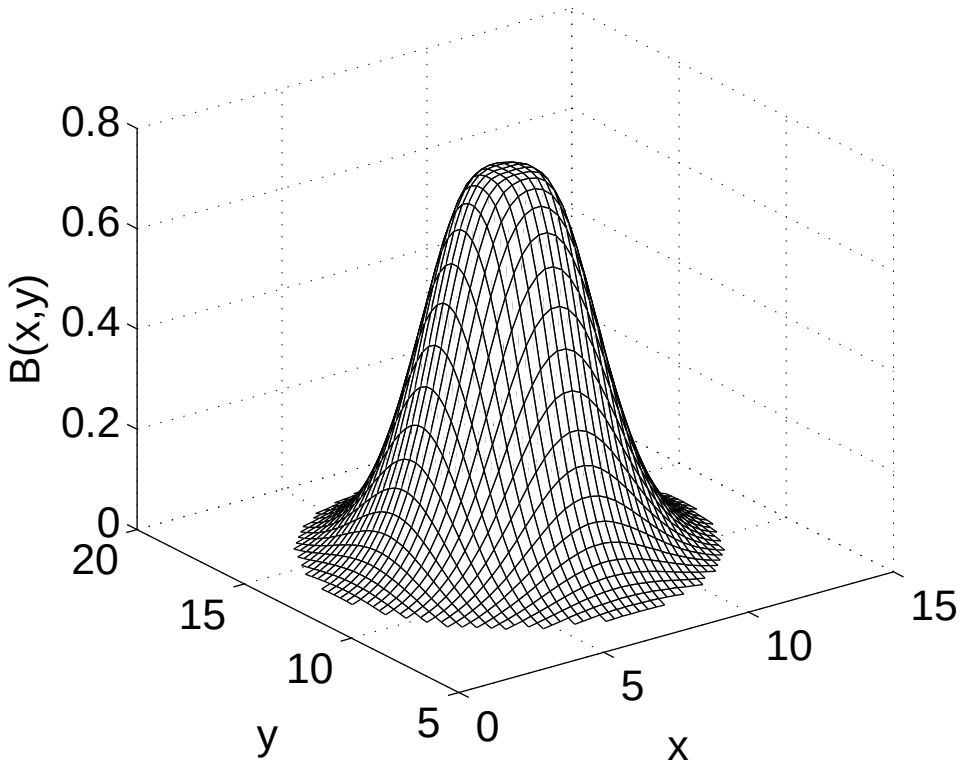

Figure 29: Doubles B_z for $\kappa = 0.5$

B_z for a bulk sample with $p = 2$, $\kappa = 0.5$ and $\bar{B}/\mu_0 H_{c2} = 0.3$.

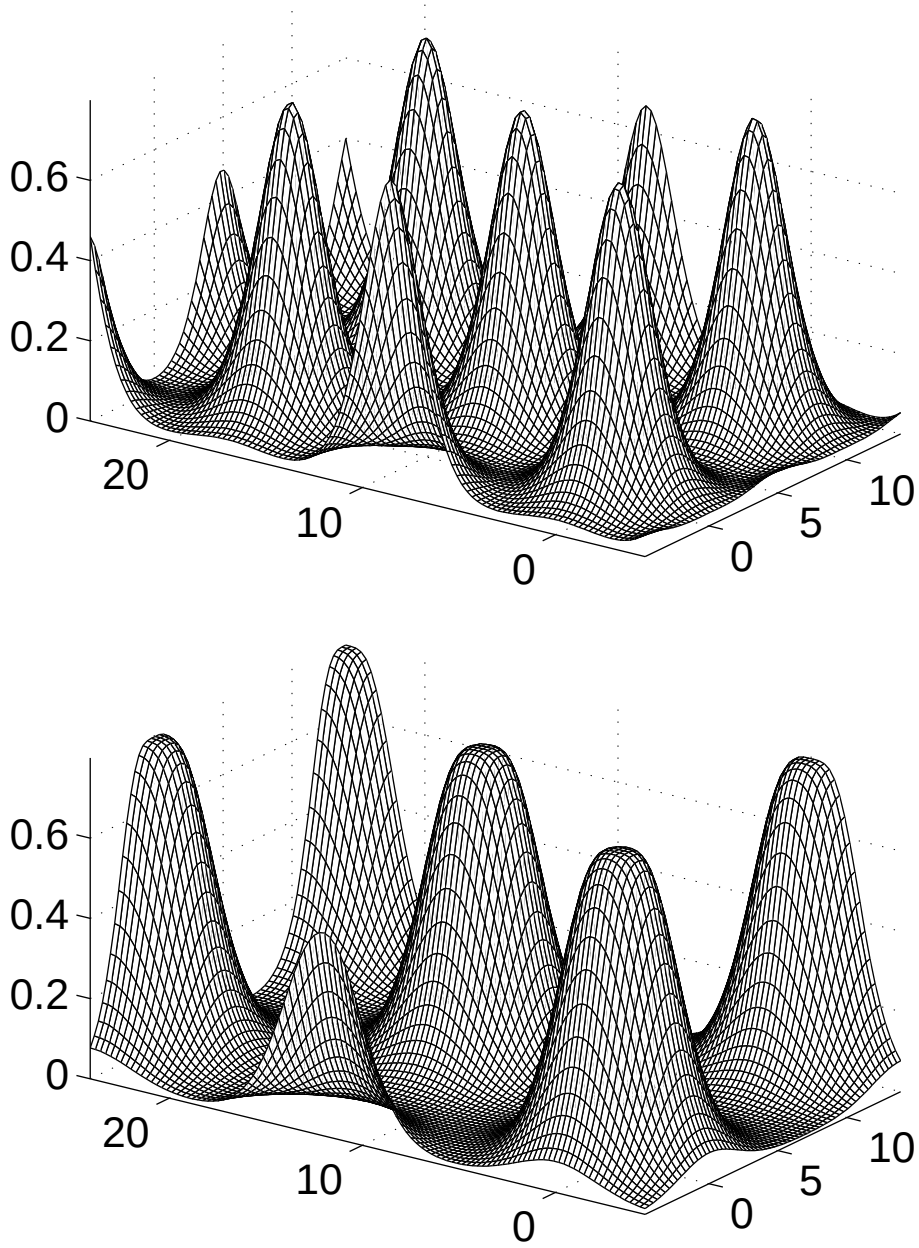

Figure 30: $B_z$for $\kappa = 0.5$

$B_z(x, y)$ for a bulk sample with $\kappa = 0.5$, $\bar{B}/\mu_0 H_{c2} = 0.3$ and a triangular lattice. Singles are shown in the upper plot with $B_z(0) = 0.80$, doubles in the lower plot with $B_z(0) = 0.78$. The vortex spacing for singles is $x_1 = 9.8$.

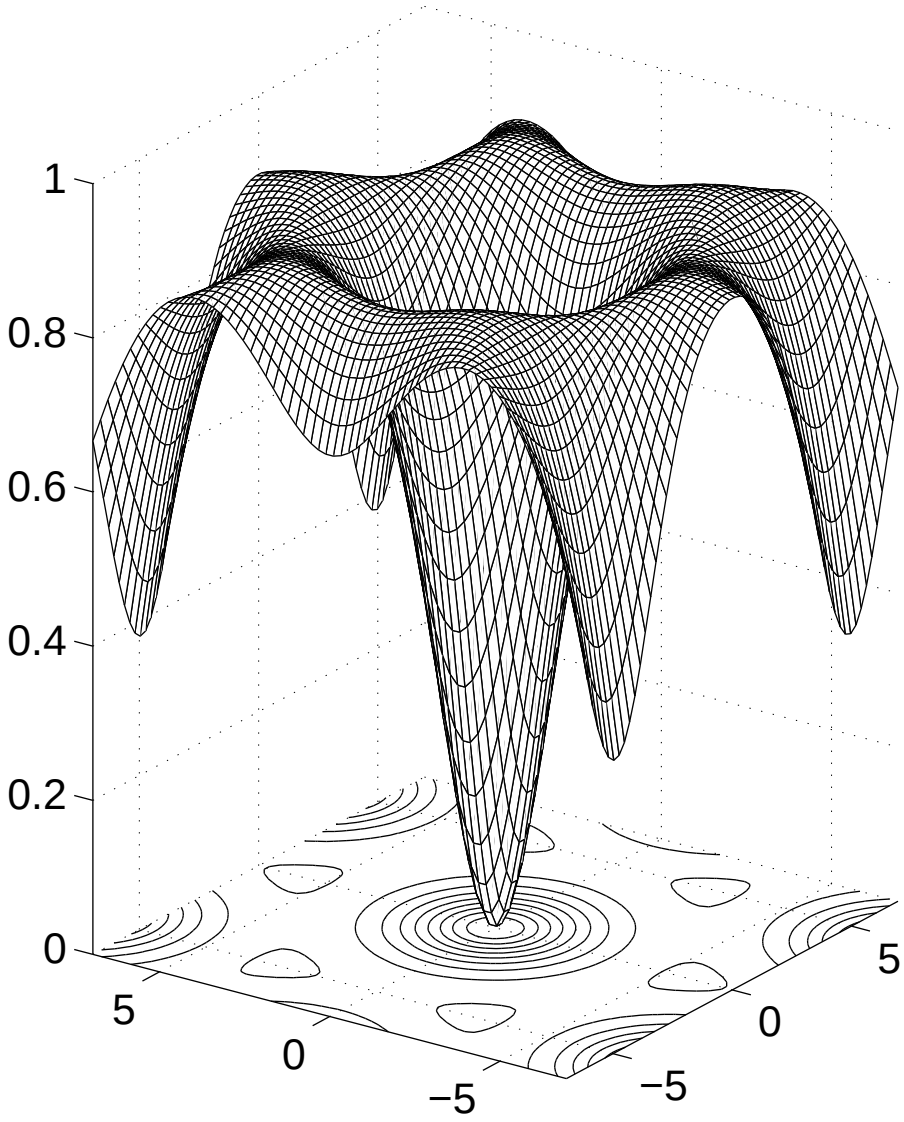

Figure 31: ω for $\kappa = 0.5$, Singles

$\omega\,(x, y)$ for a bulk sample with $\kappa = 0.5$, $\bar{B}/\mu_0 H_{c2} = 0.3$ and a triangular lattice of singly quantized vortices. The underlying contours are drawn at 0.1 intervals starting from 0.

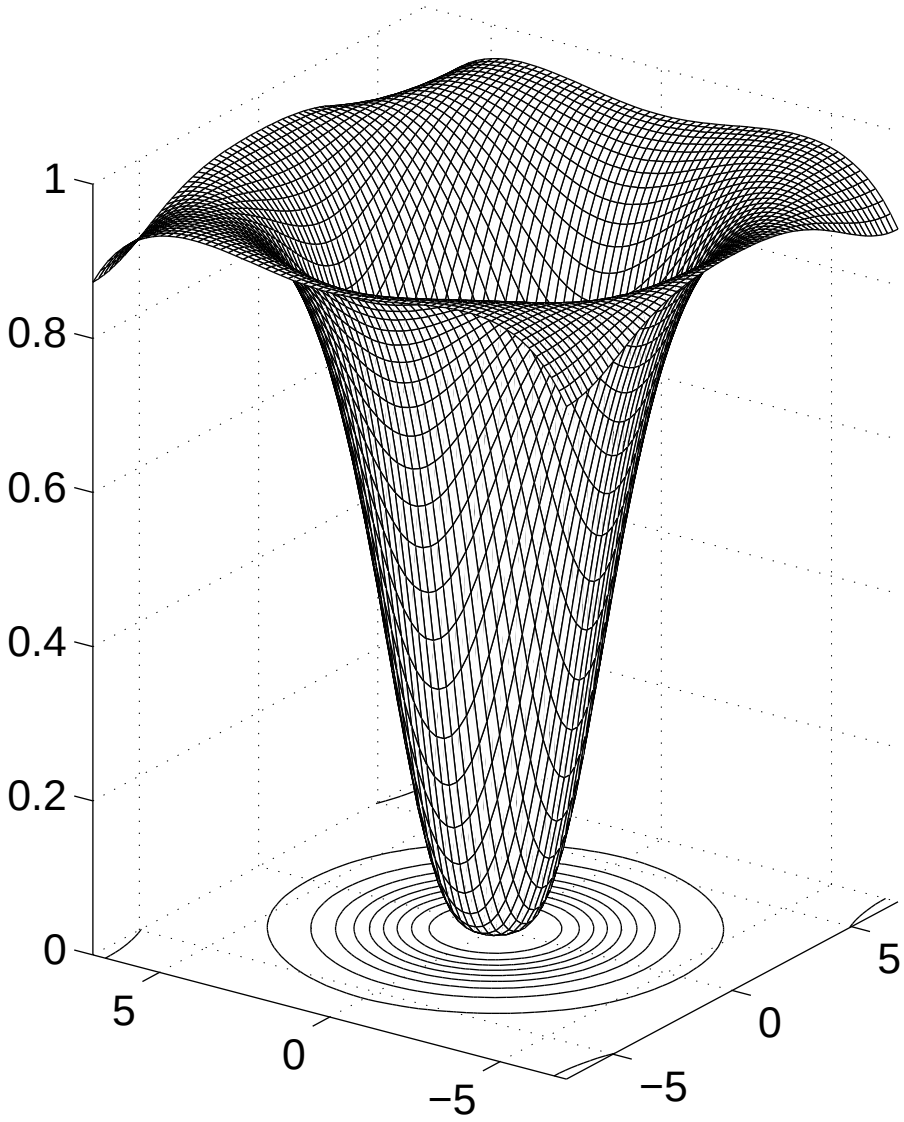

Figure 32: ω for $\kappa = 0.5$, Doubles

Same as for Fig. 31 but for a lattice of doubly quantized vortices.